University of South Australia

Institute for Telecommunications Research

**Ph.D Thesis**

# MIMO for Satellite Communication Systems

A thesis submitted in fulfillment of the requirements

for the degree of Doctor of Philosophy

**Balachander Ramamurthy**

August 22, 2018

# Contents

# List of Acronyms

**A2U** .......... Anchor to User

**AR** ........... Axial Ratio

**BER** .......... Bit Error Rate

**BGAN** ....... Broadband Global Area Network

**CP** ............ Co-Polar

**CSI** ........... Channel State Information

**CSIR** ......... CSI at the Receiver

**CSIT** ......... CSI at the Transmitter

**DP** ........... Dual Polarized

**DST** .......... Defence Science and Technology

**DVB** ......... Digital Video Broadcasting

**DVB-SH** ..... DVB Satellite services to Hand-held

**EIRP** ......... Equivalent Isotropic Radiated Power

**EM** ........... Electromagnetic

**EQ** ............ Equaliser

**EUTELSAT** . European Telecommunication Satellite Organisation

**FS** ............ Fixed Satellite

**GCD** ......... Greatest Common Divisor

**HTS** .......... High Throughput Satellite

**HiCapS** ...... High Capacity Satellite

**HSDPA** ...... High Speed Downlink Packet Access

**IEEE** ......... Institute of Electrical and Electronics Engineers

**ITR** ........... Institute for Telecommunications Research

**ITU** .......... International Telecommunications Union

**LDPC** ........ Low Density Parity Check

**LHCP** ........ Left Hand Circular Polarization

**LMS** .......... Land Mobile Satellite

**LNB** .......... Low Noise Block converter

**LOS** .......... Line of Sight

**LTE** .......... Long Term Evolution

**MILSATCOM** Military SATCOM

**MIMO** ....... Multiple Input Multiple Output

**MIMOSA** .... Characterisation of the MIMO channel for Mobile Satellite systems

**MMSE** ....... Minimum Mean Square Error

**MS** ........... Mobile Satellite

**MSMU** ....... Multi-Satellite Multi-User

**MUOS** ....... Mobile User Objective System

**MU-MIMO** .. Multi-User MIMO

**MUD** ......... Multi User Detection

**NGH** ......... Next Generation Hand-held

**NLOS** ........ Non Line of Sight

**OSTBC** ...... Orthogonal Space Time Block Code

**RHCP** ........ Right Hand Circular Polarization

**RRC** .......... Root Raised Cosine

**RTO** .......... Real Time Oscilloscope

**Rx** ............ Receiver

**SATCOM** .... Satellite Communication

**SC-FDE** ...... Single Carrier Frequency Domain Equalisation

**SISO** ......... Single Input Single Output

**SHF** .......... Super High Frequency

**SNR** .......... Signal to Noise Ratio

**SNIR** ......... Signal to Noise plus Interference Ratio

**SVD** .......... Singular Value Decomposition

**STR** .......... Symbol Timing Recovery

**STTC** ........ Space Time Trellis Code

**Tx** ............ Transmitter

**U2A** .......... User to Anchor

**U2U** .......... User to User

**UHF** .......... Ultra High Frequency

**ULA** .......... Uniform Linear Array

**UMTS** ........ Universal Mobile Telecommunications Service

**UT** ........... User Terminal

**UTC** .......... Coordinated Universal Time

**WiMax** ....... Worldwide Interoperability for Microwave Access

**WF** ........... Water Filling

**XP** ........... Cross-Polar

**XPD** ......... Cross-Polar Discrimination

**XPI** ........... Cross-Polar Isolation

**ZF** ............ Zero Forcing

# Notation

## Operations

$\dagger$ .............. Hermitian transpose

$*$ .............. Complex conjugate

$|\ .\ |$ ............ Absolute value

det(.) .......... Determinant

$(x)^+$ ........... Max $\{0, x\}$

$<\ .\ >$ ........ Time average

$||\ .\ ||$ .......... Vector or matrix norm

$\mathbb{E}(x)$ ........... Expectation value of x

## Some specific sets

$\mathbb{C}$ .............. Complex valued

$\Re$ .............. Real valued

$\mathcal{N}$ ............. Normal distribution

$\mathcal{U}$ .............. Uniform distribution

$\in$ .............. Element of

## Vectors and matrices

$\mathbf{y}$ .............. Receive signal (vector)

$\mathbf{x}$ .............. Transmit signal (vector)

$\mathbf{w}$ ............. Receiver noise (vector)

$\mathbf{H}$ ............. Channel matrix

$\widetilde{\mathbf{H}}$ ............. Channel phase only matrix

$\Upsilon$ ............. Matrix product of $\widetilde{\mathbf{H}}\widetilde{\mathbf{H}}^{\dagger}$

$\mathbf{I}$ .............. Identity matrix

$\mathbf{U}$,$\mathbf{V}$ ........... Unitary matrices

$\mathbf{J}$ .............. Channel matrix (between the satellites and large antennas)

$\mathbf{\Lambda}$ ............. Singular valued diagonal matrix

$\Sigma_w$ ............ Noise covariance matrix

$\Phi_{yv}$ ............ $2 \times 2$ matrix with differential phase coefficients

$\mathbf{p}_{\mathbf{L}}$ ............. Unit norm column vector representing LHCP

$\mathbf{p}_{\mathbf{R}}$ ............ Unit norm column vector representing RHCP

$\mathbf{P}$ ............. Polarization matrix

$\widehat{\mathbf{P}}$ ............. Scaled polarization matrix

$\mathbf{E}$ .............. Electric field vector

$\mathbf{h}$ .............. Horizontal component of $\mathbf{E}$ field vector

$\mathbf{v}$ .............. Vertical component of $\mathbf{E}$ field vector

$\mathcal{Z}$ ............. Position along the $\mathbf{z}$ axis

$\mathit{\Delta}$ ............. Combined Tx/Rx polarization matrix

## Scalars

$C$ ............. Channel capacity (bits/s/Hz)

$C_{\mathbf{opt}}$ ........... Optimal channel capacity (bits/s/Hz)

$R_{yv}$ ............ Cross-correlation coefficient of signals $y$ and $v$ at zero time lag

$T$ .............. Total integration time

$\mathbf{C}_{yv}$ ............ Coherency function for signals $y$ and $v$

$v_1, v_2$ .......... Received samples from antennas $\mathrm{v}_1$ and $\mathrm{v}_2$

$y_1, y_2$ .......... Received samples from antennas $\mathrm{y}_1$ and $\mathrm{y}_2$

$s_1, s_2$ .......... Transmitted samples from satellites $\mathrm{s}_1$ and $\mathrm{s}_2$

$\sigma_{s_1}^2, \sigma_{s_2}^2$ ........ Signal power in $s_1$ and $s_2$

$\sigma_\phi$ ............ Standard deviation of the differential phase estimate

$\sigma_\psi$ ............ Standard deviation of channel phase relationship estimate

$\mathbf{N_s}$ ........... Number of IQ samples

$i, l$ ............ index values

$\alpha$ ............. Antenna discrimination

$u$ ............. subscript denotes uplink

$d$ ............. subscript denotes downlink

$s$ ............. subscript denotes the satellite link

$t$ ............. subscript denotes the total link

$\lambda$ ............. Channel singular values

$\mu$ ............. Transmit power constraint factor

$S$ ............. Total transmit signal power

$M$ ............ Number of antennas in space

$N, Z$ .......... Number of antennas on the ground at source and destination respectively

$m$ ............ Antenna index $m \in \{1, 2...M\}$

$n$ ............. Antenna index $n \in \{1, 2...N\}$

$E_s$ ............ Energy per symbol

$N_o$ ............ Noise power spectral density (dBW/Hz)

$\sigma_w^2$ ............ Noise power

$r$ ............. Range distance (m)

$h$ ............. Channel path coefficient

$a$ ............. Channel path attenuation

$L$ ............. Channel path power loss

$g$ ............. Combined transmit and receive antenna gain

$g^{\mathbf{rx}}$ ........... Receive antenna gain

$g^{\mathbf{tx}}$ ........... transmit antenna gain

$G$ ............ Antenna power gain factor

$f$ .............. Frequency (Hz)

$c$ .............. Speed of light (m/s)

$k$ .............. Rank of the channel matrix

$K$ ............. Ricean factor

$\tau$ .............. Propagation time (s)

$T_d$ ............. Propagation time difference (s)

$\nu$ .............. Integer-valued periodicity factor

$\kappa_q$ ............. Integer-valued periodicity factor (second degree)

$\phi$ .............. Deterministic phase in the channel path coefficient

$\widehat{\phi}$ .............. Unbiased estimate of differential phase

$\widetilde{\phi}$ .............. Measured value of the differential phase

$\phi_e$ ............. Estimation error value in channel phase relationship

$\psi$ .............. Phase relationship (orthogonality factor) in the channel matrix

$\widehat{\psi}$ .............. Unbiased estimate of phase relationship in the channel matrix

$\widetilde{\psi}$ .............. Measured phase relationship in the channel matrix

$\psi_e$ ............. Error in the estimation of channel phase relationship

$\rho$ .............. Signal to noise ratio

$\varrho$ .............. Signal to noise plus interference ratio

$\eta$ .............. Power gain in the channel matrix

$\Omega$ .............. Displacement angle in latitude and longitude on the ground (degrees)

$\zeta_{il}$ ............. Elements of the matrix $\Upsilon$, $\{i, l = 1, 2, ..M\}$

$\mathbf{d_G}$ ............ Distance between the antennas on the ground

$\mathbf{d_S}$ ............. Distance between the antennas in space

$\delta_{\mathbf{G}}$ ............. Orientation angle with respect to the local North-South direction on the ground (degrees)

$E_h, E_v$ ......... Instantaneous electric field amplitude of the **h** and **v** components

$E_1, E_2$ ......... Peak electric field amplitude of the **h** and **v** components

$\beta$ .............. Wave number

$\mathcal{Z}$ ............. Polarization direction of propagation

$\delta_{\mathbf{P}}$ ............. Relative phase between **h** and **v** components

$\xi$ .............. Polarization tilt angle

$A$ .............. Amplitude error in antenna polarization excitation

$\varphi$ .............. Phase error in antenna polarization excitation

$p$ .............. Polarization parallelity

$\vartheta_{ij}$ ............. Elements of the matrix $\varDelta$

# List of Figures

# List of Tables

# Summary

The multiple antenna technique, MIMO (Multiple Input Multiple Output) is a success story in wireless communication systems. One of the main features of MIMO is the utilisation of the spatial dimension. The spatial dimension in MIMO brings significant performance improvement through array gain, spatial diversity, spatial multiplexing and interference avoidance. In this thesis, the application of MIMO to satellite communications (SATCOMs) is analysed and addressed, especially to Military SATCOM (MILSATCOM) systems operating at UHF, X and Ka band frequencies in geo-stationary orbit.

It is common for a SATCOM channel between the ground and a satellite to have a strong line of sight (LOS) path. The LOS path is essential in achieving a healthy link budget. However, in a MIMO scenario the LOS nature of the channel and the large range distance in the channel path can increase the spatial correlation between the channel paths. Geometrical optimisation is required to achieve extra spatial degrees of freedom. To achieve spatial orthogonality in the LOS SATCOM channel, antenna separation on the order of several kilometres (depending on the wavelength) is required either in space or on the ground.

In this thesis, the investigation begins with analysing the applicability of MIMO to UHF SATCOM. The benefits of spatial multiplexing using multiple satellites are addressed in the analysis. UHF SATCOM has some unique advantages compared to other higher frequency bands, but at the same time, some inherent disadvantages including limited usable bandwidth and significant restrictions on applying frequency reuse in the geostationary arc, resulting in low capacity. Generally, from a commercial perspective, a MIMO scenario using multiple satellites is not considered as a cost effective solution. However, we show that narrowband MILSATCOM in UHF is a good example where using MIMO with multiple satellites can be most useful to increase the overall spectral efficiency through frequency reuse.

Utilising orthogonal circular polarizations is another well known frequency reuse technique in MILSATCOM. However, due to channel depolarization and polarization excitation errors in the antenna, the resulting polarization wave will often be elliptical

in practice. Thus, any mismatch in antenna orientation can result in poor cross polar isolation (XPI) and this can severely degrade the system performance in respect of polarization frequency reuse. In this thesis, this problem is addressed within a MIMO framework. Polarization multiplexing is jointly analysed with spatial multiplexing using two X-band satellites in adjacent orbital slots and is shown to achieve a four-fold increase in channel capacity. The analysis also shows that the MIMO processing mitigates the effect of polarization imperfections.

Spatial multiplexing in single satellite systems using Multi-User MIMO (MU-MIMO) is also investigated. Next generation Ka-band SATCOM systems are ambitious in-terms of throughput and capacity using multiple spot beams. There are two categories of SATCOM systems that have emerged: The first is High Throughput Satellite (HTS) systems aiming to increase the overall throughput of a satellite; the second is High Capacity Satellite (HiCapS) systems, where the aim is to increase the satellite's capacity in a given region. The application of MIMO techniques to improve the system performance is a topic for research in both these scenarios. In this thesis, consideration is given to increase the frequency reuse for HiCapS systems in a high demand geographic region. Practical trade-off, user location sensitivity and MIMO communications signal processing architectures are analysed in this thesis. The results show that a linear increase in channel capacity can be achieved through MU-MIMO for a satellite with multiple spot beam antennas with overlapping frequencies serving the same geographical region.

Finally, channel measurement results are provided using a novel passive MIMO SATCOM channel measurement technique. The channel measurement results are paramount to validate the theory and knowing the channel parameters is necessary to achieve MIMO gain in real world scenarios. Results from two different measurement campaigns are presented: the first was in collaboration with Prof. Knopp and his team at the Munich University of the Bundeswehr, using signals received from two EUTELSAT satellites in Ku-band. The second was a measurement campaign conducted at the Defence Science Technology (DST) Group, Edinburgh, South Australia, in the MILSATCOM X-band.

# Acknowledgment

The satisfaction and euphoria that accompany the success of any work would be incomplete without the mention of the people who made it possible. I have great pleasure in acknowledging everyone who has contributed during the tenure of my thesis.

Firstly, I would like to express my sincere gratitude to my principal supervisor, Adjunct Prof. Bill Cowley for the continuous support of my Ph.D study and related research. I've known Bill since 2005 when he supervised me for my Master's research degree and now for my Ph.D research. Thanks Bill, for your continuous motivation and guidance, plus your commitment even post retirement in an adjunct role is extraordinary. Thanks to my associate supervisor from Defence Science and Technology (DST) Group, Dr. Gerald Bolding. This thesis would have not been possible without his exceptional support throughout the program. Thanks to my second associate supervisor, Dr. Linda Davis, who actively mentored me during the first half of my study.

I would like to thank my employer, DST Group, for this wonderful opportunity to complete this study under a work based part-time Ph.D study framework. Especially, to the two former Research Leaders in the Assured Communications Branch, Dr. Peter Shoubridge and Dr. Phil Stimson. Thanks to all the staff and students at the Institute for Telecommunications Research, UniSA, for providing me a stimulating academic environment.

My sincere appreciation and thanks also goes to Prof. Andreas Knopp and Mr. Robert Schwarz from the University of the Bundeswehr, Munich, Germany, who provided me an opportunity to join their team as a visiting researcher and provided access to the laboratory and research facilities.

I would like to thank all my fellow DST Group colleagues in the Protected Satellite Communications Group, and especially to Dr. Ismail Shakeel, Dr. Ian Holland and Dr. Weimin Zhang for the support plus sharing their expertise and experiences.

Last but not least, I would like to thank my wife Anitha, for morally supporting me in this journey for the last five years. It is a phenomenal support, especially with our two young children Tharan and Keshav.

# Declaration

I declare that this thesis contains no material which has been accepted for the award of any degree or diploma in any university and to the best of my knowledge it does not contain any material previously published or written by another person, except where due reference is made in the text.

Balachander Ramamurthy

Digitally signed by Balachander Ramamurthy
DN: cn=Balachander Ramamurthy, o=Department of Defence, ou=Defence Science and Technology Group, email=Balachander.Ramamurthy@dsto.defence.gov.au, c=AU
Date: 2018.08.24 13:10:42 +09'30'

Balachander Ramamurthy

# Chapter 1

# Introduction

The multiple antenna technique popularly known as MIMO (Multiple Input and Multiple Output) constituted a breakthrough in wireless communications system design. MIMO is a success story for two reasons: the first is the increase in data rate achieved through spatial multiplexing and the second is the improvement in reliability by exploiting the diversity in the channel [1]. The MIMO gain can be expressed in terms of rate and reliability; usually there is a trade-off in that the gain can be directed at either rate or reliability or both. The increase in channel capacity through MIMO may be explained from an information theory perspective and is achieved without requiring extra transmit power or additional bandwidth [2].

Although the general concepts of MIMO are longstanding, the popularity of MIMO has increased tremendously since 1998 with the publication of Alamouti's spatial diversity scheme [3] to achieve reliability. In the same year, the publication of space-time trellis codes (STTCs) [4] showed that multiplexing gain can be achieved from spatial diversity. For more than two decades, MIMO techniques have been widely researched and have continued to be an area of interest in both academia and industry. Many standards have now incorporated MIMO; for example, the International Telecommunications Union (ITU) specifies MIMO in the High Speed Downlink Packet Access (HSDPA) as part of the Universal Mobile Telecommunications Services (UMTS) standard, MIMO is incorporated in IEEE standards for wireless routers (802.11n), mobile WiMAX (802.16) and the Long Term Evolution (LTE) standard. Massive MIMO, a scalable version of the Multi User MIMO (MU-MIMO) technology is considered a promising technological breakthrough for 5G mobile wireless standards [5].

The success realised from the application of MIMO techniques in wireless communications have generated interest in the use of MIMO in satellite communication (SATCOM) systems. However, a SATCOM channel can be unlike the terrestrial channel in that it often does not exhibit the rich scattering environment and multi-path propagation that has traditionally provided opportunities for MIMO gains. The SATCOM channel, especially at X-band (7 GHz) and above is dominated by the line of sight (LOS) path.

The absence of scatterers in the SATCOM propagation path leads to rank deficiency in the spatial MIMO channel matrix. Hence, at a first glance it may appear that MIMO is not a candidate to provide spatial diversity or multiplexing gains for SATCOM. However, in spite of a dominant LOS path between the transmit and receive antennas, SATCOM can be shown to benefit from MIMO using orthogonal polarizations, multiple satellites, multiple ground terminals and multiple user concepts.

## 1.1 Scope and Significance

This thesis studies the application of MIMO to SATCOM and considers a comparison between MIMO and conventional single input single output (SISO) SATCOM. Figure 1.1 is a generic picture that conceptualises the application of MIMO for SATCOM systems. The satellites considered in this study are in geostationary orbit and typically employ non-regenerative transponder architectures. A MIMO channel matrix can be constructed from multiple diversity sources such as orthogonal polarizations, multiple ground terminals, multiple users and multiple satellites. It is not the intent that a MIMO SATCOM approach would necessarily use the entire connection matrix as shown in Figure 1.1.

The primary aims of this thesis are:

- To analyse the available degrees of freedom in the LOS dominated SATCOM channel using multiple antennas.
- To understand the spatial constraint that is required for MIMO in SATCOM.
- To analyse different application scenarios, using system models and communication architectures. For example, spatial multiplexing using multiple antennas on multiple satellites or multiple antennas on a single satellite systems with displaced users on the ground.
- To analyse frequency reuse in SATCOM using orthogonal polarizations and the benefits of using MIMO to mitigate polarization imperfections.
- Where possible, to demonstrate the theoretical concepts by practical experiments and channel measurement campaigns.

## 1.2 Multiple Input Multiple Output

Historically, wireless communication systems using single antennas have evolved to efficiently make use of the time and frequency dimensions. One of the main attributes of using multiple antennas is the utilisation of the spatial dimension. The spatial dimension in using MIMO brings significant performance improvement through array gain, spatial diversity, spatial multiplexing and interference avoidance [6].

Array gain is a straightforward result of using multiple antennas either at the transmitter or receiver or both. Array gain helps to increase the signal to noise ratio (SNR) of the system by coherently combining the signals, and is often also called power gain or beamforming gain.

MIMO spatial diversity techniques are useful in improving the reliability of a wireless channel. Fading is generally considered as an unwanted component that can drastically affect the reliability of the wireless communications systems. Fading is a result of multipath scattering of the transmitted signal in the channel before it reaches the receiver. MIMO systems can be deliberately designed to exploit spatial diversity by

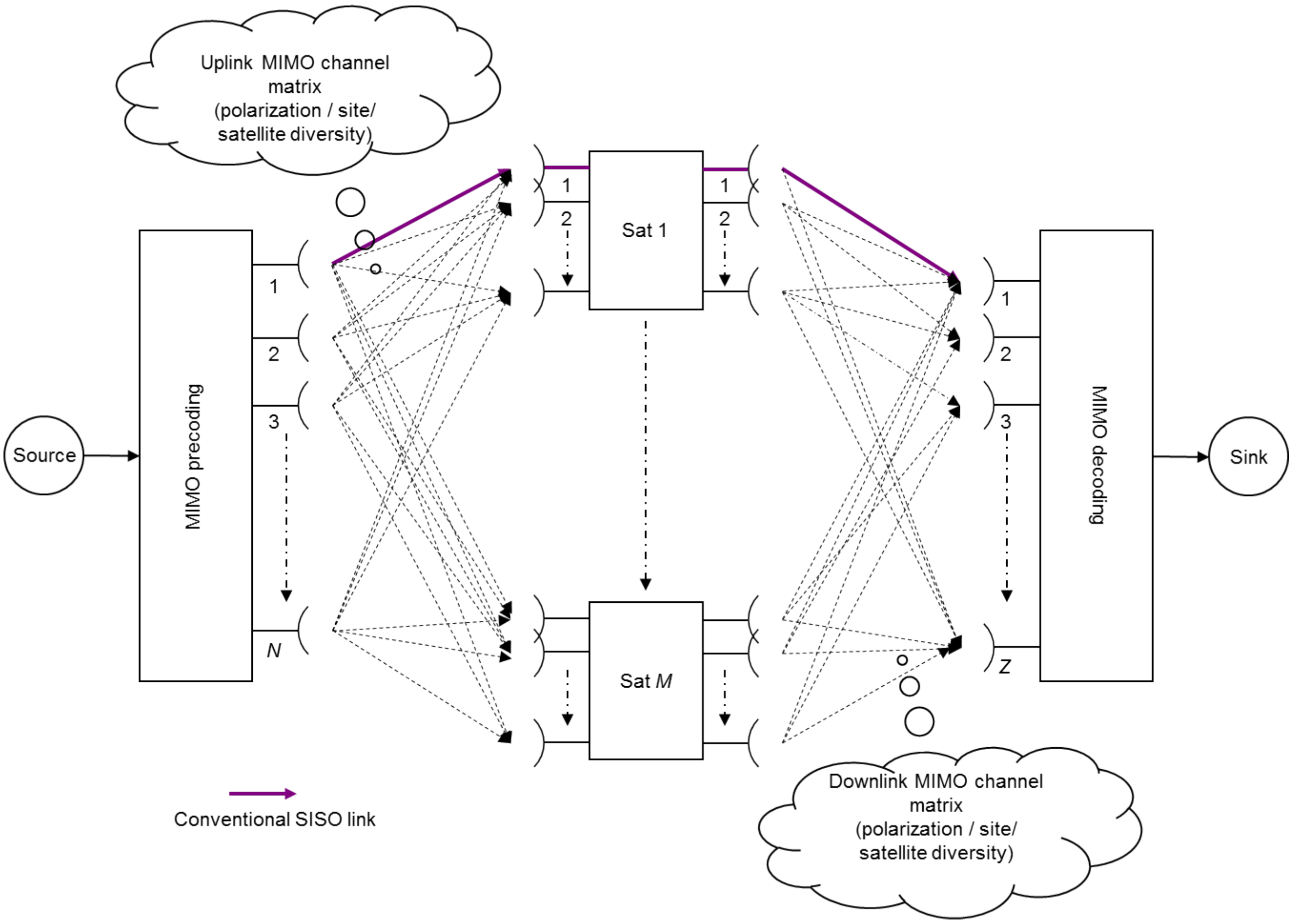


Figure 1.1: MIMO SATCOM Model

transmitting multiple copies of the signal in space and time. For a MIMO system with $N$ and $M$ antennas at the transmitter and receiver respectively, the maximum diversity order is given by the product $(NM)$, denoting the number of independent fading paths in the channel.

MIMO spatial multiplexing offers a linear increase in capacity and data rate. It makes use of the spatial dimension to yield extra degrees of freedom through which multiplexing gain can be achieved. Spatial multiplexing utilises the orthogonality in the channel paths to transmit parallel data streams from each antenna in space and time. Under suitable channel conditions, the number of degrees of freedom gained is usually the $\min\{N, M\}$.

Multi-User MIMO (MU-MIMO) can increase the overall channel capacity through spatial multiplexing and act as a interference avoidance technique between the users. It provides a method whereby multiple users can simultaneously use the same frequency and time resources. The interference between the users is avoided using the spatial dimension. The main advantages of MU-MIMO are that each user is not required to have multiple antennas and the techniques are well suited for channels dominated by the LOS path.

In practice, it may not be possible for a MIMO system to exploit all the advantages of the spatial dimension. Depending on the channel environment, usually a combination of these methods can yield enhancement in channel capacity and reliability.

## 1.3 Thesis Structure and Contributions

- **Chapter-2:** Provides a brief background on subjects that are presented in subsequent chapters of this thesis. These background materials include: An introduction to SATCOM and MILSATCOM, frequency bands of interest, MIMO channel capacity and a literature review of existing work in MIMO for SATCOM.

- **Chapter-3:** Large antenna separation either at the transmitter or at the receiver has been shown to provide an exploitable " degree of freedom " for spatial multiplexing in SATCOM [7]. Motivated by the research of Prof. Knopp and his team, the investigation in this chapter is extended to narrowband SATCOM in the Ultra High Frequency band (UHF) band. UHF user terminals are typically low cost, easily deployable and have broad antenna beamwidths so that precise pointing to the satellite is not a requirement for mobile users. At the same time, some inherent disadvantages of UHF SATCOM are limited bandwidth and significant restrictions in applying frequency reuse in the geo-stationary arc, hence less overall capacity. Strict frequency and orbital coordination is in place to avoid interference with other satellites. The use of MIMO spatial multiplexing techniques are found to be useful in these scenarios. Channel modelling, capacity analysis, communication signal processing architectures to deal with multi-satellite synchronisation issues and satellite ephemeris impacts are addressed in this chapter. Parts of the content from this chapter have been published [8, 9].

- **Chapter-4:** In this chapter, the benefits of polarization multiplexing are analysed and discussed. Utilizing orthogonal polarizations is a well-known frequency reuse technique in SATCOM to provide additional spectrum in a given geographical region. However, in practice there is a link degradation due to cross talk between the two polarization channels. The cross talk results from the combined effects of the antenna's imperfect ability to distinguish between the two polarizations and channel depolarization effects. The effect of cross talk can be significant, limiting the benefits of using orthogonal polarizations. Greater cross-polar isolation (XPI) reduces the link degradation in terms of the received signal to noise plus interference ratio (SNIR). In this chapter a polarization channel model is derived and the XPI impact is evaluated in terms of received SNIR when using orthogonal polarizations. The use of MIMO techniques to mitigate the XPI impact are analysed in this chapter. Using a case study in the MILSATCOM X-band with two satellites, the investigation is extended to analyse the MIMO SATCOM channel capacity by simultaneously utilising polarization and spatial multiplexing. Parts of the content of this chapter have been published [10, 11].

- **Chapter-5:** MU-MIMO is an attractive solution for SATCOM systems that are dominated by the LOS signal path. There is a wave of interest and research effort investigating MU-MIMO for High Throughput Satellite (HTS) systems in Ka-band to mitigate interference issues. In this chapter, the application of MU-MIMO is analysed and investigated for High Capacity Satellites (HiCapS) systems by expanding on the spatial multiplexing concepts from Chapter-3. The results show that channel capacity can be linearly increased using multiple antennas on a single satellite, albeit with some restrictions and an increase in complexity. A framework to enhance the overall communication capacity of a satellite in servicing a single geographical region is described. Practical trade-offs, user location sensitivity and MIMO communications signal processing architectures are also analysed in this chapter.

- **Chapter-6:** In the previous chapters, it is shown that MIMO for SATCOM is a key enabler to provide higher data rates for commercial applications or to increase capacity in MILSATCOM. It is imperative that the theoretical concepts can be proven by channel measurements and experiments. This chapter presents a unique passive channel measurement technique developed by the author, to validate the MIMO SATCOM channel. The measurement method uses cross-correlation analysis of the received signals to estimate differential phase measurements without the need to actively transmit signals to the satellites. These phase measurements are used to estimate the channel orthogonality and compared with theoretical models. Results from two different measurement campaigns are presented in this chapter: The first was in collaboration with Prof. Knopp and his team at the Munich University of the Bundeswehr, using signals received from two EUTELSAT satellites in Ku-band. The second was a measurement campaign in the MILSATCOM X-band, completed at Defence Science and Technology Group, Edinburgh, South Australia. The measurement method, accuracy analysis and results are presented in this chapter.

- **Chapter-7:** The conclusion and remarks for future work in MIMO SATCOM are presented in this chapter.

# Chapter 2

# Background

Satellite communications play a vital role in delivering global access to communications. In the last 60 years the satellite industry has seen a tremendous technological growth. Originally SATCOM was designed to relay information from one point to another, but with increasing satellite size and power, today's SATCOM technology is able to satisfy a broad range of applications. The successful role of SATCOM can be witnessed in television and radio broadcasting services, broadband Internet access, Maritime plus other on-the-move applications and as a backbone for military communications.

The orbits for communication satellites are generally categorised into geostationary and non-geostationary. Historically, the most popular is the geostationary orbit with near zero inclination, where the satellite orbits around the earth in the equatorial plane at an altitude of 35786 km above the equator. The period is equal to the Earth's rotation and thus it appears that the satellite is stationary at a point in space relative to any point on the Earth. Currently, a multitude of satellites occupy the geostationary belt in discrete locations known as orbital slots. A list of commercial satellites that ring the Earth as of June 2011 is shown in Figure 2.1 [1]. The proliferation of satellites has reached a point where less than two degrees can separate adjacent satellites in the same frequency band. In some cases, multiple satellites using different frequency bands occupy a single orbital slot. Hence, both the frequency spectrum and the availability of an orbital slot have become a premium resource in SATCOM. The

[1] Picture published by Boeing

International Telecommunication Union (ITU) coordinates the frequency planning and orbital allocation for satellites in space that are used by different agencies or countries.

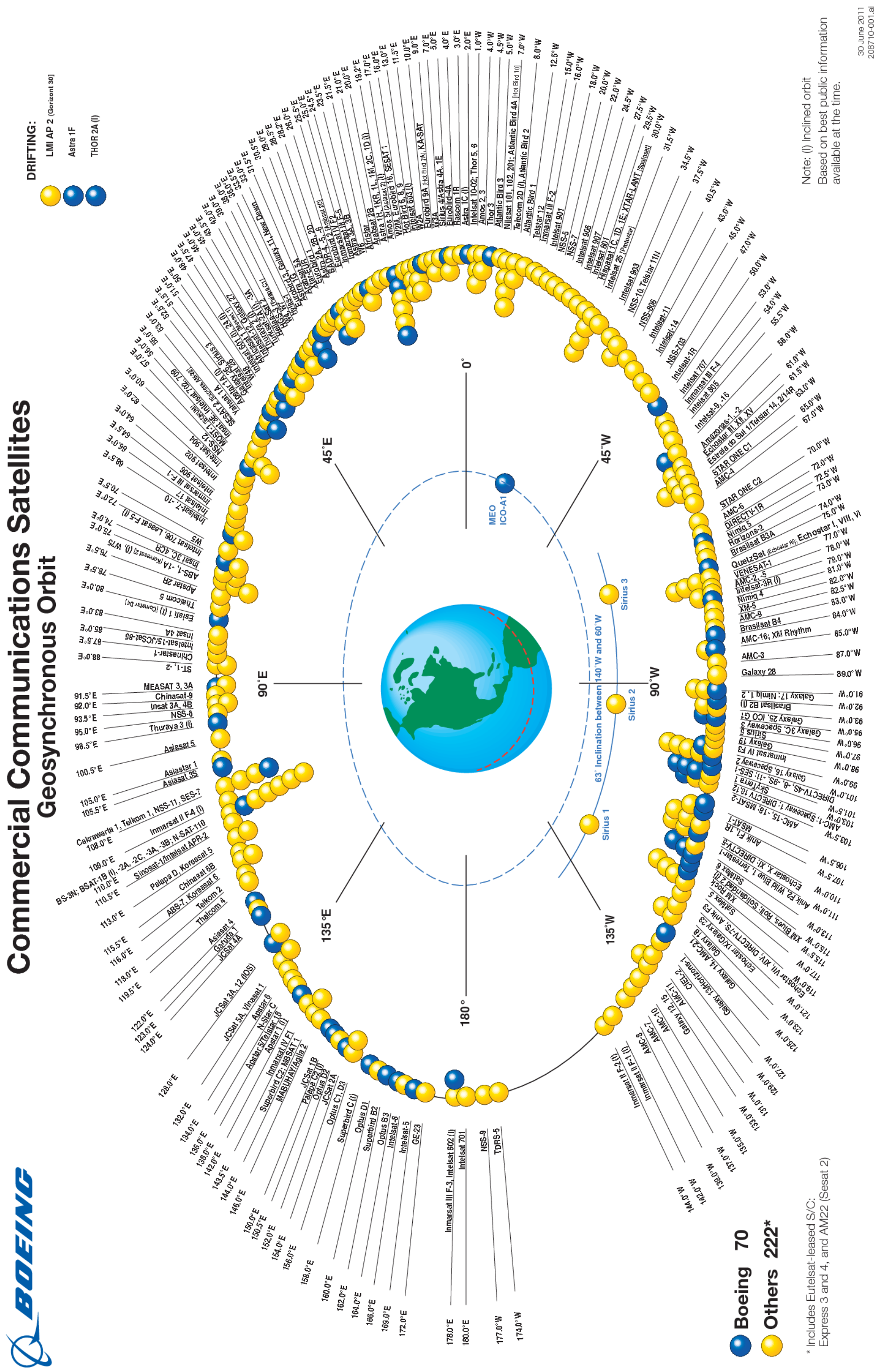


Figure 2.1: Satellites in geostationary orbit

There are two types of satellite communications payload architectures that are typically employed: The first and most common is non-regenerative, also called a transparent or bent-pipe payload. It is a transponding architecture, where the received signal is frequency converted, amplified and retransmitted back to the ground. In recent years, digital channelisation techniques have become popular in the transponder architecture, for example in the Wideband Global SATCOM (WGS) system [12]. This increases the on-board flexibility in gain control and frequency translation. One major disadvantage of the non-regenerative payload is the amplification of the noise signal from the receiver being transmitted back to the ground, using valuable power and contributing to reducing the overall relayed signal quality. The second type is a regenerative payload, where the received signal is demodulated, remodulated, frequency translated, amplified and routed to the desired destination beam. Of the two, the most commonly used payload is based on the non-regenerative type. The reasons for this are (historically) due to lower complexity (cost) plus high flexibility.

Looking into the future, there is a growing trend to launch more powerful satellites into geostationary orbits. Each of these satellites can deliver capacity in the order of 100 Gbps to 1 Tbps, typically operate in higher frequency bands and have a large number of spot beams with a high degree of frequency reuse. Some identified technologies to meet the demand for future SATCOM needs are: High Throughput Satellites (HTS), hybrid SATCOM and terrestrial communications [13], MIMO for capacity enhancement and interference avoidance and adaptive beamforming [14].

## 2.1 SATCOM Frequency Bands

Each SATCOM frequency band exhibits different propagation characteristics. Due to the finite geostationary orbital slots and high demand, frequency congestion is a serious problem, especially at lower frequency bands such as UHF. The higher the frequency band, typically, there is access to more bandwidth. Higher frequency bands are becoming popular due to this large available bandwidth and technology evolution. To obtain a certain antenna gain and beamwidth, the required antenna size decreases as the frequency increases. At the same time, the higher frequency bands have greater path loss and are more prone to degradation in rain and weather events. The SATCOM frequency bands are classified into:

**UHF**: SATCOM in the UHF band is primarily used for voice and data communication services. The band extends from 220 MHz to 400 MHz. The UHF band is popular among the MILSATCOM community for its convenient small antennas, mobility, canopy penetration and for being less susceptible to weather conditions. The conventional MILSATCOM frequency range spans from 244 to 270 MHz for the downlink and 292 to 317 MHz for the uplink. The application of MIMO spatial multiplexing to narrow bandwidth UHF channels is analysed and presented in Chapter-3. The Mobile User Objective System (MUOS) is the next generational UHF MILSATCOM system developed by the US DoD [15]. MUOS occupies 300 to 320 MHz for the uplink and 360 to 380 MHz for the downlink for the user side of the link. Insights into how MIMO could be useful for MUOS satellites are discussed in Chapter-7.

**L-band**: L-band ranges from 1 to 2 GHz and is primarily used by satellite mobile phone systems such as Iridium and INMARSAT's Broadband Global Area Network (BGAN).

**S-band**: S-band ranges from 2 to 4 GHz. The majority of the MIMO literature for SATCOM have devoted their analysis to L-band and S-band for Land Mobile Satellite (LMS) channels. In LOS path obstructed channel environments, multipath effects will be more pronounced and the channel will exhibit a Rayleigh channel characteristics. In these scenarios, multipath diversity can be exploited using MIMO spatial diversity or multiplexing techniques.

**C-band**: C-band ranges from 4 to 6.5 GHz. It is used for satellite TV broadcasting networks and is less subject to rain fading than the following higher frequency bands.

**X-band**: X-band ranges from 7 to 11.2 GHz. A dedicated 500 MHz bandwidth in X-band is allocated for MILSATCOM systems, with the downlink from 7.25 to 7.75 GHz and the uplink from 7.9 to 8.4 GHz. The satellites and terminals using X-band frequencies require high gain directional antennas to overcome the path loss and to support high data rates. The application of MIMO in X-band jointly utilising polarization and spatial multiplexing is analysed and discussed in Chapter-4. MIMO channel measurement results using two X-band satellites are presented in Chapter-6.

**Ku-band**: Ku-band ranges from 12 to 18 GHz. It is a heavily used used for commercial TV broadcasting and direct-to-home services. Often, Ku-band is preferred over C-band because of smaller user antenna size requirements. Owing to its heavy usage, frequency and bandwidth availability in Ku-band is scarce. MIMO spatial multiplexing techniques using single or multiple satellites could be useful to enhance the spectral efficiency in Ku-band. MIMO channel measurement results using two EUTELSAT satellites in Ku-band are presented in Chapter-6

**Ka-band**: Ka-band ranges from 26 to 40 GHz. The MILSATCOM systems have one GHz bandwidth allocation in Ka-band, the downlink from 20.2 to 21.2 GHz and the uplink from 30 to 31 GHz. There is growing trend in SATCOM systems moving towards Ka-band SATCOM to satisfy the need for more bandwidth and capacity per satellite. HTS and HiCapS are two popular multiple beam SATCOM systems in Ka-band [16]. The application of MU-MIMO spatial multiplexing technique to enhance the channel capacity of a multi spot beam satellites into a single geographical region is presented in Chapter-5.

## 2.2 Literature Review

As the demand for satellite capacity increases, MIMO has emerged as a promising technology to increase the spectral efficiency in SATCOM. The increase in channel capacity comes mainly from utilising the spatial domain, without any increase in bandwidth or power [17].

Interestingly MIMO applicability to SATCOM covers a range of possibilities. A first of a kind, comprehensive review of the MIMO techniques for SATCOM is presented by Arapoglou et al. [18]. This review paper broadly distinguishes the MIMO applicability into Fixed Satellite (FS) and Mobile Satellite (MS) systems. In both cases, the authors consider only satellites that operate in geostationary orbits. The key characteristics of the FS system are fixed location terminals operating in an unobstructed propagation environment at frequency bands above 10 GHz. Meanwhile, the characteristics of an MS system are mobile terminals operating below 10 GHz with different degrees of obstruction in urban, suburban and rural environments.

The FS systems typically require a LOS signal path between the satellite and the earth terminal. The authors in [18] state that the presence of the LOS path and no nearby scatterers at the satellite or the ground terminal make it difficult to achieve independent paths to benefit from MIMO. At the same time, the authors also acknowledge the research presented in [19] to provide MIMO capacity gain through a geometrical optimisation process using two satellites or ground antennas separated by a reasonably large distance. It is also stated that the MU-MIMO is a feasible single satellite MIMO solution for FS systems from a futuristic research and application perspective. The analysis presented in [14] echoes a similar view, suggesting the use of MU-MIMO is a practically feasible opportunity because of the scattered user distribution.

The majority of MIMO SATCOM research activities and analysis has been focused on MS systems, particularly in making use of the dual polarization channel in L-band and S-band. Although simultaneously using orthogonal polarizations is a well known frequency reuse technique in SATCOM, the application of MIMO is aimed at improving the system performance and to offer better isolation for polarization multiplexing. A MIMO simulation framework with polarization is presented in [20] using Alamouti's orthogonal space time block code (OSTBC) for diversity and space time trellis code (STTC) for multiplexing gain. The results show that by using the MIMO method, performance improvement can be achieved in terms of bit error rate (BER) and spectral efficiency.

Some early interest for MIMO in satellite broadcast systems are evidenced by the study report produced by DVB-NGH (Digital Video Broadcasting to Next Generation Hand-held) in mid 2008 [21]. In the DVB-NGH study report, MIMO is identified as a potential enhancement technique in a hybrid satellite-terrestrial architecture for the DVB-SH (Digital Video Broadcast of Satellite to Hand-held terminals) standard. DVB-SH is a mobile satellite standard that came into existence circa mid-2007, which defines the coding and modulation for satellite transmissions to hand-held devices [22].

### Land Mobile Satellite Channel

Modelling and measurement of the land mobile satellite (LMS) MIMO channel is presented in King's Ph.D thesis [23]. The focus of the thesis is to characterize the LMS MIMO channel between a satellite and a mobile user terminal. A statistical LMS MIMO channel model was derived to simulate the effects of multiple satellites and/or dual polarization under different propagation environments [24]. Extensive measurements were made to validate the channel model with an artificial satellite platform on a hill top. The measurement setup included two hill mounted spatially separated antenna masts, where each mast contained a LHCP (Left Hand Circularly Polarized) and a RHCP (Right Hand Circularly Polarized) antenna adjacently mounted. The mobile platform included four omni directional antennas atop a vehicle, two in each polarization. Although the measurement captured a $4 \times 4$ dual polarized channel, only a $2 \times 2$ was analysed in depth, as it was seen that a single satellite dual polarized system was a more commercially viable option. Some key findings from the King's LMS channel characterisation measurements were:

- Under LOS conditions, the multipath effects in the $2 \times 2$ channel matrix are reduced and enough isolation was naturally seen between the two polarizations. In this case, the channel induced depolarization is minimal and the cross polar isolation in the link is dominated by the antenna's ability to distinguish between the polarizations.

- In obstructed LOS channel environments, the multipath effects are more pronounced and the Ricean factor $K$ reduces towards a Rayleigh channel. Under Non-Line of Sight (NLOS) conditions, the $2 \times 2$ LMS polarization MIMO channel shows four weakly correlated Rayleigh fading coefficients.

- Based on the capacity analysis of the measurement data, a doubling of capacity is seen between SISO and $2 \times 2$ MIMO at high SNR's due to good isolation between the polarizations. However, at low SNRs, a much greater capacity ratio increase is available due to four fold increase in the diversity order under Rayleigh channel conditions.

### MIMOSA

MIMOSA (characterisation of the MIMO channel for mobile satellite systems) [25] was an European Space Agency (ESA) project started at the end of 2010. The main objective of this project was to study the fading characteristics of the LMS channel and to analyse the MIMO applicability while utilising polarization and satellite diversity. The examined frequency bands were S and L band. An extensive channel measurement campaign was carried out around Erlangen in Germany, using the Solaris payload of the EUTELSAT-10A satellite. A multi-tone test signal was transmitted in S-band from the satellite in both polarizations (RHCP and LHCP) and the different fading characteristics of the polarization channel was measured. Six omni-directional antennas were used atop the measurement vehicle, but only a $2 \times 2$ subset of the channel was used to study the different spatial antenna positions. The results show different fading characteristics between two differently polarized antennas, for example a flat fading in one antenna and frequency selective fading in another. A detailed discussion on the measurement results and channel modelling are discussed in [26].

### Spatial Geometrical Optimization

In the LOS environment, it is known that MIMO can achieve extra spatial degrees of freedom using geographically separated antennas either at the transmitter or at the receiver [27]. The construction of an orthogonal MIMO channel for SATCOM through geometrical optimisation method was first presented in [19]. Since then, Prof. Knopp and his team at the Munich University of the Bundeswehr have presented a number of research activities analysing the MIMO channel capacity, channel atmospheric impairments, practical trade-offs, applications and MIMO SATCOM channel measurements [7, 28, 29, 30, 31].

In [19], the authors show that a satellite to ground MIMO communication link can achieve maximum spectral efficiency gain in spite of LOS propagation. The spatial multiplexing gain is achieved by geometrical optimisation process to obtain distinct phase relationship in the channel matrix using the range (distance) between the satellite and ground antennas. Since the phase in the channel paths are a function of carrier frequency and range distances, at a given frequency a distinct phase relationship can be obtained in the channel matrix by optimised antenna placements. Due to the large range distance and small relative displacement of the ground antennas, a single satellite architecture often cannot satisfy the spacing constraints required for MIMO. Hence a multi-satellite solution is initially proposed in [19] to enable closer antenna spacing on the ground. In [7], practical constraints are taken into account and the authors present a view that MIMO capacity enhancement using multiple satellites could be undesirable, due to economical considerations.

A single satellite MIMO approach is presented in [29] with displaced ground antennas for a broadband military SATCOM application. In the single satellite example, the antennas on-board the satellite are separated by 6 m and this requires the antennas on the ground to be separated by approximately 68 km and 77 km for a 14 GHz uplink and 12 GHz downlink, respectively. Although the antennas on the ground are separated by many kilometres, they are required to be connected by a fibre network in both the uplink and the downlink to achieve full spatial multiplexing gain. Large ground antenna displacement on both the uplink and the downlink will introduce a large propagation delay difference in the channel path and can introduce severe inter symbol interference (ISI) in the channel. To overcome this problem, use of a block based Single Carrier Frequency Domain Equalisation (SC-FDE) transmission scheme was proposed and analysed in [30].

The theoretical model for the geometrical positioning of the antennas to achieve the orthogonality in the MIMO channel matrix has been proven by experiments [31]. The authors [31] present a proof of concept using two Ku-band satellites: EUTELSAT-7B and EUTELSAT-10A in the $7^o$ E and $10^o$ E orbital locations, respectively. Both the satellites have transponded payloads with a small shared frequency spectrum in Ku-band. The experiment involved transmitting to the satellites using two SISO uplinks with MIMO in the downlink at 12 GHz. The authors were able to successfully verify and prove the theoretical predictions for channel capacity.

### MU-MIMO for Multi-beam Satellites

There are two fundamental advantages of MU-MIMO over the more traditional single user or point-to-point MIMO: First, it can favourably work in the LOS propagation environment and second, MU-MIMO requires only single antenna terminals [5]. Next generation geostationary SATCOM systems in Ka-band are aggressive in-terms of throughput and capacity. HTS and HiCapS are the two main categories of satellite systems that have emerged [32, 16]. A HTS system typically consists of several fixed spot beams covering multiple small footprints on the ground. The main aim of a HTS system is to increase the overall throughput of a satellite by frequency reuse across the spot beams, using at-least four or more colours [33]. Spot beams with different colours differ in frequency or polarization. Reducing the number of colours in a HTS system will increase the bandwidth in each spot and can boost the overall throughput, at the cost of increased interference for users at the edge of the beams. The application of MU-MIMO, precoding and multi-user detection (MUD) techniques have been been analysed to mitigate the interference [34, 35, 36, 37] and these studies show an improvement in the system performance.

## 2.3 Spatial Multiplexing in SATCOM

In the LOS environment, to utilise spatial degrees of freedom gain, antenna separation in the order of hundreds of kilometres is required either at the satellite or on the ground. Since the antenna spacing on-board a single satellite will be limited to few meters, larger geographically separated antennas on the ground are required to achieve the orthogonality in the MIMO channel matrix.

An example is shown in Figure 2.2, where there are $N = 2$ antennas on the ground separated by a distance $\mathrm{d_G}$ and $M = 2$ antennas on-board the satellite separated by a small distance $\mathrm{d_S}$. For a MIMO link, it is assumed that the ground terminals are connected terrestrially. The $2 \times 2$ channel matrix of the uplink channel is given as

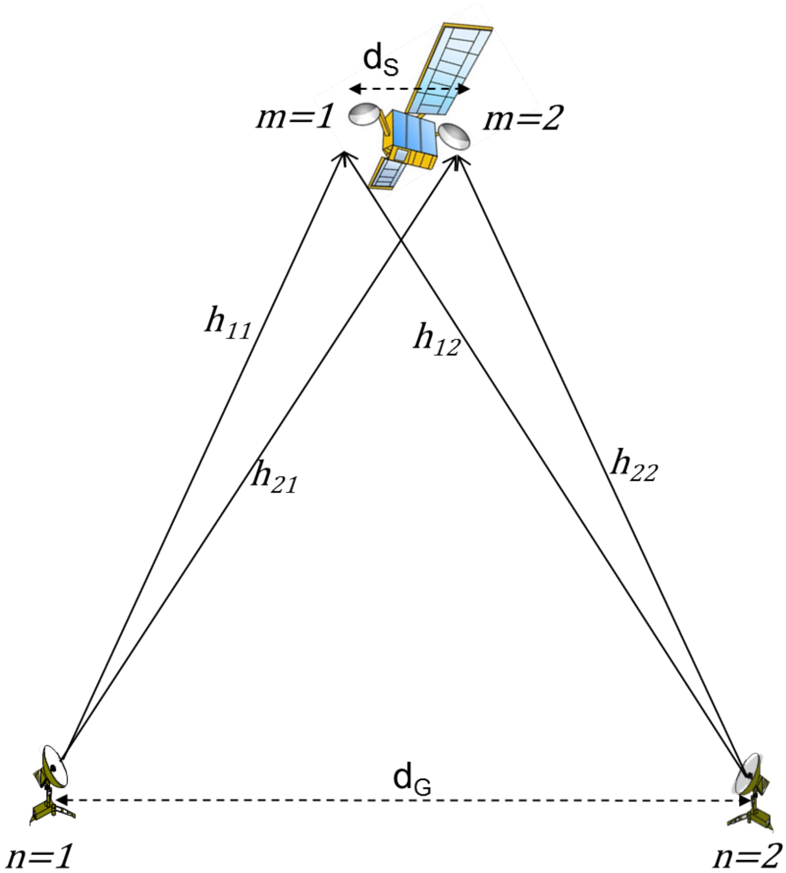


Figure 2.2: Antenna spacing for spatial multiplexing in SATCOM

below:

$$\mathbf{H} = \begin{pmatrix} h_{11} & h_{12} \\ h_{21} & h_{22} \end{pmatrix}, \tag{2.1}$$

$$h_{mn} = a_{mn} g_{mn} e^{-j\phi_{mn}}, \tag{2.2}$$

where $a_{mn}$ denotes channel path attenuation, $g_{mn}$ denotes the corresponding combined tx/rx antenna gain and $\phi_{mn}$ denotes the deterministic phase component in each channel path element.

$$\phi_{mn} = 2\pi \frac{f}{c} r_{mn}, \tag{2.3}$$

$$a_{mn} = \frac{c}{4\pi f r_{mn}}, \tag{2.4}$$

where $f$ is carrier frequency in Hz, $c$ is speed of light in meters per second and $r_{mn}$ denotes the range distance between the $n^{\text{th}}$ ground terminal and $m^{\text{th}}$ satellite antenna in meters. Based on the geometry ($\mathrm{d_S} \lll \mathrm{d_G}$ and $\mathrm{d_G} \lll r_{mn}$ ), it is reasonable to approximate the channel path attenuation to $a_{mn} \approx a$ and $g_{mn} \approx g$, such that:

$$\mathbf{H} = ag\widetilde{\mathbf{H}}, \tag{2.5}$$

where $\widetilde{\mathbf{H}}$ is the channel phase matrix:

$$\widetilde{\mathbf{H}} = \begin{bmatrix} e^{-j\frac{2\pi f}{c}r_{11}} & e^{-j\frac{2\pi f}{c}r_{12}} \\ e^{-j\frac{2\pi f}{c}r_{21}} & e^{-j\frac{2\pi f}{f}r_{22}} \end{bmatrix}. \tag{2.6}$$

The channel phase matrix is orthogonal if the matrix product $\widetilde{\mathbf{H}}\widetilde{\mathbf{H}}^{\dagger}$ results in a diagonal matrix:

$$\widetilde{\mathbf{H}}\widetilde{\mathbf{H}}^{\dagger} = \begin{bmatrix} e^{-j\frac{2\pi f}{c}r_{11}} & e^{-j\frac{2\pi f}{c}r_{12}} \\ e^{-j\frac{2\pi f}{c}r_{21}} & e^{-j\frac{2\pi f}{f}r_{22}} \end{bmatrix} \begin{bmatrix} e^{j\frac{2\pi f}{c}r_{11}} & e^{j\frac{2\pi f}{c}r_{21}} \\ e^{j\frac{2\pi f}{c}r_{12}} & e^{j\frac{2\pi f}{c}r_{22}} \end{bmatrix} \tag{2.7}$$

$$= \begin{bmatrix} 2 & e^{-j\frac{2\pi f}{c}(r_{11}-r_{21})} + e^{-j\frac{2\pi f}{c}(r_{12}-r_{22})} \\ e^{-j\frac{2\pi f}{c}(r_{21}-r_{11})} + e^{-j\frac{2\pi f}{c}(r_{22}-r_{12})} & 2 \end{bmatrix}. \tag{2.8}$$

The off-diagonal elements of $\widetilde{\mathbf{H}}\widetilde{\mathbf{H}}^{\dagger}$ are complex conjugate to each other. A geometrical optimisation is required to obtain a distinct range relationship in the channel matrix so that the off-diagonal elements can be zero [19]:

$$(r_{11} - r_{21}) - (r_{12} - r_{22}) = \frac{\nu}{2}\frac{c}{f}, \tag{2.9}$$

where $\nu$ is a periodic factor and must be an integer indivisible by 2. After substituting (2.9) in (2.8), the matrix product $\widetilde{\mathbf{H}}\widetilde{\mathbf{H}}^{\dagger}$ results in a diagonal matrix, where both spatial multiplexing and beamforming gain can be achieved:

$$\widetilde{\mathbf{H}}\widetilde{\mathbf{H}}^{\dagger} = \begin{bmatrix} 2 & 0 \\ 0 & 2 \end{bmatrix}. \tag{2.10}$$

In the geostationary SATCOM scenario the range distance $r$ is very large. To satisfy (2.9), large geometrical spacing $\mathrm{d_G}$ is required for terminals located on the Earth's surface, the value of which depends on $\mathrm{d_S}$ and $f$. For example if $\mathrm{d_S} = 3$ m, a

$\mathrm{d_G}$ of approximately 260 km and 70 km antenna separation for X-band (8 GHz) and Ka-band (30 GHz), respectively, is required.

Although spatial multiplexing is achievable in the LOS dominated SATCOM scenarios, the practical drawback is the requirement for large antenna separation on the ground. Practical application scenarios for MIMO spatial multiplexing in SATCOM using multiple satellites are discussed in Chapter-3 and Chapter-4. A single satellite MIMO application scenario using multiple users is discussed in Chapter-5.

## 2.4 MIMO Channel Capacity

The most direct method to characterise the performance of a MIMO system is by analysing the achievable channel capacity in terms of spectral efficiency in bits/s/Hz. Consider a MIMO system with $N$ transmit antennas and $M$ receive antennas. For a time invariant channel, the system transfer function can be expressed by simple linear equation:

$$\mathbf{y} = \mathbf{H}\mathbf{x} + \mathbf{w}, \tag{2.11}$$

where $\mathbf{x} \in \mathbb{C}^{N\times 1}$ denotes transmitted signal vector from $N$ antennas, $\mathbf{y} \in \mathbb{C}^{M\times 1}$ denotes received signal vector from $M$ antennas and $\mathbf{w} \sim \mathcal{CN}(0, \sigma_w^2 \mathbf{I}_M)$ denotes zero mean additive white complex Gaussian noise vector, where $\sigma_w^2$ is the noise power at each receive antenna and $\mathbf{I}$ denotes identity matrix. Each element of the channel matrix $\mathbf{H} \in \mathbb{C}^{M\times N}$ is a complex coefficient denoted by $h_{mn}$, where $m \in 1, 2...M$ and $n \in 1, 2...N$:

$$\mathbf{H} = \begin{pmatrix} h_{11} & h_{12} & . & . & h_{1N} \\ h_{21} & h_{22} & . & . & h_{2N} \\ . & . & . & . & . \\ . & . & . & . & . \\ h_{M1} & h_{M2} & . & . & h_{MN} \end{pmatrix}. \tag{2.12}$$

Shannon's channel capacity theorem can be extended to yield the following formula, where the channel capacity can be expressed by calculating the log-determinant of the matrix [6]:

$$C = \log_2 \det \left( \mathbf{I}_M + \frac{S}{N\sigma_w^2} \mathbf{H}\mathbf{H}^\dagger \right) \qquad \text{bits/s/Hz}, \tag{2.13}$$

where $C$ denotes the channel capacity in bits per seconds per Hz, det(.) denotes the determinant operation, † denotes Hermitian transpose and $S$ denotes the total transmit signal power. Equation (2.13) assumes the channel state information is available at the receiver.

### 2.4.1 Singular Value Decomposition

Singular Value Decomposition (SVD) is a useful technique to decompose and analyse a channel's spatial degree of freedom [27]. The SVD process works under the assumption that the channel matrix $\mathbf{H}$ is known both at the transmitter and at the receiver. The channel matrix can be decomposed using the SVD technique. Let,

$$\mathbf{H} = \mathbf{U}\mathbf{\Lambda}\mathbf{V}^\dagger, \tag{2.14}$$

where $\mathbf{U} \in \mathbb{C}^{M\times M}$, $\mathbf{V} \in \mathbb{C}^{N\times N}$ are both unitary matrices and $\mathbf{\Lambda} \in \Re^{M\times N}$ is a singular value matrix.

$$\mathbf{\Lambda} = \begin{pmatrix} \lambda_1 & 0 & . & . & 0 \\ 0 & \lambda_2 & . & . & 0 \\ . & . & . & . & . \\ . & . & . & . & . \\ 0 & 0 & . & . & \lambda_k \end{pmatrix}, \tag{2.15}$$

$$k \leq \min\{M, N\}, \tag{2.16}$$

where $k$ denotes the rank of the matrix $\mathbf{H}$. The diagonal elements of $\mathbf{\Lambda}$ are non-negative real entries called the singular values ($\lambda_1 \geq \lambda_2 \geq ...\lambda_k$) and the off-diagonal elements of $\mathbf{\Lambda}$ are zeros.

Figure 2.3 shows the SVD processing blocks that include the transmit precoder ($\mathbf{V}$), channel and receiver preprocessing ($\mathbf{U}^\dagger$). The transmit vector before and after precoding are denoted by $\widetilde{\mathbf{x}}$ and $\mathbf{x}$, respectively, and the received signal vector before and after preprocessing are denoted by $\mathbf{y}$ and $\widetilde{\mathbf{y}}$, respectively.

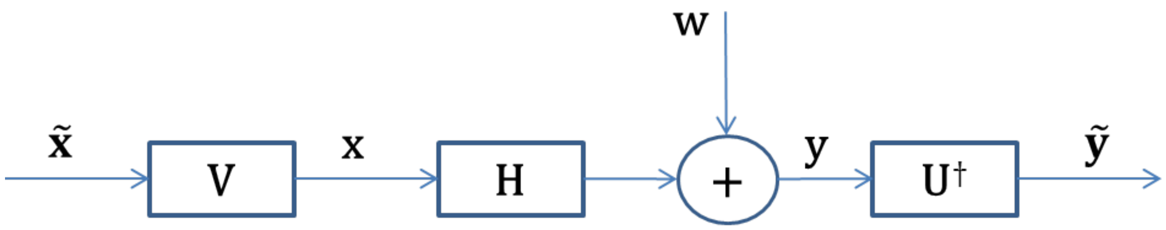


Figure 2.3: SVD Processing

The received signal vector from (2.11) can be expressed as below:

$$\begin{aligned} \mathbf{y} &= \mathbf{H}\mathbf{V}\widetilde{\mathbf{x}} + \mathbf{w} && (2.17) \\ &= \mathbf{U}\boldsymbol{\Lambda}\mathbf{V}^{\dagger}\mathbf{V}\widetilde{\mathbf{x}} + \mathbf{w} && (2.18) \\ &= \mathbf{U}\boldsymbol{\Lambda}\widetilde{\mathbf{x}} + \mathbf{w}, && (2.19) \end{aligned}$$

and after receive preprocessing:

$$\begin{aligned} \widetilde{\mathbf{y}} &= \mathbf{U}^{\dagger}\mathbf{y} && (2.20) \\ &= \mathbf{U}^{\dagger}\mathbf{U}\boldsymbol{\Lambda}\widetilde{\mathbf{x}} + \mathbf{U}^{\dagger}\mathbf{w} && (2.21) \\ &= \boldsymbol{\Lambda}\widetilde{\mathbf{x}} + \widetilde{\mathbf{w}}. && (2.22) \end{aligned}$$

Since $\mathbf{U}$ is a unitary matrix, the distribution of $\widetilde{\mathbf{w}}$ is same as $\mathbf{w}$. The SVD process effectively divides the channel into multiple parallel paths, where up to $k$ parallel data streams can be transmitted with no mutual interference. The sum capacity of the channel is given by [27]:

$$C = \sum_{i=1}^{k} \log_2(1 + \frac{S_i}{\sigma_w^2}\lambda_i^2) \qquad \text{bits/s/Hz}, \tag{2.23}$$

where $S_1, ....S_k$ are power allocations corresponding to each respective data stream, with the constraint that:

$$S = \sum_{i}^{k} S_i. \tag{2.24}$$

The rank, $k$, in each scenario is equal to $\min\{M, N\}$. (2.24) constraints the total transmit signal power, $S$, to be a constant irrespective of the total number of transmit antennas. The channel capacity scenarios for MIMO and SISO are shown in Figure 2.4. A best case example is considered for each MIMO scenario, where the channel matrix in each MIMO scenario is fully orthogonal and takes advantage of both spatial multiplexing and array gains. In a square MIMO channel, where $M = N$, all the channel singular values will be equal, as $\lambda_1 = \lambda_2 = ...\lambda_k = \sqrt{k}$. The capacity plot shows that the channel capacity increases linearly with increase in MIMO order.

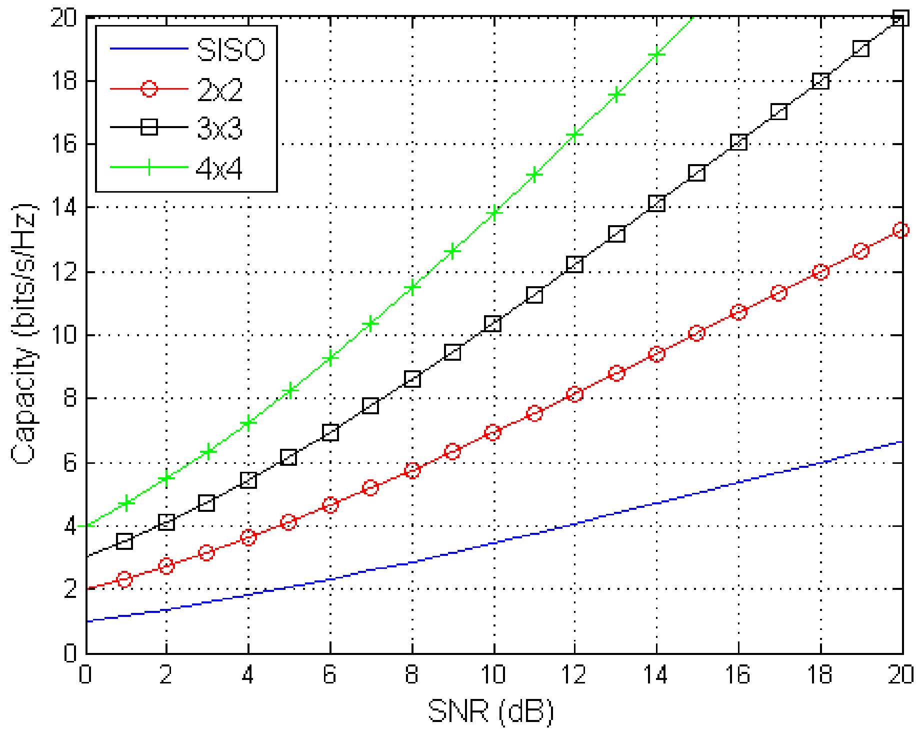


Figure 2.4: MIMO channel capacity

In the above example, since the channel singular values are equal, optimum capacity is achieved by equal power allocation to each data stream. However, in a non-ideal case, where the MIMO channel matrix is not perfectly orthogonal, the channel capacity decreases. Power allocation using the water-filling method has been proven to be an optimum strategy to maximize capacity [27]. Recall that the underlying assumption in using the SVD process is that the Channel State Information (CSI) is available at both the transmitter and the receiver. Since CSI at the transmitter (CSIT) is available, the capacity can be maximised by using waterfilling power allocation for non-ideal channels.

$$S_i = \left(\mu - \frac{N_o}{\lambda_i^2}\right)^+, \tag{2.25}$$

where $\mu$ is a parameter chosen to satisfy the total power constraint in (2.24) and $(x)^+$ denotes $\max\{0, x\}$. The waterfilling method allocates more power to the data stream with highest singular value.

An example case with a non-ideal $4 \times 4$ channel is shown in Figure 2.5. The channel singular values are $\lambda_1 = 2.67$, $\lambda_2 = 2.55$, $\lambda_3 = 1.52$ and $\lambda_4 = 0.28$. The distribution of the channel singular values is a measure of the orthogonality of the channel. The channel is fully orthogonal if all the singular values are equal. In Figure 2.5, it is shown that the capacity of the non-ideal channel is less compared to the ideal case. However, by using waterfilling power allocation the capacity can be increased especially at low SNRs, while at high SNRs the waterfilling power allocation performance converges to equal power allocation method.

### 2.4.2 Beamforming Gain

The generalised assumption to achieve a full rank MIMO channel matrix is that there is sufficient scattering in the propagation environment so that the capacity linearly scales with $\min\{M, N\}$. In a LOS only propagation environment large antenna separation is required either at the transmitter or receiver to obtain extra spatial degrees of freedom gain [27]. Insufficient antenna spacing will lead to strong correlation between the channel path elements reducing the available spatial degrees of freedom to one. In these channel scenario, multiple antennas at the transmitter and receiver therefore only benefit from beamforming gain. In transmit beamforming, the phase and amplitude of

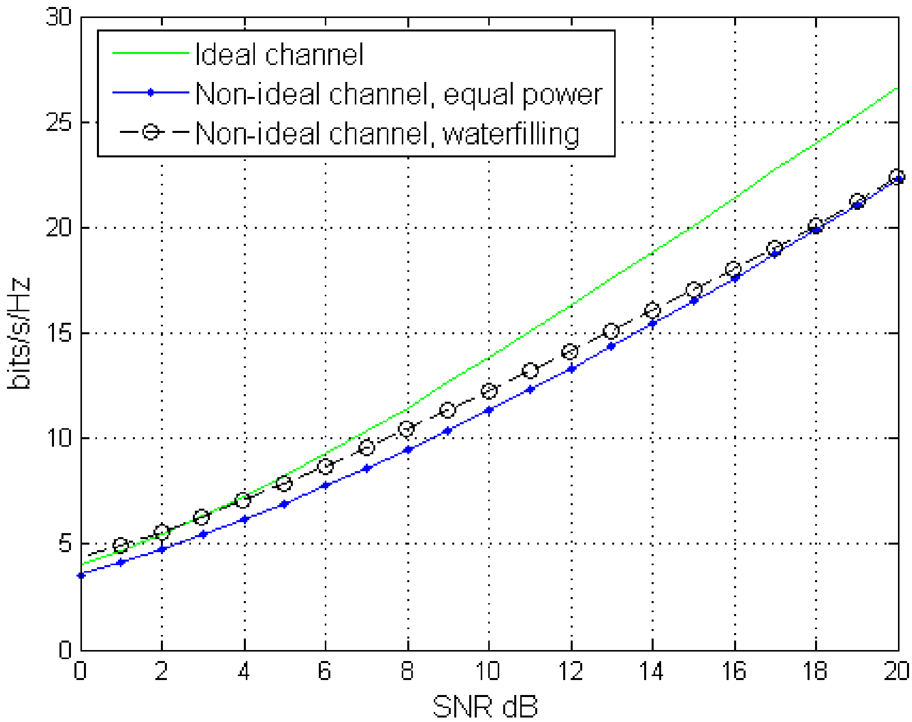


Figure 2.5: Comparison of waterfilling and equal power allocation in $4 \times 4$ MIMO channel scenario

the signal from each transmit antenna are adjusted so that they add constructively at the receiver [38]. In the receive beamforming case, the receive signals from each antenna are combined constructively to maximize the SNR. Thus an increase in channel capacity can be shown with respect to beamforming gain, equivalently called as power or array gain. The rank of this channel ultimately reduces to $k = 1$, with only one non-zero singular value $\lambda_1 = a\sqrt{MN}$ [27]. The achievable capacity is then;

$$C = \log_2 (1 + \frac{S}{\sigma_w^2} a^2 MN) \qquad \text{bits/s/Hz.} \tag{2.26}$$

# Chapter 3

# MIMO Spatial Multiplexing: Multi-Satellite Systems

To gain the full advantage of MIMO spatial multiplexing in LOS dominated SATCOM channels, it is known that the antennas either in space or at the ground must be separated by a large distance. This introduces a practical difficulty for the single satellite scenario, due to the spacing constraint on-board the satellite for large antenna displacement. On the other hand, multiple antennas hosted on multiple satellites in different orbital slots can enable closer antenna spacing for a ground user. In X, Ku or Ka bands, a MIMO SATCOM approach using two satellites within an orbital separation between $0.5^o$ and $2^o$ can boost the overall channel capacity in a high demand geographical region [39] [40]. Typically, geostationary satellites with overlapping frequency bands are not placed in orbits at a narrow spacing in order to avoid adjacent satellite interference. At the same time, to use two satellites for spatial multiplexing may not always be considered cost effective, given the high cost to launch and operate each satellite [7].

However, UHF and narrowband MILSATCOM is one example where MIMO can be most useful to increase the spectral efficiency using two satellites. MILSATCOM normally uses UHF for low data rate applications with bandwidths of 5 kHz and 25 kHz channels. The conventional frequency allocation for a UHF MILSATCOM downlink is between 244 and 270 MHz and uplink between 292 and 317 MHz [41].

Some advantages that are unique to UHF SATCOM are its ability to penetrate into buildings and foliage, robustness to adverse weather conditions and small portable user terminals (UTs) that are low cost and easy to deploy [42, 43]. The UHF UTs have broad beamwidths so that precise pointing to the target satellite is not a requirement for mobile users. The beamwidth for a typical UHF terminal is very broad. For example the 3 dB beamwidth of a terminal with a 7 dBi gain is approximately 75 degrees. Strict frequency and orbital coordination are in place to avoid interference issues with other satellites. At the same time, some inherent disadvantages of UHF SATCOM are limited bandwidth and significant restrictions on applying frequency reuse in the geo-stationary arc resulting in low capacity. Hence capacity is a scarce resource in the UHF band and it is a challenge to efficiently use the available spectrum.

To enable MIMO SATCOM in UHF band, the required orbital separation between geostationary satellites with UHF payloads is between $30^o$ and $45^o$ degrees to achieve MIMO spatial multiplexing gain. This approach makes use of the broad antenna beamwidths of an UHF UT. The main thrust of this chapter is to analyse the applicability of MIMO to UHF SATCOM to address the capacity limitation and the challenges therein.

A system model is introduced in Section-3.1. The MIMO link channel is considered only for the user side at the UHF band, either in the uplink or downlink. Whereas, the satellites to anchor or vice-versa is via two SISO links. In Sections-3.2 and 3.3, channel modelling and capacity analysis are addressed, respectively, assuming a Ricean distribution in the MIMO channel. The receiver signal processing architectures in both user uplink and downlink scenarios are addressed in Section-3.4 and simulation results are presented in Section-3.5. The aspects of satellite orbital drift and its impact on the MIMO channel orthogonality are addressed in Section-3.6.

## 3.1 System Model

The system model is shown in Figure 3.1. Two satellites with UHF payloads are considered in this analysis, separated by an orbital spacing $d_S$. Each satellite payload is a non-regenerative amplify and forward relay. There are two communication scenarios considered; the first is the anchor to user (A2U) scenario and the second is the user to anchor (U2A) scenario. In the A2U scenario, the uplink is two SISO links, with MIMO in the downlink to the user. In the U2A scenario, the uplink is a MIMO channel and the two downlinks to the anchor terminals are SISO.

A MIMO channel in both uplink and downlink, i.e. a user to user (U2U) scenario is avoided. Large propagation time difference between the two satellites will result in a very small coherence bandwidth ($\approx$ 1 kHz). Hence, it is not a practical solution to consider MIMO in a U2U scenario. This is further discussed in Section-3.4.3.

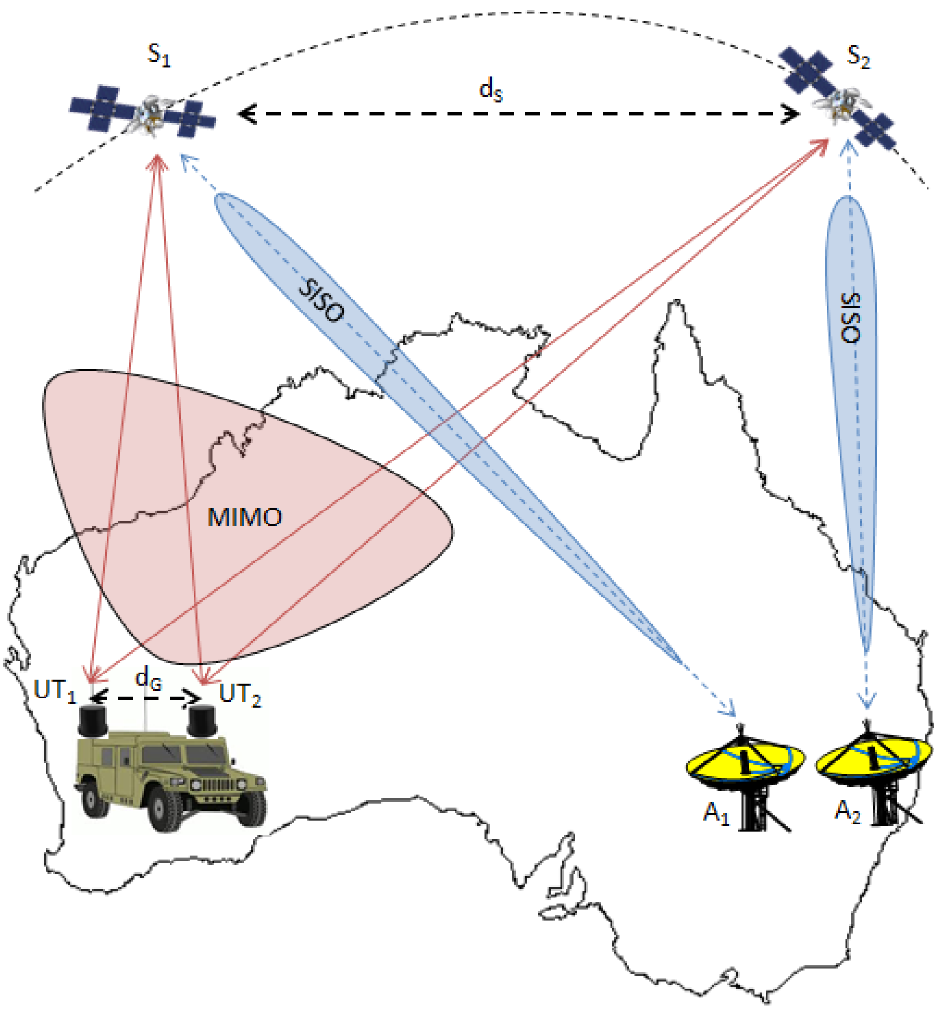


Figure 3.1: MIMO SATCOM system model in UHF band: (A2U) two SISO uplinks plus MIMO downlink, and (U2A) MIMO uplink and two SISO downlinks

Table 3.1: System parameters for MIMO SATCOM in UHF band

| **Parameter** | **Value** |
|---|---|
| $S_1$ orbital position | $120^o$ E |
| $S_2$ orbital position | $150^o$ E |
| $UT_1$ and $UT_2$ locations | $28^o$S $114^o$E |
| $A_1$ and $A_2$ locations | $33^o$S $151^o$E |
| $d_G$ | $\approx 1$ m |
| UHF uplink $f_u$ | 292 MHz |
| UHF downlink $f_d$ | 244 MHz |

Each anchor terminal has a narrow antenna beamwidth. The anchor to satellite link and satellite to anchor link can be either in UHF or in other bands, such as Ka or X. The approximate spacing between the UTs ($d_G$), orbital location for $S_1$ and $S_2$, anchor terminal location for $A_1$ and $A_2$, and UT location are listed in Table 3.1. The location of the satellites, the UTs and the anchor stations are notional values for the purpose of analysis.

## 3.2 Channel Modelling

A generic channel model is considered in this analysis, with $N$ antennas at the source, $M$ satellites (each with one uplink and one downlink antenna) and $Z$ antennas at the destination. The source can be either the anchor or the UHF user and similarly the destination can be either the anchor or UHF user. In the example shown in Figure 3.2, there are $N = 2$ transmit antennas at source, $M = 2$ satellites and $Z = 2$ receive antennas at destination. The spatial dimension for multiplexing can be increased beyond two, that is by increasing the number of satellites and antennas on the ground. However, the analysis is restricted to $M = 2$ for practical consideration. In Chapter-5, an analysis is presented to increase the spatial dimension beyond two, but it should be noted that it is a different system model, using multiple single antenna users in a single satellite system with multiple antennas.

The uplink and the downlink channel matrices are denoted by $\mathbf{H}_u \in \mathbb{C}^{M\times N}$ and $\mathbf{H}_d \in \mathbb{C}^{Z\times M}$, respectively. In this analysis, since the MIMO channel is considered either in the uplink or the downlink, the off-diagonal gain values in $\mathbf{H}_u$ or $\mathbf{H}_d$ will be substituted to zeros depending on a U2A scenario or A2U scenario, respectively.

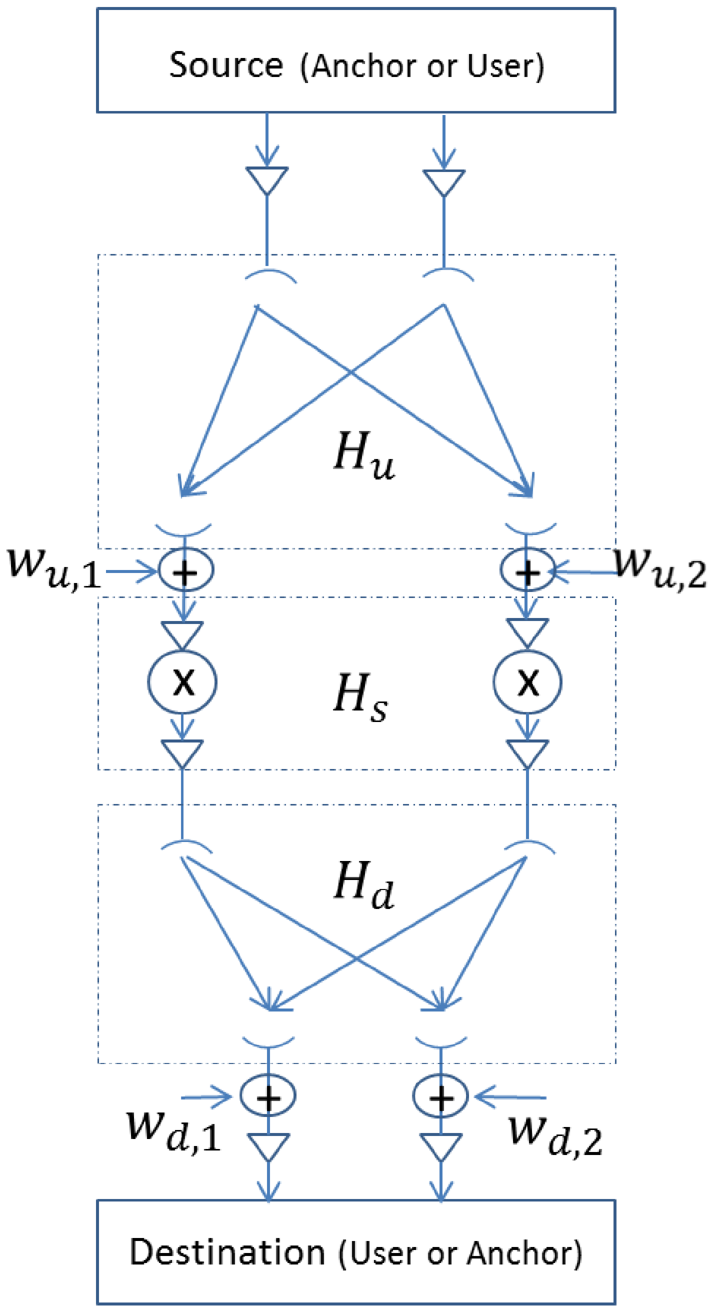


Figure 3.2: Channel model ($N = M = Z = 2$)

In the uplink channel matrix, each LOS channel coefficient $h^{\text{LOS}}_{u,mn}$ includes the channel path attenuation $a_{u,mn}$ from free space path loss, the combined Tx/Rx antenna gain $g_{u,mn}$ and a distinct deterministic channel phase $\phi_{u,mn}$ (2.2):

$$h^{\mathrm{LOS}}_{u,mn} = a_{u,mn}\, g_{u,mn}\, e^{-j\phi_{u,mn}}, \tag{3.1}$$

$$\phi_{u,mn} = 2\pi \frac{f_u}{c} r_{u,mn}, \tag{3.2}$$

$$g_{u,mn} = g^{\mathrm{rx}}_{u,m}\, g^{\mathrm{tx}}_{u,n}, \tag{3.3}$$

where the antenna gain (3.8) is the combination of both transmit and receive antennas and the channel path attenuation is given in (2.4). Due to the specific geometry of the system in Figure 3.1 and assuming equivalent UT antennas, it is reasonable to approximate $a_{u,mn} \approx a_u$ and $g_{u,mn} \approx g_u$ (2.5).

Depending on the channel environment, multipath propagation is typically expected for a UT in the UHF band. The MIMO channel matrix can be modelled using a Ricean distribution to include both LOS and NLOS components. The overall uplink MIMO channel matrix $\mathbf{H}_u$ is sum of both the LOS and NLOS components [18]:

$$\mathbf{H}_u = a_u g_u \widetilde{\mathbf{H}}_u, \tag{3.4}$$

$$\widetilde{\mathbf{H}}_u = \sqrt{\frac{K}{K+1}}\widetilde{\mathbf{H}}^{\mathrm{LOS}}_u + \sqrt{\frac{1}{K+1}}\widetilde{\mathbf{H}}^{\mathrm{NLOS}}_u, \tag{3.5}$$

where $K$ is the Ricean factor which indicates the power ratio between the LOS and NLOS components. The elements of $\widetilde{\mathbf{H}}^{\mathrm{LOS}}_u$ are the deterministic phases from the LOS components ($e^{-j\phi_{u,mn}}$). $\widetilde{\mathbf{H}}^{\mathrm{NLOS}}_u$ represents the NLOS components which are zero mean and stochastic.

Channel measurement results from literature have shown that coherence bandwidth (from local scattering effects at the user) is much higher than 25 kHz [44]. Therefore, it is reasonable to assume flat fading for narrowband UHF SATCOM.

The downlink channel modelling from the satellite to the destination is similar to the uplink channel[1]:

$$h^{\mathrm{LOS}}_{d,zm} = a_{d,zm}\, g_{d,zm}\, e^{-j\phi_{d,zm}}, \tag{3.6}$$

$$\phi_{d,zm} = 2\pi \frac{f_d}{c} r_{d,zm}, \tag{3.7}$$

$$g_{d,zm} = g^{\mathrm{rx}}_{d,z}\, g^{\mathrm{tx}}_{d,m} \tag{3.8}$$

and

$$\mathbf{H}_d = a_d\, g_d\, \widetilde{\mathbf{H}}_d. \tag{3.9}$$

The satellite channel matrix $\mathbf{H}_s \in \mathbb{C}^{M\times M}$ is a simple amplify and forward relay with a gain $g_s$

$$\mathbf{H}_s = g_s\, \widetilde{\mathbf{H}}_s, \tag{3.10}$$

The diagonal entries of $\widetilde{\mathbf{H}}_s$ matrix are $e^{-j\phi_{s,mm}(t)}$ and the the off-diagonal entries are zeros, where $\phi_{s,mm}$ is an arbitrary phase offset in each satellite's transponder path. This phase offset is considered to be a function of time, to model the frequency offset in the respective satellite's path.

## 3.3 Channel Capacity

In Chapter-2, a generalised channel capacity for a point-to-point MIMO system is given in equation (2.13). In this section the capacity calculation is presented in a form that is applicable to a MIMO system with a non-regenerative relay. From [45], the capacity of a MIMO channel with non-regenerative relay is:

$$C = \log_2 \det\left(\mathbf{I}_M + \frac{S}{N\sigma^2_{w,u}}\mathbf{H}_u\mathbf{H}_u^{\dagger} - \frac{S}{N\sigma^2_{w,u}}\mathbf{H}_u\mathbf{H}_u^{\dagger}\mathbf{F}^{-1}\right), \tag{3.11}$$

[1]Recall that in our model only either $\mathbf{H}_u$ or $\mathbf{H}_d$ is a MIMO channel depending on the scenario U2A or A2U, repectively.

$$\mathbf{F} = \mathbf{I}_M + \frac{\sigma_{w,u}^2}{\sigma_{w,d}^2}\mathbf{H}_s^\dagger\mathbf{H}_d^\dagger\mathbf{H}_d\mathbf{H}_s. \tag{3.12}$$

The noise variance corresponding to the noise signals $w_u$ and $w_d$, in the uplink and the downlink are denoted by $\sigma_{w,u}^2$ and $\sigma_{w,d}^2$, respectively. The capacity loss factor $(\frac{S}{N\sigma_{w,u}^2}\mathbf{H}_u\mathbf{H}_u^\dagger\mathbf{F}^{-1})$ in (3.11) is due to the non-regenerative relay. The instantaneous capacity between the source and the destination through a non-regenerative relay link can be calculated using (3.11). An underlying assumption is that $\mathbf{H}_u$ is orthogonal to $\mathbf{H}_d$, which is the case in SATCOM, where the uplink and the downlink are at different frequencies and hence orthogonal in the frequency dimension.

In our work, although the MIMO channel is considered only in a single direction, (3.11) can be used for both U2A and A2U scenarios. The main intention of [45] is to find an optimal relay matrix to maximise the capacity, under the assumption that the relay knows both $\mathbf{H}_u$ and $\mathbf{H}_d$ plus both $\mathbf{H}_u$ and $\mathbf{H}_d$ are orthogonal to each other. In this work, we apply the capacity formulation to the SATCOM scenario; under the assumption that the channel matrix $\mathbf{H}_s$ is diagonal, CSIR is available and CSIT is not available. Similarly, the authors in [29] have also used (3.11) to analyse the capacity in a Ku-band single satellite with displaced ground antenna scenario. An alternate capacity analysis using SVD approach is given and used in Chapter-4, which allows to analyse the spatial plus dual polarization MIMO scenario using transmit power control optimisation techniques.

The terms uplink and downlink carrier power to noise power ratio are most commonly used in a SATCOM link budget. Similarly from a MIMO SATCOM perspective, let's define $\rho_u$ and $\rho_d$ as the uplink and downlink carrier power to noise power ratios respectively:

$$\rho_u = \frac{\mathrm{EIRP}_u}{L_u}\frac{G_u^{\mathrm{rx}}}{\sigma_{w,u}^2}, \tag{3.13}$$

$$\rho_d = \frac{\mathrm{EIRP}_d}{L_d}\frac{G_d^{\mathrm{rx}}}{\sigma_{w,d}^2}, \tag{3.14}$$

where $\mathrm{EIRP}_u$ and $\mathrm{EIRP}_d$ are total equivalent isotropic radiated power in the direction of the receiver in the uplink and the downlink, respectively. $L_u = \left(\frac{1}{a_u}\right)^2$ and $L_d = \left(\frac{1}{a_d}\right)^2$ are path loss in the uplink and the downlink respectively, $G_u^{tx} = (g_u^{tx})^2$ and $G_u^{\mathrm{rx}} = (g_u^{\mathrm{rx}})^2$

are respective transmit and receive antenna power gains in the uplink, $G_d^{tx} = (g_d^{tx})^2$ and $G_d^{\text{rx}} = (g_d^{\text{rx}})^2$ are respective transmit and receive antenna power gains in the downlink and $G_s = (g_s)^2$ is power gain achieved inside the satellite transponder.

In the U2A scenario, the downlink $\text{EIRP}_d$ in (3.16) achieves a gain $\eta$, due to the power gain in the diagonal elements of $\mathbf{H}_u\mathbf{H}_u^\dagger$ as shown in (2.10); such that $\eta = M$ if the uplink is a MIMO channel or $\eta = 1$ if the uplink constitutes $M$ SISO paths:

$$\text{EIRP}_u = SG_u^{\text{tx}} \tag{3.15}$$

and

$$\text{EIRP}_d = \eta \, \frac{\text{EIRP}_u}{L_u} \, G_u^{rx} \, G_s \, G_d^{tx}. \tag{3.16}$$

However, in order to keep the overall satellite power emission as a constant, each satellite transponder gain ($g_s$) is scaled by $\sqrt{\eta}$, such that irrespective of a MIMO uplink or not, (3.16) remains the same. This ensures a fair comparison between MIMO scheme (either in A2U or U2A) and a conventional single satellite SISO SATCOM system.

After substituting (3.13) to (3.16) in (3.11), the MIMO capacity can be expressed using $\rho_u$ and $\rho_d$:

$$C = \log_2 \det\left(\mathbf{I}_M + \frac{\rho_u}{N}\widetilde{\mathbf{H}}_u\widetilde{\mathbf{H}}_u^\dagger - \frac{\rho_u}{N}\widetilde{\mathbf{H}}_u\widetilde{\mathbf{H}}_u^\dagger\mathbf{F}^{-1}\right), \tag{3.17}$$

$$\mathbf{F} = \mathbf{I}_M + \frac{1}{\eta}\frac{\rho_d}{\rho_u}\widetilde{\mathbf{H}}_s^\dagger\widetilde{\mathbf{H}}_d^\dagger\widetilde{\mathbf{H}}_d\widetilde{\mathbf{H}}_s. \tag{3.18}$$

In the case when $N = M = Z = 1$ and $|\widetilde{\mathbf{H}}_u|^2 = |\widetilde{\mathbf{H}}_s|^2 = |\widetilde{\mathbf{H}}_d|^2 = 1$ and noting that:

$$\frac{1}{\rho_t} = \frac{1}{\rho_u} + \frac{1}{\rho_d}, \tag{3.19}$$

where $\rho_t$ is the overall carrier power to noise power ratio [46]. The channel capacity (3.17) reduces to the well known Shannon's channel capacity equation for a single satellite SISO case.

$$C_{\text{SISO}} = \log_2(1 + \rho_t) \quad \text{bits/s/Hz}. \tag{3.20}$$

### 3.3.1 Channel Orthogonality

For best performance, a distinct phase relationship in the uplink and downlink channel paths are required in equations (3.2) and (3.7) to achieve an orthogonal channel transfer matrix for an uplink or downlink LOS MIMO channel respectively. In Chapter-2, it was shown that for a SATCOM channel dominated by the LOS signal path, antenna separations in the order of hundreds of kilometres are required either on the ground or in space. Since $\mathrm{d_S}$ is large with $M = 2$ satellites in the UHF scenario under consideration, a small spacing on the ground $\mathrm{d_G}$ is sufficient for UHF user terminals. Geometrical optimisation of channel orthogonality requires specific range relationships in the uplink channel matrix for U2A scenario. Extending (2.9) for $N$ antennas at the UT, we obtain:

$$(r_{u,1i} - r_{u,2i}) - (r_{u,1l} - r_{u,2l}) = (l - i)\frac{\nu}{N}\frac{c}{f_u} \qquad i, l \in \{1..N\}, \tag{3.21}$$

where $\nu$ is an integer-valued phase periodic factor and the greatest common divisor between $\nu$ and $N$ must be equal to one. The same spacing relationship holds true for MIMO downlink in the A2U scenario, however, in a reversed order, where $Z$ and $f_d$ replace $N$ and $f_u$ respectively

$$(r_{d,i1} - r_{d,l1}) - (r_{d,i2} - r_{d,l2}) = (l - i)\frac{\nu}{Z}\frac{c}{f_d} \qquad i, l \in \{1..Z\}, \tag{3.22}$$

where the greatest common divisor between $\nu$ and $Z$ must be equal to one. The range relationships in (3.21) and (3.22) are derived from (2.9), but the user antennas on the ground are modelled as generic quantities $N$ and $Z$. However, note that the number of spatial degrees of freedom or the rank of the channel matrix cannot be greater than two, because the number of satellites in space is $M = 2$.

### 3.3.2 Capacity Analysis

The mean capacity for SISO and MIMO channels are plotted in Figure 3.3 and Figure 3.4 for the A2U and U2A scenarios, respectively, as a function of $\mathrm{d_G}$ based on (3.17), where the SNR $\rho_u = \rho_d$ =13 dB. The analysis assumes a flat fading channel, i.i.d $\tilde{H}^{NLOS}$ [2] with two cases, $K = 100$ and $K = 10$. The $K$ values are chosen to emulate the likely channel scenarios where the LOS paths are dominant [44].

The mean capacity is calculated using ten thousand different random NLOS channel values. The impact of the inter-antenna spacing $\mathrm{d_G}$ on the achievable capacity for the A2U scenario can be seen in Figure 3.3. In the MIMO scenario the channel capacity is maximised when the inter-antenna spacing is 1.15 m, 3.45 m and 5.75 m corresponding to the periodic factor $\nu = 1, 3$ and 5 respectively. Similarly results for the U2A scenario are shown in Figure 3.4, where the channel capacity is maximised when the inter-antenna spacing is 0.96 m, 2.88 m, 4.8 m and 6.72 m corresponding to the periodic factor $\nu = 1, 3, 5$ and 7 respectively. In both the scenarios, the antennas are aligned in E-W (East-West) direction. The optimal inter-antenna spacing requirement will vary with different angular alignment with respect to the E-W direction. This is analysed later in the chapter.

Irrespective of the $K$ values, the results show that the required inter-antenna spacing is determined by the LOS signal paths. At optimal $\mathrm{d_G}$ values, the achievable mean capacity is higher for $k = 100$ than for $K = 10$. This is due to the random phase values from multi-path components affecting the phase relationship of the channel paths. However, it is opposite at worst case $\mathrm{d_G}$ values, where the random phase values from multi-path components increase the average capacity.

The maximum achievable capacity at any of the optimal $\mathrm{d_G}$ values is same in both the A2U and U2A scenarios. At non-optimal $\mathrm{d_G}$ values, the achievable capacity is lower in A2U scenario compared to U2A scenario. This is due to the superposition of satellite noise by a non-orthogonal $\mathbf{H}_d$ matrix. However, this is not the case in U2A scenario where the downlinks are two SISO link, and $\mathbf{H}_d$ is always an orthogonal matrix.

From the UT perspective, a difference in $f_u = 292$ MHz (U2A scenario) and $f_d = 244$ MHz (A2U scenario) requires different optimal antenna spacing requirement for the uplink and the downlink. However for this specific geometry, it can be seen from Figure 3.3 and Figure 3.4 that an inter-antenna spacing of $\mathrm{d_G} = 1\mathrm{m}$ is a good compromise and achieves a capacity close to the optimal in both U2A and A2U

[2] independent and identical distribution

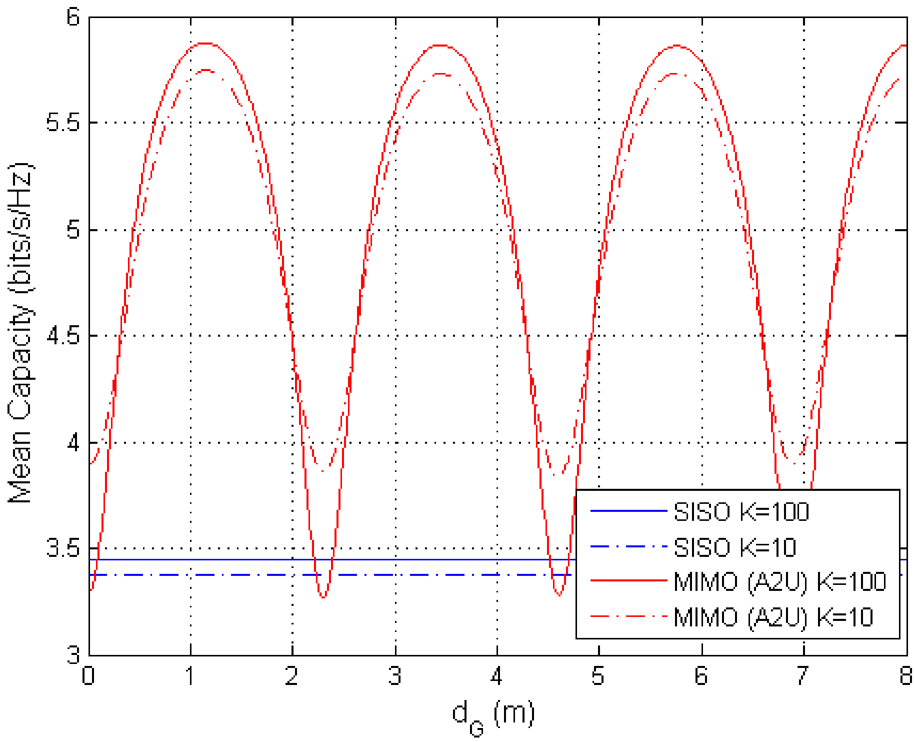


Figure 3.3: Mean capacity analysis using (3.17) in A2U scenario at $\rho_u = \rho_d = 13$ dB; the UTs are stationary in E-W alignment

scenarios. It is also important to note that different locations of the UHF user relative to the satellite position will result in slightly different optimum $\mathrm{d_G}$. Nevertheless, the achievable capacity in the MIMO case is almost doubled compared to the SISO reference case, noting $\mathrm{EIRP}_u$ and $\mathrm{EIRP}_d$ are held to the same sum value in accord with (2.24) irrespective of MIMO or SISO. The mean capacity variation with SNR value is shown in Figure 3.5, with an optimal UT spacing in the A2U scenario. The results compare the MIMO gain with respect to the SISO case.

### 3.3.3 Mobile User

So far in the analysis, the UT antennas have been considered in a fixed orientation in an E-W direction. For mobile vehicles with UT antennas fixed to the vehicle, the orientation with E-W will vary. As the antenna orientation with respect to the E-W changes, a fixed $\mathrm{d_G}$ will violate the spacing requirement as per (3.21) or (3.22) and this will affect system performance. To mitigate this effect, an antenna arrangement

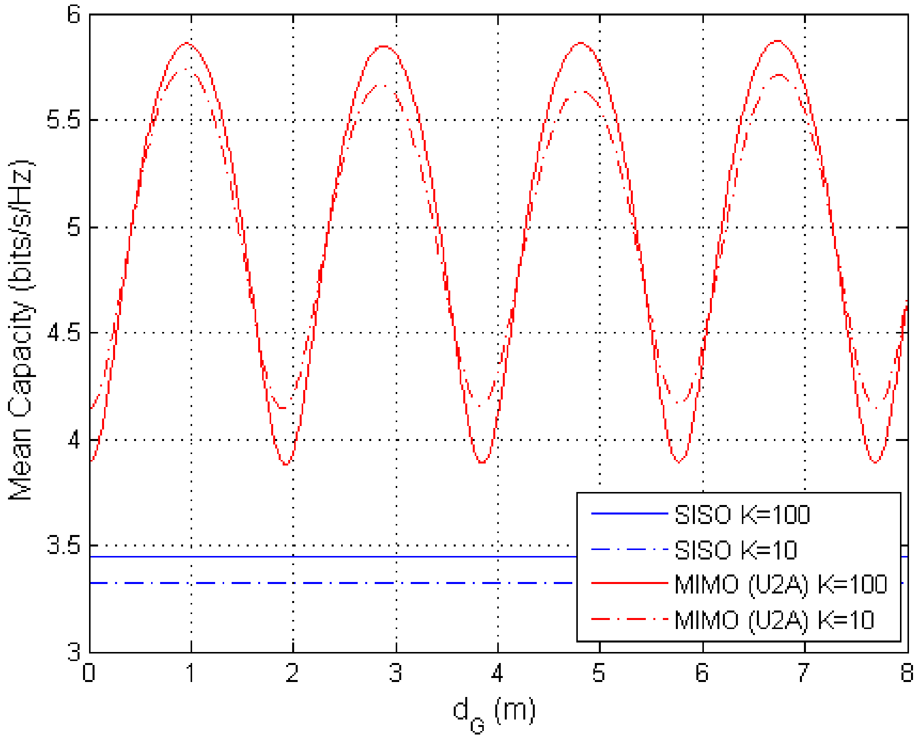


Figure 3.4: Mean capacity analysis using (3.17) in U2A scenario at $\rho_u = \rho_d = 13$ dB; the UTs are stationary in E-W alignment

of three UTs in a triangular arrangement with equal distances ($\mathrm{d_G}$) between each of them is proposed and shown in Figure 3.6. In such an arrangement, perfect channel orthogonality may not be achievable, but the performance degradation will be small compared to optimum positioning of two terminals. The angle $\delta_\mathrm{G}$ is the orientation of the antenna array with respect to the local E-W direction.

The capacity analysis from Figure 3.3 is expanded to include the triangular antenna orientation case with $Z = 3$, as shown in Figure 3.7 for the A2U scenario with $K = 100$. A small increase in capacity compared to $Z = 2$ case is due to the array gain. The impact from the orientation of the UT antenna array is shown in Figure 3.8, the y-axis denotes normalised capacity. In the $Z = 2$ case, with the optimum inter-antenna spacing $\mathrm{d_G} = 1.15$ m from Figure 3.3, it can be seen that the capacity drops significantly with varying $\delta_\mathrm{G}$. However, the capacity degradation in the triangular antenna setup using $Z = 3$ UTs in the A2U scenario is relatively insensitive to the orientation angle. The capacity may not be “optimal ” at all $\delta_\mathrm{G}$ values, but remains above 98% of the

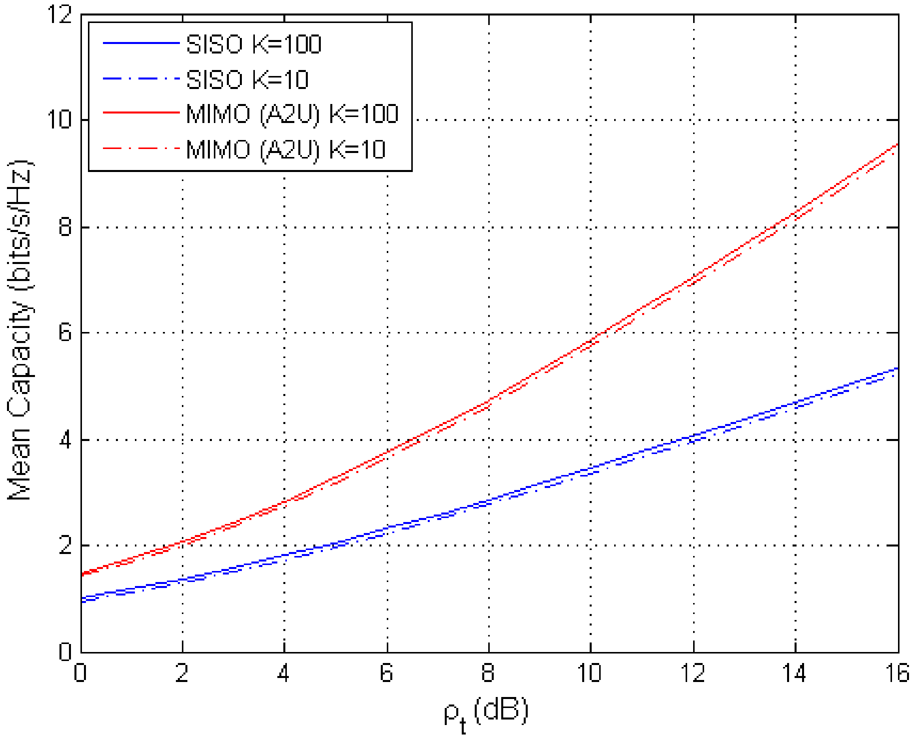


Figure 3.5: Mean capacity analysis in A2U scenario at $\mathrm{d_G} = 1.15$ m

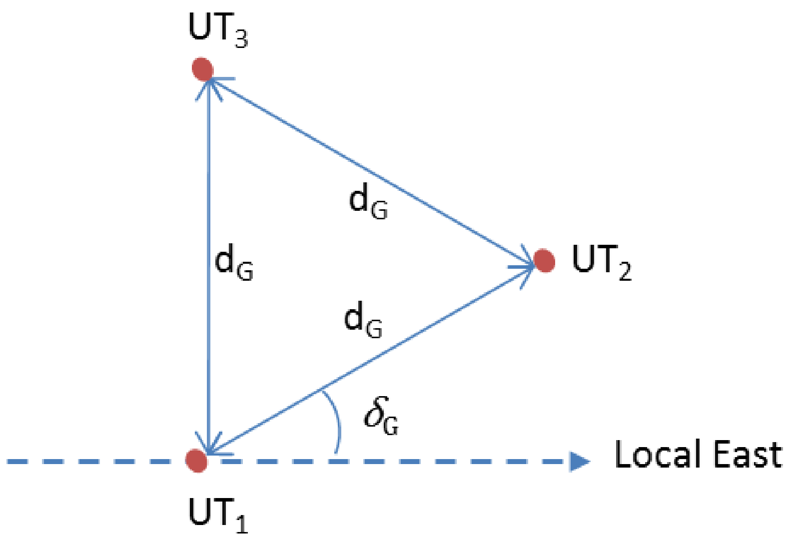


Figure 3.6: Triangular antenna arrangement for UT antennas

optimal capacity $C_{\mathrm{opt}}$. In this case, $\mathrm{d_G} = 1.4$ m is chosen as optimum from Figure 3.7 (choosing the smallest $\mathrm{d_G}$ that maximises the mean capacity). Note that forcing $\mathrm{d_G}$ to 1 m will reduce capacity by only a small amount from approximately 6.2 to 6 bits/s/Hz.

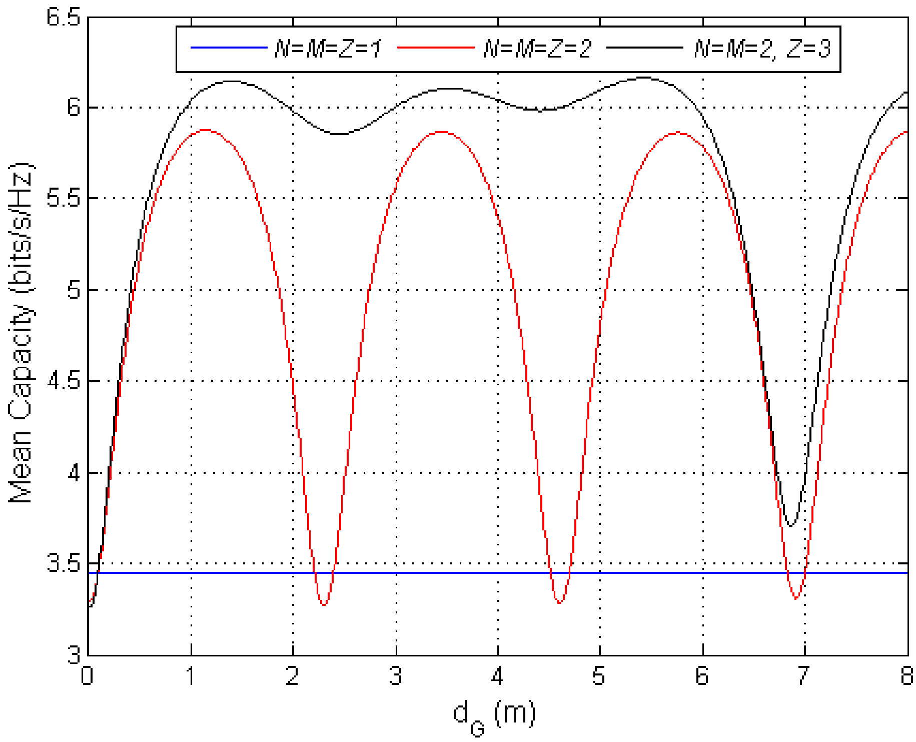


Figure 3.7: Mean capacity analysis at $K = 100$ and $\rho_u = \rho_d = 13$ dB (showing the effect of using a three antenna triangular arrangement)

## 3.4 Receiver Architecture

The receiver signal processing and architecture are of a paramount importance to realising MIMO SATCOM through multiple satellites. In this section, time domain signal processing methods are discussed to deal with different propagation time delay and Doppler offsets between the two satellite paths. The receiver signal processing architecture for the A2U and U2A scenarios are also provided.

### 3.4.1 SISO uplink and MIMO downlink

The A2U scenario comprises two SISO uplinks and a MIMO downlink. The proposed receiver architecture is shown in Figure 3.9. The signal processing approach assumes oversampling at integer multiples of the symbol rate. With reference to Figure 3.2, the

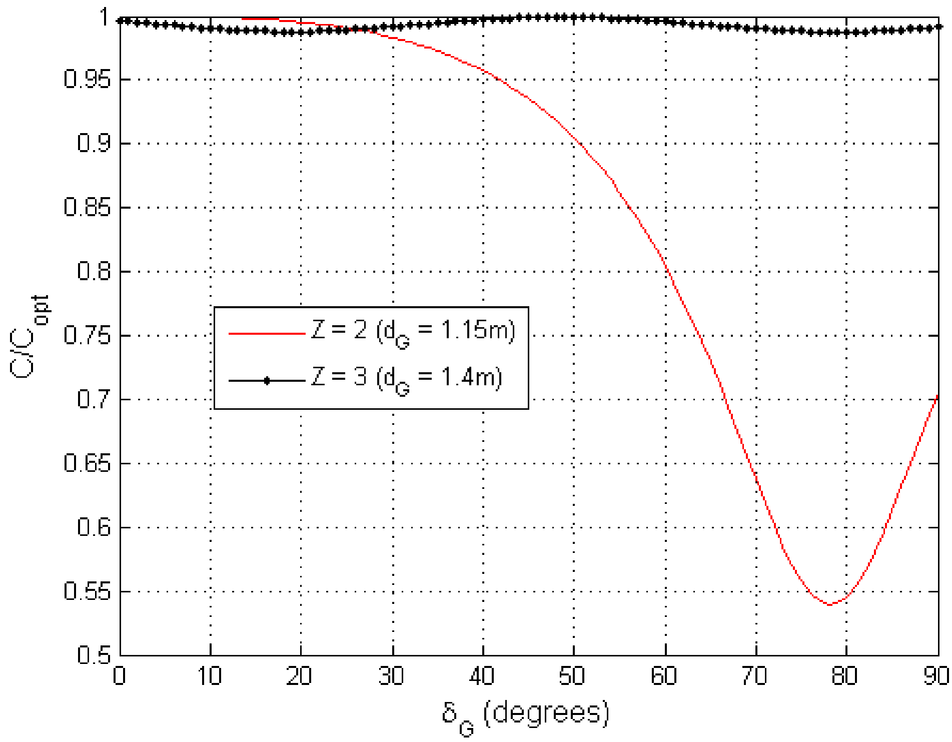


Figure 3.8: Mean capacity analysis with antenna orientation angle for two and three antenna arrangement

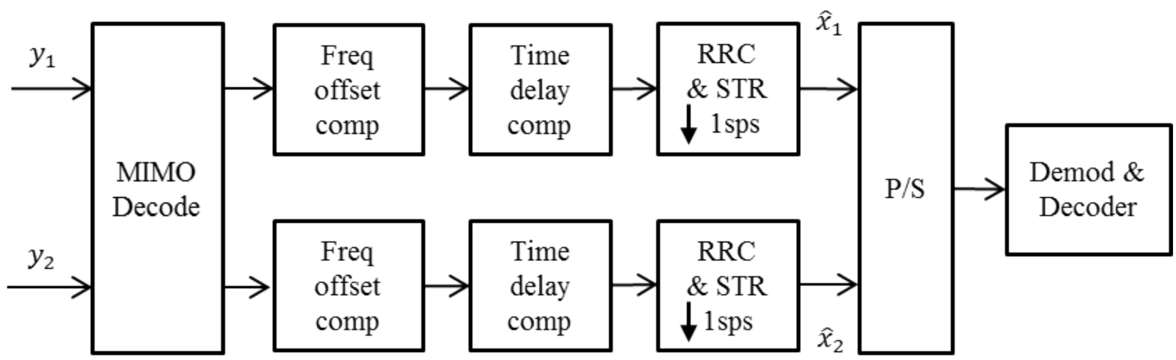


Figure 3.9: Receiver architecture for A2U scenario

formulation of the received signal is given as:

$$\mathbf{y} = \mathbf{H}_d\mathbf{H}_s\mathbf{H}_u\mathbf{x} + \mathbf{H}_d\mathbf{H}_s\mathbf{w}_u + \mathbf{w}_d, \tag{3.23}$$

where $\mathbf{x} \in \mathbb{C}^{N\times 1}$ and $\mathbf{y} \in \mathbb{C}^{Z\times 1}$ are transmit and receive vectors. To simplify the analysis, $N = M = Z = 2$ are again chosen:

$$\begin{bmatrix} y_1 \\ y_2 \end{bmatrix} = \begin{bmatrix} h_{d,11} & h_{d,12} \\ h_{d,21} & h_{d,22} \end{bmatrix} \mathbf{H}_s \begin{bmatrix} h_{u,11} & 0 \\ 0 & h_{u,22} \end{bmatrix} \begin{bmatrix} x_1 \\ x_2 \end{bmatrix} + \mathbf{H}_d \mathbf{H}_s \mathbf{w}_u + \mathbf{w}_d \tag{3.24}$$

and

$$\mathbf{H}_s = \begin{bmatrix} h_{s,1} & 0 \\ 0 & h_{s,2} \end{bmatrix}. \tag{3.25}$$

Ignoring the noise components, the time-series representation of the received signal will be

$$y_1(t) = h_{111}(t)\ x_1(t - \tau_{111}) + h_{122}(t)\ x_2(t - \tau_{122}), \tag{3.26}$$

$$y_2(t) = h_{211}(t)\ x_1(t - \tau_{211}) + h_{222}(t)\ x_2(t - \tau_{222}), \tag{3.27}$$

where $\tau_{zmn}$ denotes the overall propagation time in each channel path and where

$$h_{zmn} = h_{d,zm} h_{s,m} h_{u,mn}, \tag{3.28}$$

$$\tau_{zmn} = \frac{r_{d,zm}}{c} + \tau_{s,m} + \frac{r_{u,mn}}{c}, \tag{3.29}$$

and where $\tau_{s,m}$ denotes propagation time through each satellite signal path. $\tau_{s,m}$ will be small, and $\tau_{s,1} \approx \tau_{s,2}$ is a realistic assumption and achievable for a satellite, so we choose to simplify the analysis by using $\tau_{s,1} = \tau_{s,2} = 0$ . Again, based on the geometry and close antenna spacing at the ground for anchors and UTs, the total propagation time can be approximated as follows:

$$\tau^{\{m\}} \simeq \tau_{1m1} \simeq \tau_{2m1} \simeq \tau_{1m2} \simeq \tau_{2m2} \qquad m \in \{1, 2\}. \tag{3.30}$$

The propagation time difference between the two satellite paths is given by:

$$T_d = \max(\tau^{\{m\}}) - \min(\tau^{\{m\}}) \qquad m \in \{1, 2\}. \tag{3.31}$$

After simplifying (3.26) and (3.27) using (3.30):

$$y_1(t) = h_{111}(t)\ x_1(t - \tau^{\{1\}}) + h_{122}(t)\ x_2(t - \tau^{\{2\}}), \tag{3.32}$$

$$y_2(t) = h_{211}(t)\ x_1(t - \tau^{\{1\}}) + h_{222}(t)\ x_2(t - \tau^{\{2\}}). \tag{3.33}$$

The frequency offset (inclusive of the Doppler) associated in the channel paths through each respective satellite will be identical. That is, the channel path elements $h_{111}(t)$ and $h_{211}(t)$ will experience the same frequency offset and similarly for the channel path elements $h_{122}(t)$ and $h_{222}(t)$. This accounts for the satellite movement and assumes that the anchor terminals are not moving and the UT antennas are co-located on a single platform, hence they move together.

A suitable MIMO decoder based on either minimum mean square error (MMSE) or zero forcing (ZF) criteria can be employed for channel inversion [27]. The channel inversion processing coherently separates the two parallel symbol streams. Post channel inversion, frequency offset compensation and time delay compensation are required to compensate for individual frequency offsets and to time-align the symbol streams (due to $T_d$) respectively. Subsequently the signals are processed by Root-Raised Cosine (RRC) filtering and symbol-timing recovery (STR) as shown in Figure 3.9. Post STR, the oversampled signals are decimated to one sample per symbol (sps) rate, to obtain $\hat{x}_1$ and $\hat{x}_2$. The received symbol estimates are then combined serially followed by conventional receiver processing that includes demodulation and forward error correction (FEC) decoding.

### 3.4.2 MIMO uplink and SISO downlink

In the U2A scenario, the uplink is MIMO and two downlinks are SISO:

$$\begin{bmatrix} y_1 \\ y_2 \end{bmatrix} = \begin{bmatrix} h_{d,11} & 0 \\ 0 & h_{d,22} \end{bmatrix} \mathbf{H}_s \begin{bmatrix} h_{u,11} & h_{u,12} \\ h_{u,21} & h_{u,22} \end{bmatrix} \begin{bmatrix} x_1 \\ x_2 \end{bmatrix} + \mathbf{H}_d \mathbf{H}_s \mathbf{w}_u + \mathbf{w}_d. \tag{3.34}$$

Ignoring the noise components, the time-series representation of the received signal after substituting (3.30) will be as follows:

$$y_1(t) = h_{111}(t)\ x_1(t - \tau^{\{1\}}) + h_{112}(t)\ x_2(t - \tau^{\{1\}}), \tag{3.35}$$

$$y_2(t) = h_{221}(t)\ x_1(t - \tau^{\{2\}}) + h_{222}(t)\ x_2(t - \tau^{\{2\}}). \tag{3.36}$$

In contrast to the A2U scenario, in the U2A scenario, the frequency offset and time delay compensation must be performed before the channel inversion as shown in Figure 3.10. In equations (3.35), (3.36), the frequency offset in the channel path elements $h_{111}(t)$ and $h_{112}(t)$ will be the same and similarly for $h_{221}(t)$ and $h_{222}(t)$. To compensate for the propagation time difference, one of the received signals with $\min(\tau^{\{m\}})$ has to be delayed by $T_d$ to time align with the other received signal. The symbol estimates $\hat{x}_1$ and $\hat{x}_2$ are obtained post channel inversion, filtering and timing recovery. The subsequent receiver signal processing after the parallel to serial conversion block is identical to the U2A scenario.

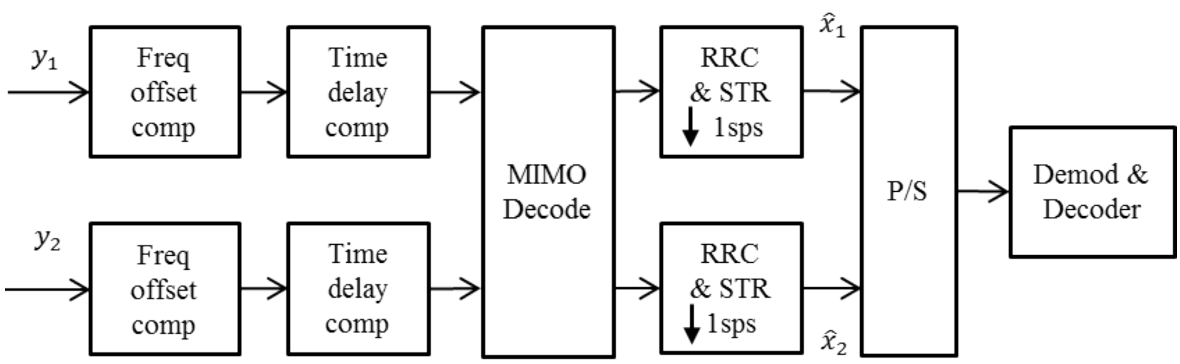


Figure 3.10: Receiver architecture for U2A scenario

### 3.4.3 MIMO uplink and MIMO downlink

In the A2U and U2A scenarios, MIMO is used either on downlink or uplink, hence, the receiver signal processing is relatively simple. If MIMO links are used in both uplink and downlink:

$$\begin{bmatrix} y_1 \\ y_2 \end{bmatrix} = \begin{bmatrix} h_{d,11} & h_{d,12} \\ h_{d,21} & h_{d,22} \end{bmatrix} \mathbf{H}_s \begin{bmatrix} h_{u,11} & h_{u,12} \\ h_{u,21} & h_{u,22} \end{bmatrix} \begin{bmatrix} x_1 \\ x_2 \end{bmatrix} + \mathbf{H}_d \mathbf{H}_s \mathbf{w}_u + \mathbf{w}_d. \tag{3.37}$$

Again, ignoring the noise components, the time-series representation of the received signal after substituting (3.30) will be as follows:

$$\begin{aligned} y_1(t) = {} & h_{111}(t)\ x_1(t - \tau^{\{1\}}) + h_{121}(t)\ x_1(t - \tau^{\{2\}}) \\ & + h_{112}(t)\ x_2(t - \tau^{\{1\}}) + h_{122}(t)\ x_2(t - \tau^{\{2\}}), \end{aligned} \tag{3.38}$$

$$\begin{aligned} y_2(t) = {} & h_{211}(t)\ x_1(t - \tau^{\{1\}}) + h_{221}(t)\ x_1(t - \tau^{\{2\}}) \\ & + h_{212}(t)\ x_2(t - \tau^{\{1\}}) + h_{222}(t)\ x_2(t - \tau^{\{2\}}). \end{aligned} \tag{3.39}$$

Each of the received signals have multiple copies of the transmitted symbols, time separated by $T_d$. This results in a multipath induced frequency selective channel with a coherence bandwidth inversely proportional to $T_d$. The typical coherence bandwidth will be in the order of 1 kHz or less due to large orbital separation of the satellites. With such a small coherence bandwidth, an efficient waveform design would be challenging. This architecture is not considered further in this thesis.

## 3.5 Simulation Results

A simulation framework was developed to evaluate the performance of the A2U scenario with a slow varying flat fading Ricean channel. The bit error rate (BER) performance was assessed for the MIMO system in comparison with conventional SISO SATCOM under different Ricean factor values ($K$ =100 and $K$ =10). In Figure 3.11, uncoded 16-QAM and uncoded QPSK are considered to achieve a spectral efficiency of 4 bits/s/Hz in the SISO (single satellite, 16-QAM) and MIMO (two satellites, 2 $\times$ QPSK), respectively. The term $\mathrm{E_s/N_o}$ is identical to $\rho_t$, assuming the signal bandwidth is same as the symbol rate. The figure legend $Z \times M \times N$ signifies the number of receivers, satellites and transmitters, respectively. The UHF UTs are spaced at an optimum distance $\mathrm{d_G} = 1.15$ m as per Figure 3.3. Throughout, the simulation framework uses a fixed frequency offset of 1000 Hz and 1050 Hz at the two satellites, respectively, $T_d = 1.02 \times 10^{-3}$ sec, a sample rate of 25 kHz and four samples per symbol oversampling. It is assumed that the receiver has a perfect knowledge of the channel, frequency offsets and propagation time difference.

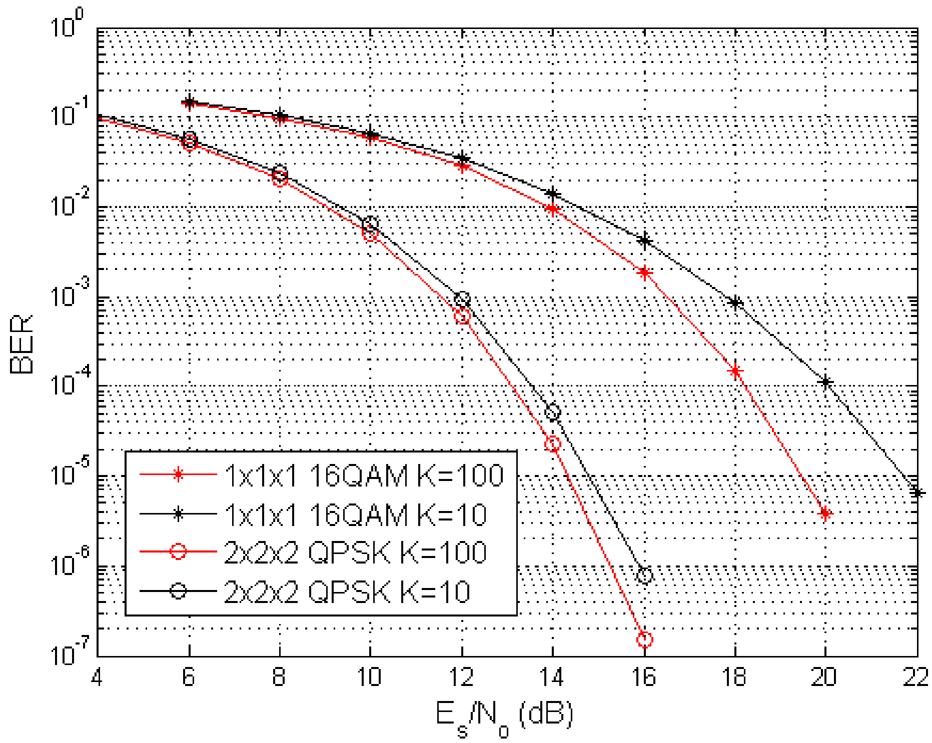


Figure 3.11: Uncoded BER performance in Ricean fading at $\mathrm{d_G} = 1.15$ m

The performance improvement using MIMO is illustrated in Figure 3.11. Approximately 5 dB and 6.5 dB of improvement is achieved over the SISO scenario at $10^{-5}$ BER for $K = 100$ and $K = 10$, respectively. For a fair comparison, the sum power in the uplink ($\mathrm{EIRP}_u$) and downlink ($\mathrm{EIRP}_d$) are the same in both MIMO and SISO cases.

In Figure 3.12, the BER performance is analysed with respect to different inter-antenna spacing at $E_s/N_o = 14$ dB. The lowest BER is achieved when $\mathrm{d_G} = 1.15$ m, where the channel is spatially orthogonal in the A2U scenario. This pattern is related to the capacity analysis presented in Figure 3.3.

The BER performance using a popular error control coding method, namely low density parity check (LDPC) at half rate code is shown in Figure 3.13. The LDPC code design is based on DVB-S2 standard with block length equal to 64,800 bits [47]. Similarly, the results show a performance improvement of 4.5 dB and 6.7 dB over SISO scenario at $10^{-4}$ BER for $K = 100$ and $K = 10$, respectively.

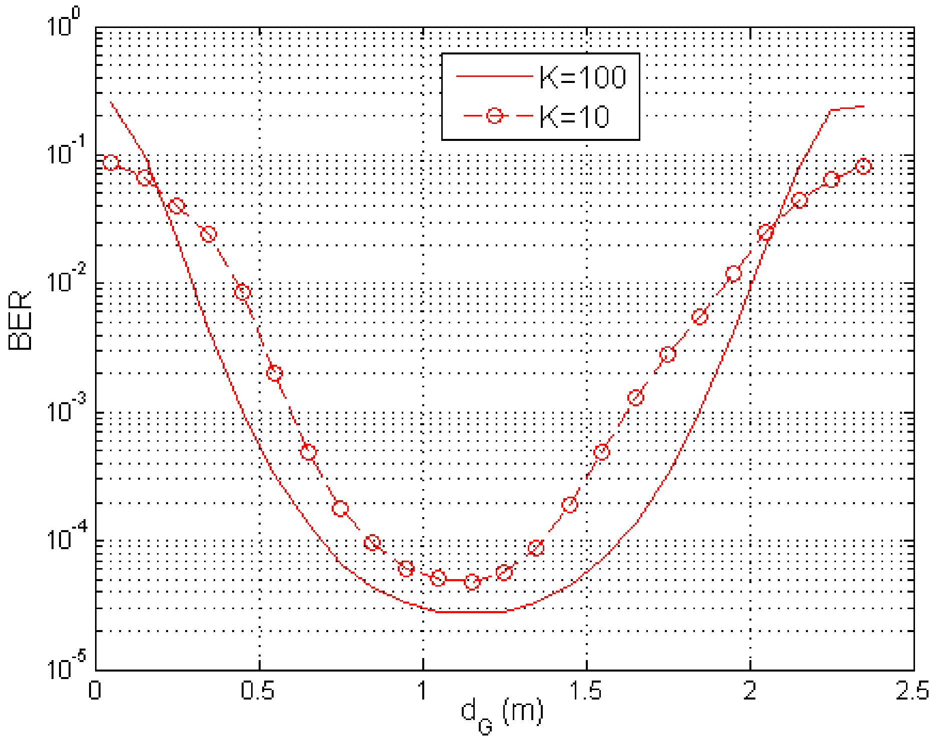


Figure 3.12: A2U 2×2×2 uncoded QPSK, BER with respect to $\mathrm{d_G}$ at $E_s/N_o = 14$ dB

## 3.6 Satellite Orbital Drift

So far, it has been assumed that the satellites are fixed in their respective orbital positions except for the acknowledgement of a Doppler contribution. However, in practice the satellites do not maintain a stationary position and have non-zero eccentricity and

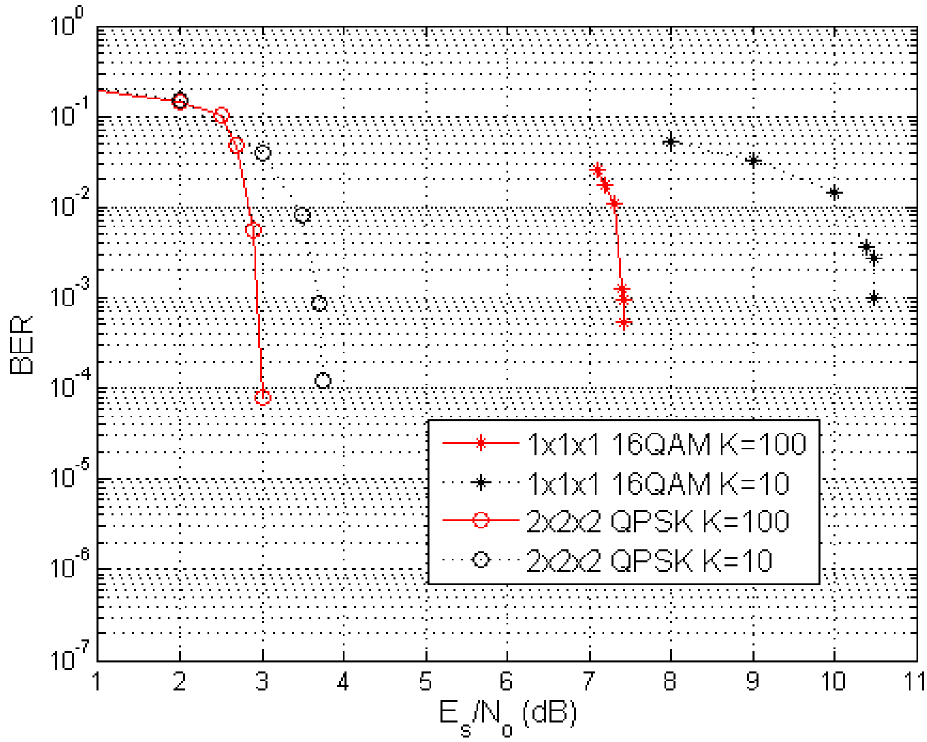


Figure 3.13: Comparison of 16-QAM SISO + A2U 2x QPSK MIMO, LDPC Rate 1/2 BER performance in Ricean fading channel

inclination. As the orthogonality of the channel is dependent on the geometry, it is important to consider the restrictions of the MIMO channel capacity to the real world effects of satellite movements. A typical station keeping volume for a geostationary satellite in latitude and longitude is $\pm 0.05^{\circ}$ and $4e^{-4}$ in eccentricity [46]. Assuming the two satellites are in random locations within their respective station keeping box, for each set of satellite positions, the optimal location contours for antenna placement is overlaid and is shown in Figure 3.14. Each contour in Figure 3.14 corresponds to different $\nu$ value that satisfies (3.22) in the A2U scenario.

The contour lines, whilst not significantly smeared in this case, indicates that the antenna placement for UHF SATCOM is least affected due to the satellite ephemeris. This result is attributed to the farther orbital separation of satellites for the UHF band, which would not be the case in the higher frequency bands that utilise closer orbital separation of satellites. Some satellites in the UHF band are deliberately placed in an inclined orbit to serve the polar regions. The optimal location contour is shown in

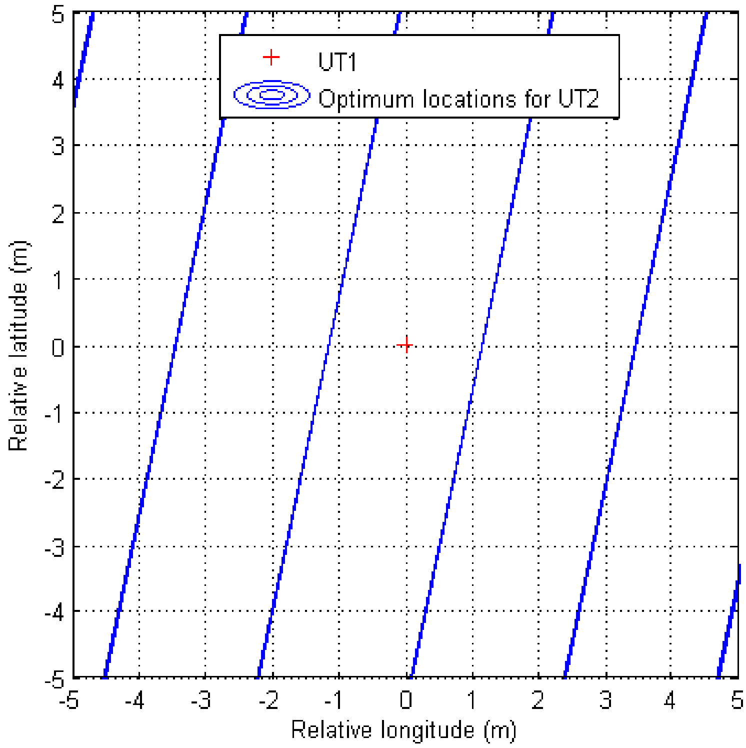


Figure 3.14: Optimal location contour for antenna placement

Figure 3.15 when the satellites are inclined by plus or minus two degrees in latitude. The smearing effects in the location contours are much more pronounced and are due to the large relative movement of the satellites. At the same time, the optimal location contours also indicate that there is only a small degradation when the UTs are arranged in the longitudinal axis, that is, $\delta_{\mathrm{G}} = 0$.

Figure 3.16 shows the normalised capacity analysis with respect to the antenna orientation angle for the case when the satellites are two degrees inclined. As it can be seen from the figure, for $Z = 2$ antennas on the ground, the capacity randomly varies with respect to $\delta_G$ for each random position of the satellites. This phenomenon is comparable with the optimal location contour plot in Figure 3.15. However, for $Z = 3$ antennas on the ground in a triangular set-up as shown in Figure 3.6, the normalised capacity is less sensitive to both the $\delta_G$ and the satellite inclination. The results show that for a practical use case, a triangular antenna set-up can offer a robust geometrical solution in the UHF band when using MIMO SATCOM even with inclined satellites.

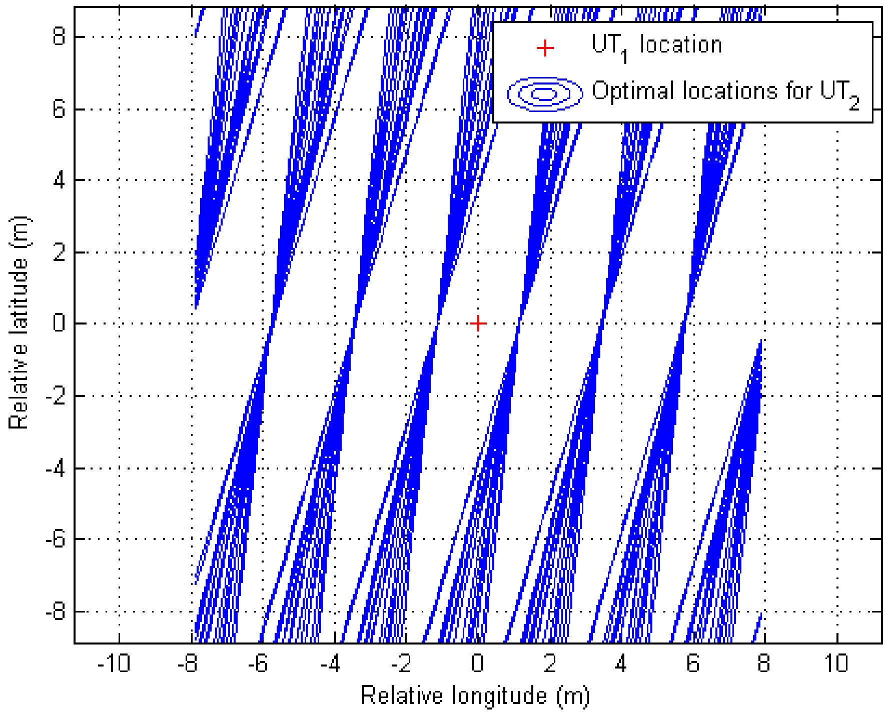


Figure 3.15: Optimal location contour for UT antenna placement for 2° inclined satellites for $Z = 2$

## 3.7 Chapter Review

Narrowband satellite communications at UHF is an attractive option to global military SATCOM community because of its unique advantages, including low cost. However, an inherent drawback of the UHF band is its relatively low bandwidth and the practical inability to frequency reuse in the geo-stationary orbital space due to the broad beamwidth of user antennas; hence very limited available capacity. In this chapter, the potential performance improvement for UHF SATCOM by applying the MIMO spatial multiplexing technique is analysed. Spatial orthogonality was achieved through two satellites separated by 30 degrees in orbit and UHF user antennas separated by spacing in the order of one meter on the ground as a specific example. Channel modelling using Ricean flat fading channel and capacity calculations were presented. A simple, practical receiver signal processing architecture was presented to deal with the synchronisation challenges from multiple satellites for both the A2U and U2A scenarios. The results show that the application of the MIMO technique has the potential

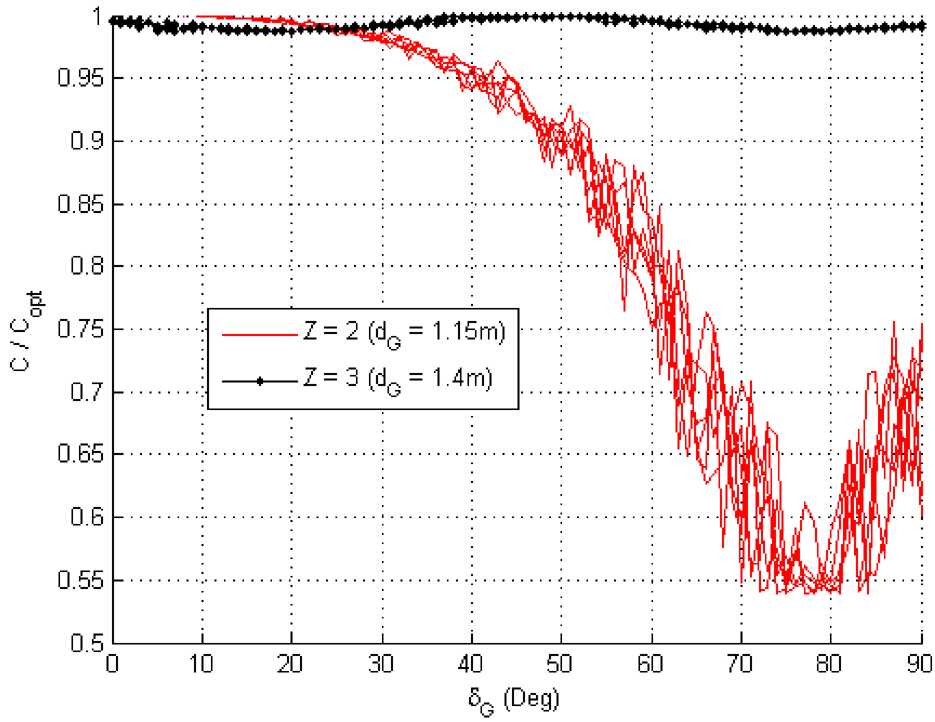


Figure 3.16: Capacity analysis with respect to $\delta_G$ for 2° inclined satellites and $Z = 2, 3$ with optimal spacing

to increase the channel capacity in narrowband UHF SATCOM. Although the MIMO analysis presented in this chapter was targeted for conventional narrowband UHF SATCOM, the technique may also provide a MIMO opportunity for satellites such as the US DoD's mobile user objective system (MUOS). Investigation of MIMO waveforms for frequency selective multi-user wideband UHF SATCOM channels is a subject topic for future research and is further discussed in Section-7.2.1. Results form the work presented in this chapter have been published in [8] and [9].

# Chapter 4

# Polarization Multiplexing

Utilising orthogonal polarizations as two independent SISO systems is an existing frequency reuse technique in SATCOM. Polarization multiplexing is similar to spatial multiplexing but without the requirement to spatially separate antennas either in the ground or space. A single Dual Polarized (DP) antenna that can simultaneously excite in both orthogonal polarizations can be used to transmit or receive an independent data stream in each polarization. However, poor Cross Polar Isolation (XPI) in the link can significantly reduce the achievable gain.

The application of polarization for MIMO SATCOM has been studied earlier for LMS broadcasting systems [48, 23]. The conclusion of these studies was that the polarization provides significant diversity gain in an LMS channel. In [49], one-dimensional Space Time Trellis Codes (STTCs) are shown to provide both multiplexing and diversity gains in a DP channel. In a Rayleigh fading channel, the use of STTC with polarization multiplexing is shown to provide equal or better BER than the SISO scenario whilst doubling the spectral efficiency [20].

In this chapter, the polarization domain is analysed under LOS channel conditions using two orthogonal circular polarizations, namely Left Hand Circular Polarization (LHCP) and Right Hand Circular Polarization (RHCP). Under LOS conditions (assuming without rain) there is significant natural isolation in the channel between the two polarizations. Thus, the channel induced depolarization is minimal and the XPI in the link would be dominated by each antenna's ability to distinguish between the polarizations [50].

We begin with a brief introduction to polarization in Section-4.1 and show how the system performance can degrade when using orthogonal polarizations as two separate SISO channels. It is common in MIMO literature to define the polarization metrics using the antenna's Axial Ratio (AR), it's Cross-Polar Discrimination (XPD) or in-terms of the XPI in the link. However, these metrics only represent the polarization state in-terms of amplitude or power values and ignore the phase information. We derive a DP antenna model for circular polarization in Section-4.3 that includes both phase and amplitude, and show that in a MIMO context the factor "polarization parallelity" of an antenna is more significant than XPD. Using the DP antenna model, an example case study is presented in Section-4.4 in order to analyse the requirements for combined spatial and polarization MIMO with a $4 \times 4$ channel model. Using the case study, the MIMO capacity impact due to non-ideal DP antennas is analysed in Section 4.5.

## 4.1 Polarization Ellipse

The Electro-Magnetic (EM) wave radiated by an antenna consists of an electric field component and a magnetic field component; these two components are orthogonal and are perpendicular to the direction of propagation of the wave [46]. Polarization is defined as the orientation of the plane that contains the electric field of the radiated wave [51]. A vertical whip antenna generates and receives in vertical polarization. Similarly if the antenna element is horizontal, the wave polarization is horizontal. Vertical and horizontal polarizations are categorised as linear polarizations and are mutually orthogonal. Elliptical polarization is similar to linear polarization but uses both vertical and horizontal elements of the antenna to create a polarization vector that rotates either in left-hand or right-hand polarization. Circular polarization is a special case of elliptical polarization and is commonly used in MILSATCOM as LHCP and RHCP, because in an ideal case, it removes the need to align the transmit and receive antennas. LHCP and RHCP are mutually orthogonal to each other. Linear or circular orthogonal polarizations both support frequency reuse technique in SATCOM.

The antenna polarization can be conveniently explained using a polarization ellipse as shown in Figure 4.1. The time harmonic electric field vector, denoted by **E** for a plane wave along the direction of propagation in the **z** axis, is a function of time ($t$) and position ($\mathcal{Z}$) along the direction of propagation. In the figure, the **z** axis cuts through and propagates out of the page.

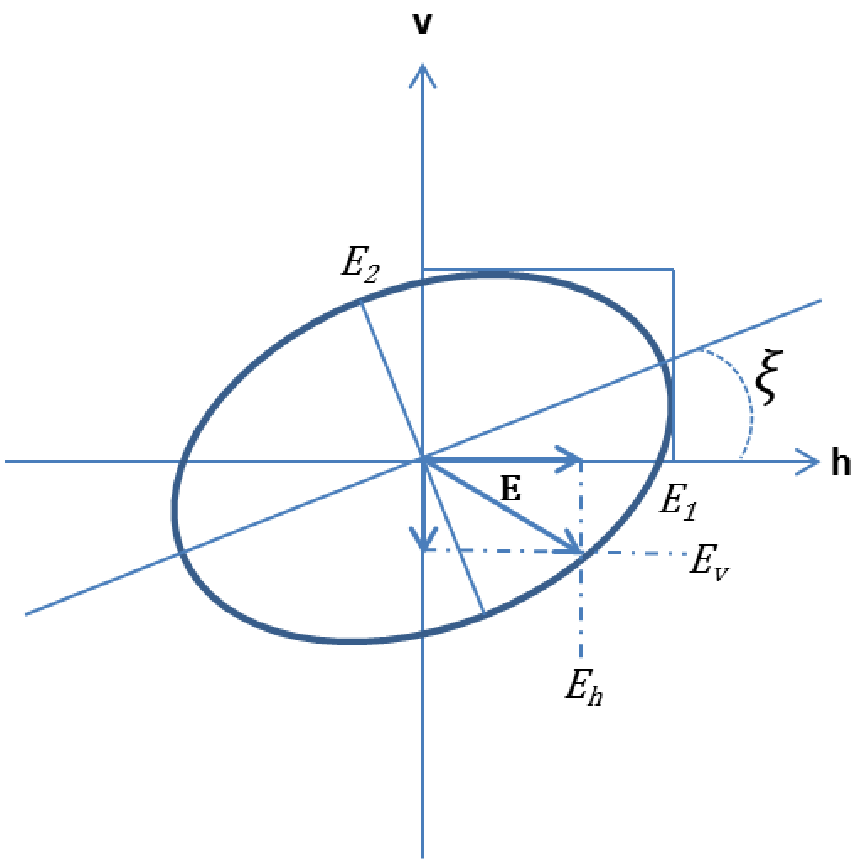


Figure 4.1: Polarization ellipse

$$\mathbf{E} = \mathbf{h}E_h + \mathbf{v}E_v, \tag{4.1}$$

where **h** and **v** are the components of the **E** field vector. The terms $E_h$ and $E_v$ denote the instantaneous amplitudes of the **h** and **v** components, respectively:

$$E_h = E_1 \sin(\omega t - \beta \mathcal{Z}), \tag{4.2}$$

$$E_v = E_2 \sin(\omega t - \beta \mathcal{Z} + \delta_{\mathrm{P}}), \tag{4.3}$$

where $E_1$ and $E_2$ are peak amplitudes along the $\mathbf{h}$ and $\mathbf{v}$ directions, respectively, and $\beta$ denotes the wave number. The term $\delta_{\mathrm{P}}$ denotes the relative phase between the $E_h$ and $E_v$ components of the electric field vector.

For a linear polarized wave, $\delta_{\mathrm{P}}$ will be equal to zero and the orientation of the electric field is determined by $\mathbf{h}E_1 + \mathbf{v}E_2$. If $E_1 = E_2$ and $\delta_{\mathrm{P}} = \pm 90$ degrees, the wave will be circularly polarized. According to the IEEE notation, a right hand circular polarization (where $\delta_{\mathrm{P}} = -90^{\mathrm{o}}$) is clockwise rotation of the wave viewed in the direction of propagation. Similarly, a left hand circular polarization (where $\delta_{\mathrm{P}} = +90^{\mathrm{o}}$) is characterised by anti-clockwise rotation of the wave viewed in the direction of propagation [51].

The AR of an antenna is defined as voltage ratio of the major and minor axis of the polarization ellipse, ($1 \leq \mathrm{AR} \leq \infty$). The AR is equal to one for ideal circular polarization. The tilt angle $\xi$ in the polarization ellipse is defined as the angle between the major axis and the $\mathbf{h}$ axis.

## 4.2 Polarization Metrics

Although there exist multiple version of definitions for XPD and XPI in the literature, in this thesis we follow the following definitions: XPD is an antenna specific parameter and is a measure of how much a signal in a given polarization is coupled into the opposite polarization. XPI is a measure of how much two signals transmitted simultaneously in orthogonal polarizations will interfere with each other at the receiver [23, 46]. XPI is denoted as a power ratio between the Cross-Polar (XP) and Co-Polar (CP) components in the link at the receiver.

To maximise CP signal reception; the axial ratio, polarization sense (RHCP or LHCP) and orientation (tilt angle) of the receive antenna must match with the polarization of a received wave. Similarly to maximise XPI in the link, the antenna AR and orientation must match the received CP signal, but in an opposite sense (for example, the receive antenna polarization fully rejecting the XP signal).

The XPD of an antenna is often expressed in-terms of the antenna AR as given below [46]:

$$\mathrm{XPD} = \frac{\mathrm{AR}+1}{\mathrm{AR}-1} \tag{4.4}$$

Since XPD and AR are amplitude ratios, in decibels they are expressed by $20\log_{10}(\mathrm{XPD})$ and $20\log_{10}(\mathrm{AR})$, respectively. Similarly, XPI can be expressed in-terms of the AR and polarization tilt angles between the incoming wave and the received antenna [51].

$$\mathrm{XPI} = 1 - \frac{(1+\mathrm{AR}_t^2)(1+\mathrm{AR}_r^2) + 4\mathrm{AR}_t\mathrm{AR}_r + (1-\mathrm{AR}_t^2)(1-\mathrm{AR}_r^2)\cos(2[\xi_t - \xi_r])}{2(1+\mathrm{AR}_t^2)(1+\mathrm{AR}_r^2)} \tag{4.5}$$

where the subscripts $t$ and $r$ denote transmit and receive antennas, respectively, and $\xi_t - \xi_r$ denotes the polarization tilt angle difference between these antennas. In this case, we have assumed an ideal channel with no depolarization. In decibels the XPI is given as $10\log_{10}(\mathrm{XPI})$. In Figure 4.2, an example where the transmit antenna AR is held constant 1.5 dB, the XPI is plotted against the polarization tilt angle difference for different polarization axial ratios. Often for circularly polarized antennas, the polarization performance will be given in-terms of AR or XPD. It can be noticed from Figure 4.2 that a given antenna AR does not guarantee a specific XPI in the link at the receiver, rather XPI is dependent on both AR and polarization tilt angles. Good isolation between the polarization is achieved when there is match between the AR of the transmit and receive antennas and the tilt angle difference is zero [52].

### 4.2.1 XPI Impact

While simultaneously using both circular polarizations can ideally double the channel capacity, poor XPI in the link can significantly degrade the system performance. In this sub-section, the XPI impact on the received SNR at the output of the antenna is

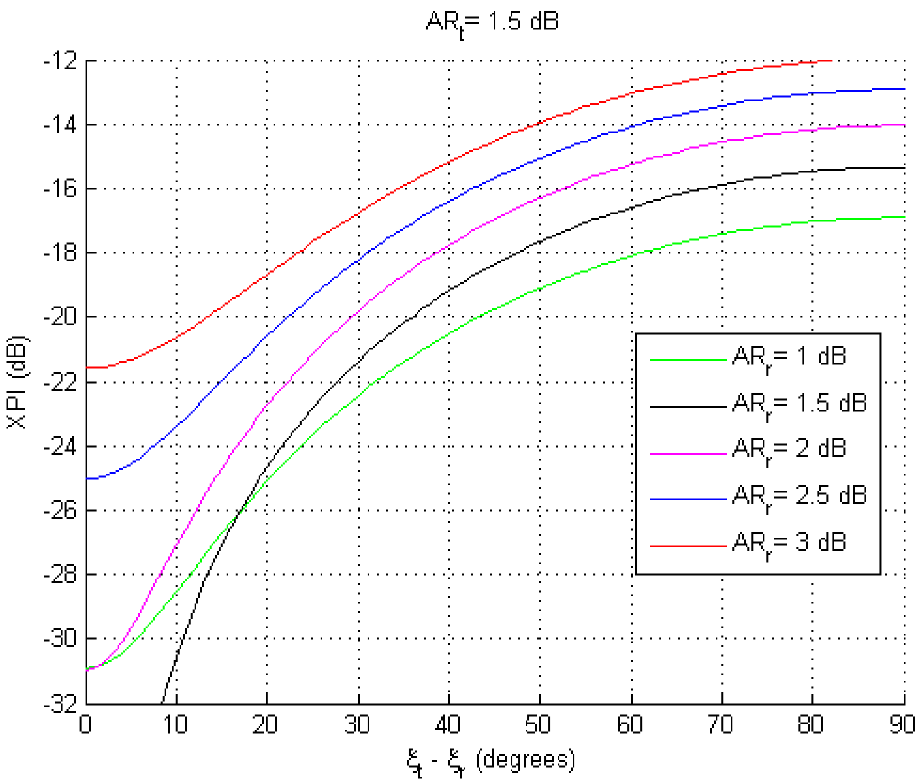


Figure 4.2: Polarization tilt angle impact on XPI

assessed. The expected received SNR ($\rho$) of a typical link is given by:

$$\rho = \frac{S_{\text{cp}}}{\sigma_w^2}, \tag{4.6}$$

where $S_{\text{cp}}$ is the received signal power for the CP signal and $\sigma_w^2$ denotes the receiver noise power. If both circular polarizations are used simultaneously, the presence of an another independent signal on the XP port could add as interference to the CP signal. Thus the actual received Signal to Noise plus Interference Ratio (SNIR) $\varrho$ is given by:

$$\varrho = \frac{S_{\text{cp}}}{\sigma_w^2 + S_{\text{xp}}}, \tag{4.7}$$

where $S_{\text{xp}}$ is the received power of the opposite polarization signal at the CP port. According to the XPI definition, we have:

$$\text{XPI} = \frac{S_{\text{xp}}}{S_{\text{cp}}}. \tag{4.8}$$

Thus the received SNIR can be expressed in a simplified form:

$$\varrho = \frac{\rho}{1 + \mathrm{XPI}\ \rho}. \tag{4.9}$$

In Figure 4.3, the XPI impact in the received SNIR is compared for different XPI values. The horizontal and vertical axes represents $\rho$ and $\varrho$, respectively. It can be seen from the plots that due to poor XPI in the link, the received SNIR asymptotes to a value where no further improvements can be made. For a link with -10 dB XPI, the received SNIR value cannot exceed 10dB irrespective of the SNR in this case. The XPI impact factor is the ratio between the expected SNR and the received SNIR.

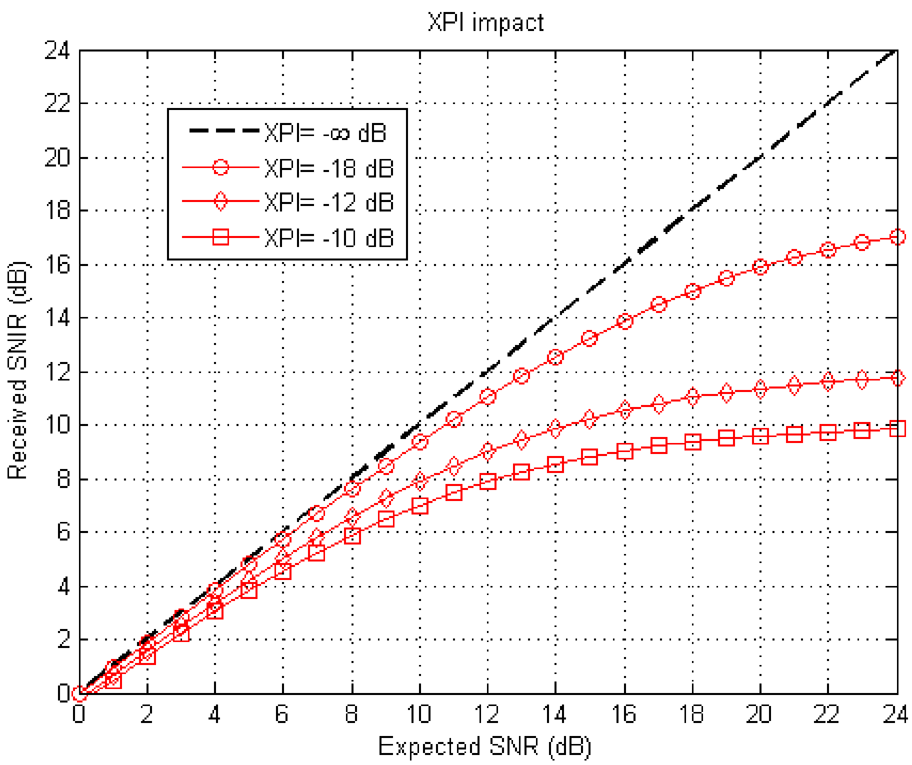


Figure 4.3: XPI impact on received SNIR

This phenomena can be compared with the BER results in [52]. It is shown that for an XPI value of -18dB, the BER performance increasingly degrades with increasing signal spectral efficiency. For example, at 1e-10 BER: using 8PSK with turbo code (rate 1/2) the XPI impact is 0.77dB, using 16APSK with turbo code (rate 3/4) the XPI impact is 2.9dB and using 16APSK with turbo code (rate 0.95) the XPI impact is 5.9dB. The data show that the XPI impact is larger as the required SNR increases due to the use of higher spectral efficiency modulation plus coding. The results show that a poor XPI in the link can significantly degrade the system performance when simultaneously using both polarizations as two independent SISO channels.

## 4.3 Antenna Polarization Model

In this section we construct an antenna polarization model to analyse the XPI impact within a MIMO context. Most communications antennas radiate linear polarization, except for a few such as helical antennas with inherent circular polarization. To generate circular polarization using linear excitation methods, two radiating elements placed perpendicular to each other in the horizontal $\mathbf{h}$ and vertical $\mathbf{v}$ axes are used, with a quarter wavelength excitation delay between them [53].

To generate LHCP, the signal to the vertical element is delayed by $\frac{\pi}{2}$ or a quarter wavelength relative to the horizontal antenna element. Similarly, to generate RHCP the signal to the horizontal antenna element is delayed by $\frac{\pi}{2}$ or a quarter wavelength relative to the vertical antenna element [54]. Thus for circular DP antennas, the antenna polarization matrix $\mathbf{P}$ is represented by two unit norm polarization column vectors $\mathbf{p}_{\mathrm{L}}$ and $\mathbf{p}_{\mathrm{R}}$ representing LHCP and RHCP, respectively. In the ideal case,

$$\mathbf{P}_{\mathrm{ideal}} = [\mathbf{p}_{\mathrm{L,ideal}}\ \mathbf{p}_{\mathrm{R,ideal}}] = \frac{1}{\sqrt{2}} \begin{bmatrix} 1 & e^{-j\frac{\pi}{2}} \\ e^{-j\frac{\pi}{2}} & 1 \end{bmatrix}. \tag{4.10}$$

By simultaneously exciting a transmitting antenna in both LHCP and RHCP, the resulting $E_h$ and $E_v$ axes can be expressed as:

$$\begin{bmatrix} E_h \\ E_v \end{bmatrix} = \mathbf{P} \begin{bmatrix} x_1 \\ x_2 \end{bmatrix}, \tag{4.11}$$

where $x_1$ and $x_2$ are the signals at the LHCP and RHCP input ports of the antenna, respectively.. However, in practice the generated polarization will be elliptical due to antenna excitation errors in amplitude and phase. The signal flow for LHCP and RHCP is shown in Figure 4.4. The non-ideal circular polarization amplitude excitation scaling factors are denoted by $A_1$ and $A_2$ and angular deviation from ideal phase excitations are denoted by $\varphi_1$ and $\varphi_2$.

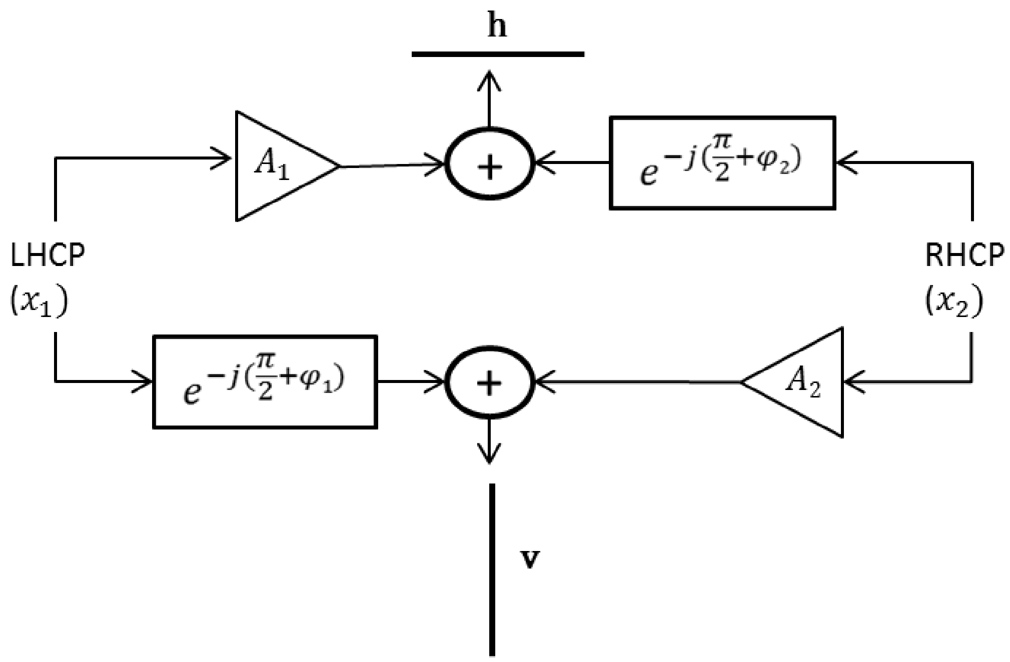


Figure 4.4: Signal flow for LHCP and RHCP

The antenna polarization model with all mismatch factors is represented in a matrix form in (4.12). This representation is similar to the amplitude and phase excitation errors in [55], but here it is presented in a convenient matrix form:

$$\mathbf{P} = [\mathbf{p}_{\text{L}}\ \mathbf{p}_{\text{R}}] = \begin{bmatrix} A_1 & e^{-j(\frac{\pi}{2}+\varphi_2)} \\ e^{-j(\frac{\pi}{2}+\varphi_1)} & A_2 \end{bmatrix} \begin{bmatrix} \frac{1}{\sqrt{1+A_1^2}} & 0 \\ 0 & \frac{1}{\sqrt{1+A_2^2}} \end{bmatrix}. \tag{4.12}$$

The first 2×2 matrix denotes circular polarization excitation errors in phase ($\varphi_1$ and $\varphi_2$) and amplitude ($A_1$ and $A_2$). In the ideal case, $\varphi_1 = \varphi_2 = 0$ and $A_1 = A_2 = 1$ and (4.12) reduces to (4.10). The last 2×2 matrix is a scaling matrix that is required to ensure the two polarization column vectors $\mathbf{p}_{\text{L}}$ and $\mathbf{p}_{\text{R}}$ are unit norm.

The two polarizations are orthogonal if their inner product is zero, i.e., $\mathbf{p}_{\text{L}}$ is orthogonal to $\mathbf{p}_{\text{R}}$ iff $\mathbf{p}_{\text{L}}^{\dagger}\mathbf{p}_{\text{R}} = 0$ [6]. For DP antennas, the measure of polarization orthogonality

$p$ is a vital parameter also referred as polarization parallelity in [56].

$$p = \frac{|\mathbf{p}_{\mathrm{L}}^{\dagger}\mathbf{p}_{\mathrm{R}}|}{\|\mathbf{p}_{\mathrm{L}}\|\|\mathbf{p}_{\mathrm{R}}\|} \qquad (0 \leq p \leq 1). \tag{4.13}$$

where the orthogonality between the two polarizations diminishes from $p = 0$ (fully orthogonal) to $p = 1$ (in-phase).

A DP antenna with non-zero orthogonality will experience effective power loss due to mutual coupling between the polarizations. This power loss is analogous to the mutual coupling effect from close inter-element spacing in antenna arrays [57]. Due to a common phase centre between the two polarizations, a DP antenna cannot offer array gain and the polarization matrix has to be scaled in the following way [56]:

$$\widehat{\mathbf{P}} = \frac{\mathbf{P}}{\sqrt{1+p}}. \tag{4.14}$$

This is equivalent to scaling the polarization matrix by its maximum singular value. In a clear sky LOS condition, the channel depolarization can be negligible, hence the polarization state of the overall link is dominated by the antennas. Overall unity gain polarization matrix $\mathit{\Delta}$, which includes the effect of both transmit and receive antenna polarization matrices:

$$\mathit{\Delta} = \widehat{\mathbf{P}}_{\mathrm{r}}^{\dagger}\widehat{\mathbf{P}}_{\mathrm{t}} = \begin{bmatrix} \vartheta_{LL} & \vartheta_{LR} \\ \vartheta_{RL} & \vartheta_{RR} \end{bmatrix}, \tag{4.15}$$

where $\vartheta_{LL}$ and $\vartheta_{RR}$ denote CP elements and $\vartheta_{LR}$ and $\vartheta_{RL}$ denote XP elements. Using (2.13), the MIMO capacity of the polarization channel can be calculated as below:

$$C = \log_2 \det\left(\mathbf{I}_2 + \frac{S}{2\,\sigma_w^2}\mathit{\Delta}\mathit{\Delta}^{\dagger}\right) \qquad \text{bits/s/Hz}, \tag{4.16}$$

where $M$ and $N$ are two for orthogonal polarizations, $S$ denotes the total transmit power.

Based on the XPI definition given in Section 4.2, the XPI for the respective polarization can also be calculated using the:

$$\mathrm{XPI}_{\mathrm{L}} = \frac{|\vartheta_{LR}|^2}{|\vartheta_{LL}|^2} \tag{4.17}$$

$$\mathrm{XPI}_{\mathrm{R}} = \frac{|\vartheta_{RL}|^2}{|\vartheta_{RR}|^2} \tag{4.18}$$

where the subscripts $_{\mathrm{L}}$ and $_{\mathrm{R}}$ denote the polarization LHCP and RHCP, respectively.

The XPI and the achievable capacity are shown in Figure 4.5. For each $p$ value, the x-axis represents each discrete simulation events. In each event, random values for $A_1, A_2, \varphi_1$ and $\varphi_2$ are chosen that satisfy the required $p$ value, using a random uniform distribution in amplitude $U(\frac{1}{1.3}, 1.3)$ and phase $U(-10^o, +10^o)$.

A common requirement for SATCOM antennas is to have AR $<$ 3 dB and generally most circularly polarized antennas achieve this. Hence the distribution range $U(\frac{1}{1.3}, 1.3)$ in amplitude and $U(-10^o, +10^o)$ in phase is used for the simulation. The worst case would be $A = 1.3$ and $\varphi = 10^o$ and that will produce a polarization ellipse with AR=2.75 dB. Within this range, multiple[1] random combination of values are generated and from that a particular set of values for $A_1, A_2, \varphi_1$ and $\varphi_2$ is selected that closely match with the required $p$ value, usually within an error value of $10^{-4}$.

Note that separate amplitude and phase values are chosen for both transmit and receive antennas in each event, however, the $p$ value for both antennas are the same. The tilt angle and the AR of the transmit and receive antenna is dependent on a chosen amplitude and phase value. Since XPI is a function of the tilt angle and AR of both the transmit and receive antennas, the XPI values have random characteristics for randomly chosen amplitude and phase values, as shown in the top sub-plot of Figure 4.5. However, the MIMO capacity of the polarization model using (4.16) in the bottom sub-plot of Figure 4.5 (at 10 dB SNR) shows negligible variation under each $p$ values, irrespective of the AR, tilt angle and the resultant XPI. Hence, in a MIMO context specifying the polarization parallelity ($p$) of a DP antenna is more significant than XPD or XPI to guarantee an achievable channel capacity in the link.

[1] around 10,000

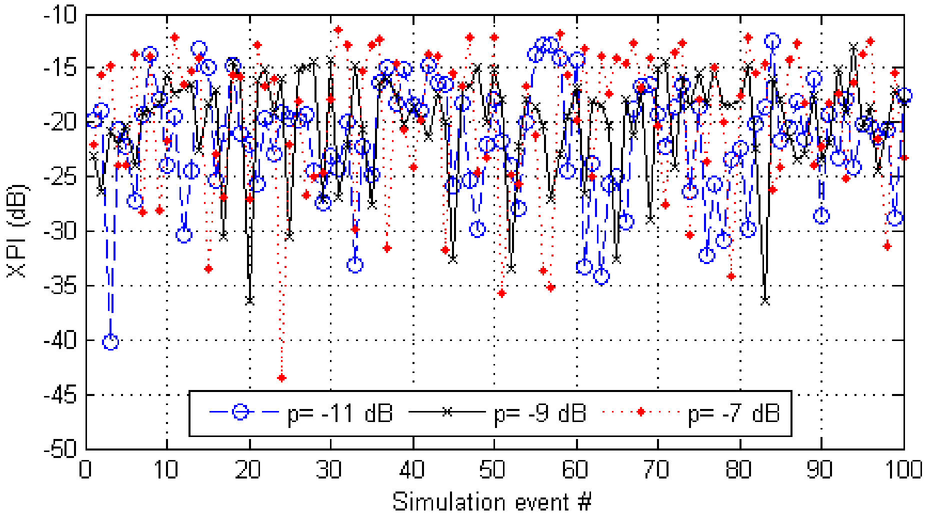


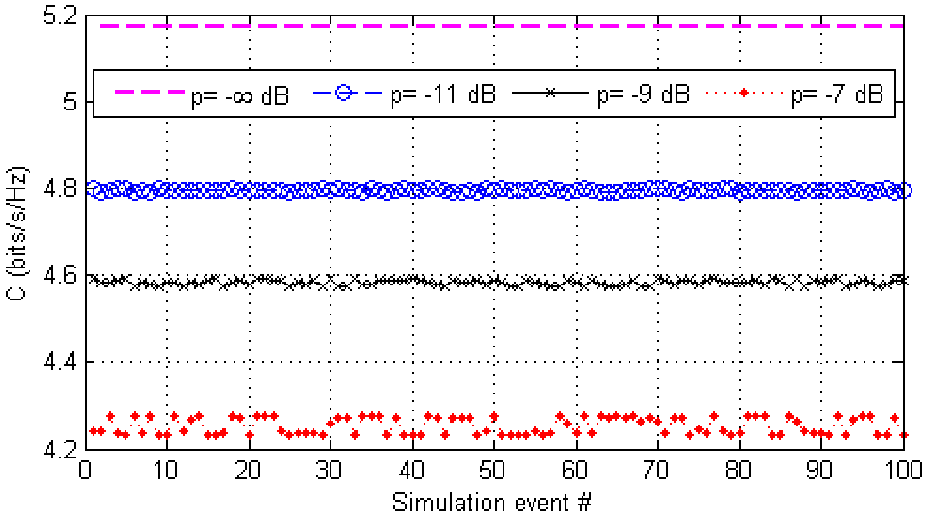


Figure 4.5: In a MIMO context, comparison of the XPI in the link (top) and the channel capacity (bottom) variation across the simulation events at 10 dB SNR

In the dual SISO context, poor XPI can degrade system performance when the two orthogonal polarizations are used simultaneously. However, the MIMO capacity results show that in a MIMO system the achievable gain is relatively insensitive to the XPI values. Hence, MIMO for SATCOM using the polarization domain is a useful method to minimize the mutual interference between the two antenna polarizations that arise from polarization tilt angle and AR differences.

## 4.4 Spatial and Polarization Multiplexing

In this section, an example case study is used to analyse the MIMO capacity utilising both spatial and polarization multiplexing. In X-band, orbital slots for multiple satellites within two degrees are generally not viable due to adjacent satellite interference issues from small user antenna terminals. A system concept to utilise MIMO in both the spatial and polarization domains is shown in Figure 4.6.

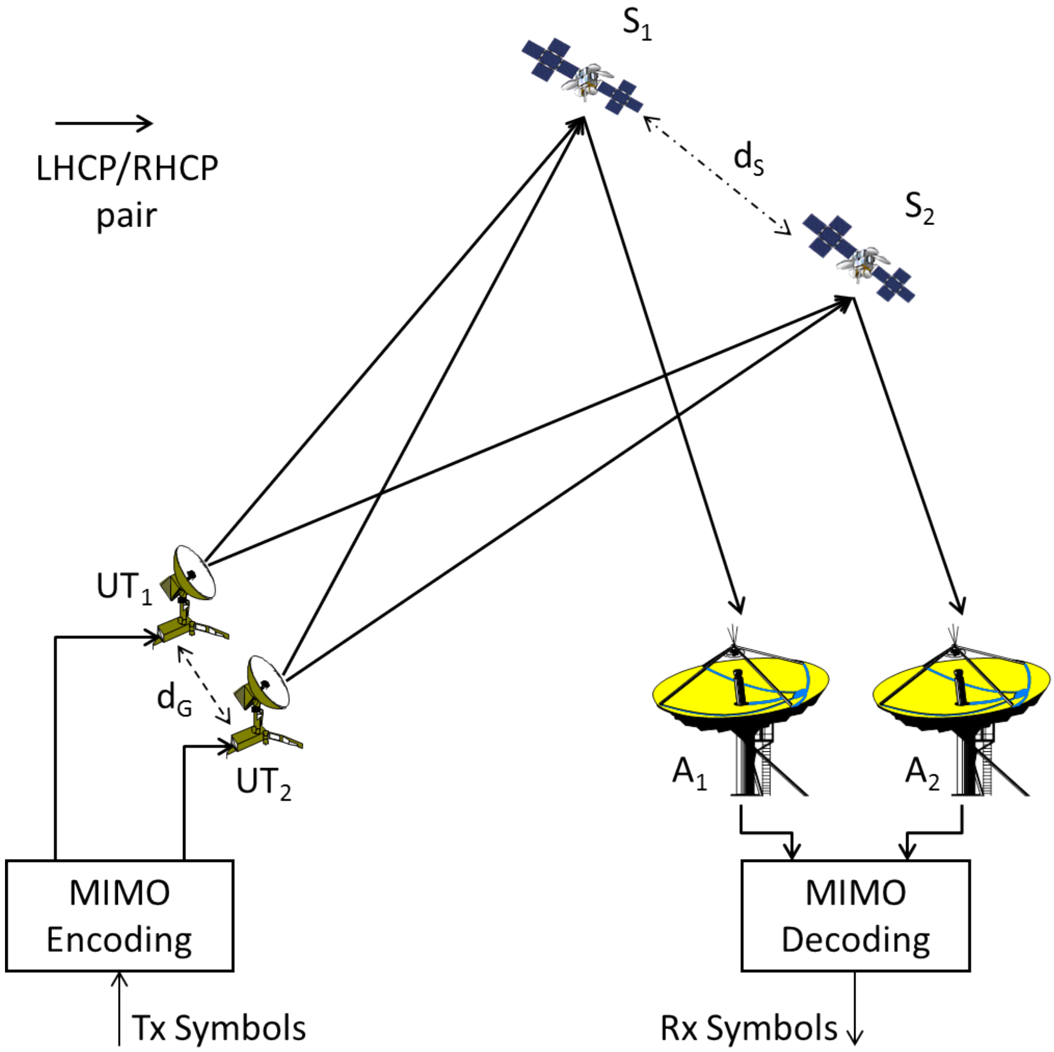


Figure 4.6: System concept for 4×4 uplink MIMO channel

In this case the uplink is a MIMO channel and downlinks from each satellite to its respective anchor station are SISO links. In the uplink, $N$ transmit DP antennas are arranged in an uniform linear array (ULA) separated by distance $\mathrm{d_G}$. In this analysis, the number of satellites is restricted to two ($M = 2$). The satellite antennas are DP on both the user and anchor links. We assume that the orbital spacing between the satellites corresponds to the longitudinal range of 0.5 to 2 degrees. Overall the number of degrees of freedom in the channel cannot be greater than four.

The overall channel matrix includes the uplink $\mathbf{H}_u \in \mathcal{C}^{2M\times 2N}$, the satellite $\mathbf{H}_s \in \mathcal{C}^{2M\times 2M}$ and the downlink $\mathbf{H}_d \in \mathcal{C}^{2M\times 2M}$ channel components, where the factor 2 is used to denote the DP antennas. The uplink MIMO channel matrix is given by:

$$\mathbf{H}_u = \begin{bmatrix} \mathbf{H}_{u,11} & \mathbf{H}_{u,12} \\ \mathbf{H}_{u,21} & \mathbf{H}_{u,22} \end{bmatrix}, \tag{4.19}$$

where,

$$\mathbf{H}_{u,mn} = a_{u,mn}\, g_{u,mn}\, \mathit{\Delta}_{u,mn} e^{-j\phi_{u,mn}} \quad m,n \in \{1,2\}, \tag{4.20}$$

where $\mathit{\Delta}$ is from (4.15). In an ideal polarization state $\mathit{\Delta}_u$ will be a $2\times 2$ identity matrix. Similarly the downlink channel matrix is given by:

$$\mathbf{H}_d = \begin{bmatrix} \mathbf{H}_{d,11} & 0_{2\times 2} \\ 0_{2\times 2} & \mathbf{H}_{d,22} \end{bmatrix}, \tag{4.21}$$

where,

$$\mathbf{H}_{d,mm} = a_{d,mm}\, g_{d,mm}\, \mathbf{I}_2 e^{-j\phi_{d,mm}} \quad m \in \{1,2\}, \tag{4.22}$$

The satellites are non-regenerative and the satellite transfer function can be expressed simply as a diagonal matrix:

$$\mathbf{H}_s = g_s \mathbf{I}_{2M}. \tag{4.23}$$

The overall transfer function of the system is similar to (3.23):

$$\mathbf{y} = \mathbf{H}_d\mathbf{H}_s\mathbf{H}_u\mathbf{x} + \mathbf{H}_d\mathbf{H}_s\mathbf{w}_u + \mathbf{w}_d \tag{4.24}$$

where we further define $\mathbf{H}_t = \mathbf{H}_d\mathbf{H}_s\mathbf{H}_u$ as the overall channel matrix and $\mathbf{x} \in \mathcal{C}^{2N\times 1}$ and $\mathbf{y} \in \mathcal{C}^{2M\times 1}$ are the transmit and receive signals, respectively.

Using SVD (Chapter-2, 2.4.1) the channel matrix can be decomposed as follows:

$$\mathbf{H}_t = \mathbf{U}\Lambda\mathbf{V}^\dagger, \tag{4.25}$$

where $\mathbf{U} \in \mathcal{C}^{2M\times 2M}$, $\mathbf{V} \in \mathcal{C}^{2N\times 2N}$ are unitary matrices, and $\Lambda \in \Re^{2M\times 2N}$ is a singular value matrix. The diagonal elements of $\Lambda$ are non-negative real valued singular values $(\lambda_1 \geq \lambda_2 ... \geq \lambda_k)$ and the off diagonal elements are zeros, where $k$ signifies the number of non-zero eigenvalues or the channel rank $(k \leq \min\{2M, 2N\})$ as per (2.16).

By substituting (4.25), $\mathbf{x} = \mathbf{V}\widetilde{\mathbf{x}}$ and $\widetilde{\mathbf{y}} = \mathbf{U}^\dagger\mathbf{y}$ in (4.24):

$$\widetilde{\mathbf{y}} = \mathbf{U}^\dagger\mathbf{U}\Lambda\mathbf{V}^\dagger V\widetilde{\mathbf{x}} + \mathbf{U}^\dagger\mathbf{H}_d\mathbf{H}_s\mathbf{w}_u + \mathbf{U}^\dagger\mathbf{w}_d, \tag{4.26}$$

$$= \Lambda\widetilde{\mathbf{x}} + \widetilde{\mathbf{w}}_u + \widetilde{\mathbf{w}}_d. \tag{4.27}$$

Since $\mathbf{U}$ is an unitary matrix, the distribution of $\widetilde{\mathbf{w}}_d$ will be same as $\mathbf{w}_d$ ($\widetilde{\mathbf{w}}_d \sim \mathbb{C}\mathcal{N}(0, \sigma^2_{w,d}\mathbf{I}_{2M})$) . However, the distribution of $\widetilde{\mathbf{w}}_u$ is dependent on the orthogonality of the $\mathbf{H}_d\mathbf{H}_s$ matrix product. In this analysis, for convenience we assume an ideal unity gain satellite and downlink channel such that the distribution of $\widetilde{\mathbf{w}}_u$ will be same as $\mathbf{w}_u$ ($\widetilde{\mathbf{w}}_u \sim \mathbb{C}\mathcal{N}(0, \sigma^2_{w,u}\mathbf{I}_{2M})$). The ideal channel assumes the downlink DP antenna polarizations are orthogonal and the two SISO links are completely isolated. The SVD channel model is shown in Figure 4.7.

The channel capacity is given by:

$$C = \sum_{i=1}^{2M} \log_2\left(1 + \frac{\tilde{S}_i}{\sigma^2_{w,u} + \sigma^2_{w,d}}\lambda_i^2\right) \qquad \text{bits/s/Hz}. \tag{4.28}$$

The capacity is modified from (2.23) to include both uplink and downlink noise components. Let $\widetilde{S}$ denote total transmit signal power before the $\mathbf{V}$ matrix and $S$ denote power after the $\mathbf{V}$ matrix. Since $\mathbf{V}$ is unitary, $\widetilde{S} = S$ so we can write:

$$\widetilde{S} = \sum_{i=1}^{2M} \widetilde{S}_i = \sum_{n=1}^{2N} S_n = S, \tag{4.29}$$

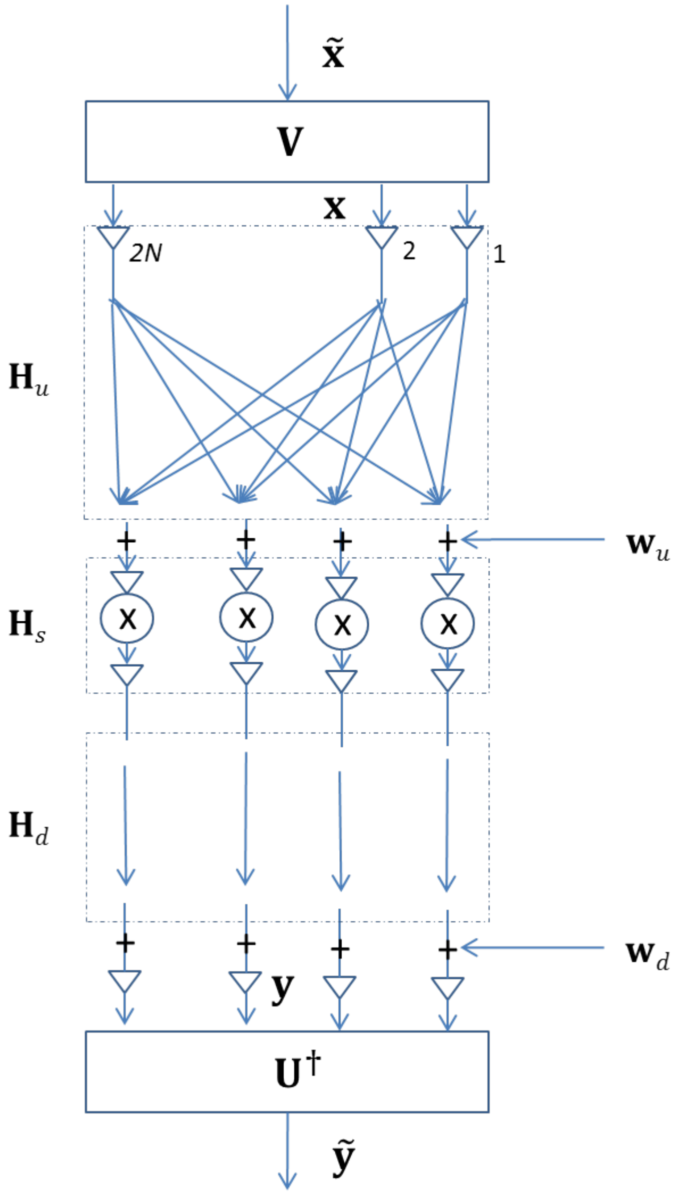


Figure 4.7: SVD model for spatial and polarization multiplexing

where $2M$ is the number of data streams transmitted using $2N$ channel paths ($N \geq M$). The total transmit signal power is constant irrespective of the total number of transmit antennas. Power allocation using the water-filling method is an optimum strategy to maximize capacity [27].

$$\widetilde{S}_i = \left(\mu - \frac{\sigma_{w,u}^2 + \sigma_{w,d}^2}{\lambda_i^2}\right)^+, \tag{4.30}$$

where $\mu$ is a parameter to satisfy the total power constraint in (4.29) and $(x)^+$ denotes $\max\{0, x\}$.

Table 4.1: System parameters for Spatial and Polarization MIMO in X-band

| Parameter | Value |
|---|---|
| $S_1$ orbital position | $156^o$ E |
| $S_2$ orbital position | $157^o$ E |
| $UT_1$ and $UT_2$ locations | $35^o$S $138^o$E |
| $d_G$ | $\approx 1$ m |
| X-band uplink $f_u$ | 8.15 GHz |
| Noise variance | $\sigma^2_{w,u} = \sigma^2_{w,d}$ |

The antennas are arranged in an uniform linear array (ULA) along the East-West orientation with spacing $d_G$ between the antennas. The achievable capacity using the SVD technique and the water-filling power allocation method is shown in Figure 4.8 with respect to $d_G$ and $N$. The calculations assume the parameters in Table 4.1 for the location of the satellites in the geostationary orbit, uplink frequency, and transmit location on the ground for the UTs. The spatial orthogonality is achieved by satisfying the range relationship in (3.21).

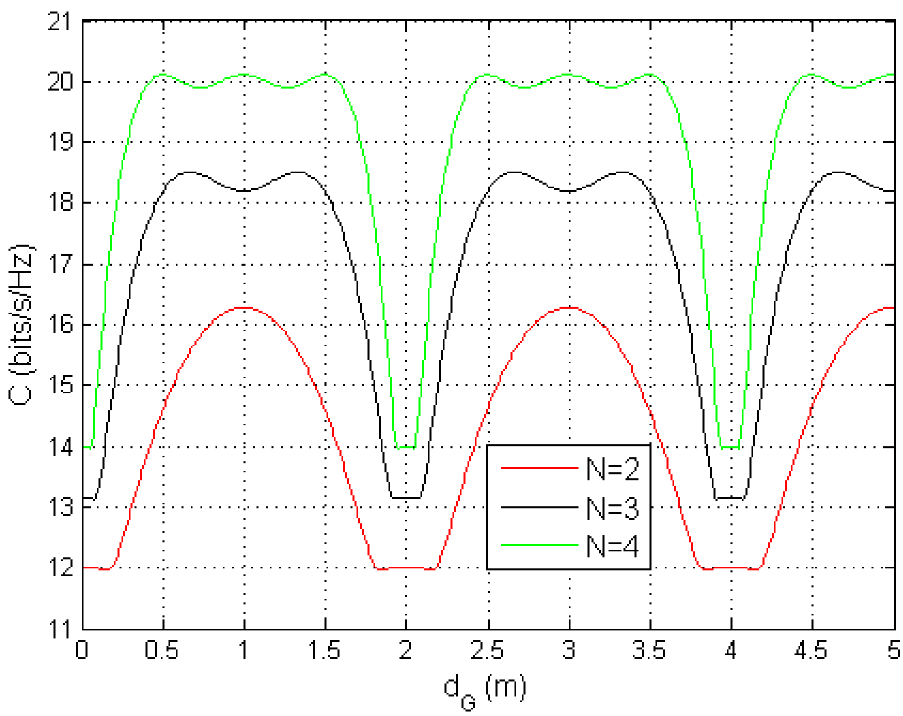


Figure 4.8: Capacity with respect to $d_G$ at 15 dB SNR with $N$ ideal DP antennas

The larger N, the less the capacity results are prone to antenna miss-positioning error in $d_T$. This result agrees with analysis presented in [19], however, the authors did not consider dual polarization. The effects of non-ideal DP antennas are analysed in next section. At non-optimum $d_G$ values, for example at 2m and 4m separations, the water-filling power allocation algorithm (4.30) ceases allocating power to low singular value channel streams. The incremental capacity obtained with more transmit antennas $N$ is an additional benefit from beamforming. The incremental capacity gain from beamforming is due to the channel state information available at the transmitter (CSIT) and for high SNRs it can be calculated as $\max\left(2M\log_2\left(\frac{N}{M}\right),0\right)$[6], where the multiplicative factor 2 denotes the two polarizations. The incremental capacity from increasing $N$ can be traded-off to reduce each transmit antenna size. For a parabolic antenna with diameter $D$, the maximum antenna gain at boresight is given by:

$$g^{\text{ant}} = \frac{\pi D f}{c}. \tag{4.31}$$

Reducing each antenna size by $\sqrt{N}$, the combined overall antenna area $\sum^{N}\pi\left(\frac{D}{2\sqrt{N}}\right)^2$ remains the same irrespective of $N$. The effect on capacity of reducing the transmit antenna size in this way as $N$ increases is illustrated in Figure 4.9 with respect to $\mathrm{d_G}$ at 15 dB SNR. The application of water-filling (WF) power allocation with respect to equal (EQ) power allocation is also compared in Figure 4.9. The WF method has no real advantage over EQ power allocation when the antenna spacing is optimal or close to being optimal. For the scenarios where the antenna spacing is close to the "worst case", the WF power allocation recognises the reduction in the channel rank and allocates the power to the two remaining independent polarizations. The SVD advantage is to make use of the CSIT and allocate the transmit power efficiently to the streams with stronger singular values.

In Figure 4.10, the WF capacity for $\mathrm{d_G}$ values at 1m and 2m separations, respectively, are shown. At high SNR values ($>$ 9 dB), better capacity is achieved when $\mathrm{d_G} = 1\mathrm{m}$, which is an optimal $\mathrm{d_G}$ value for spatial multiplexing. However, at low SNR values ($\leq$ 9dB), the capacity results are better at $\mathrm{d_G} = 2\mathrm{m}$, which is a non-optimal $\mathrm{d_G}$ value for spatial multiplexing but favourable to achieve beamforming gain. Here

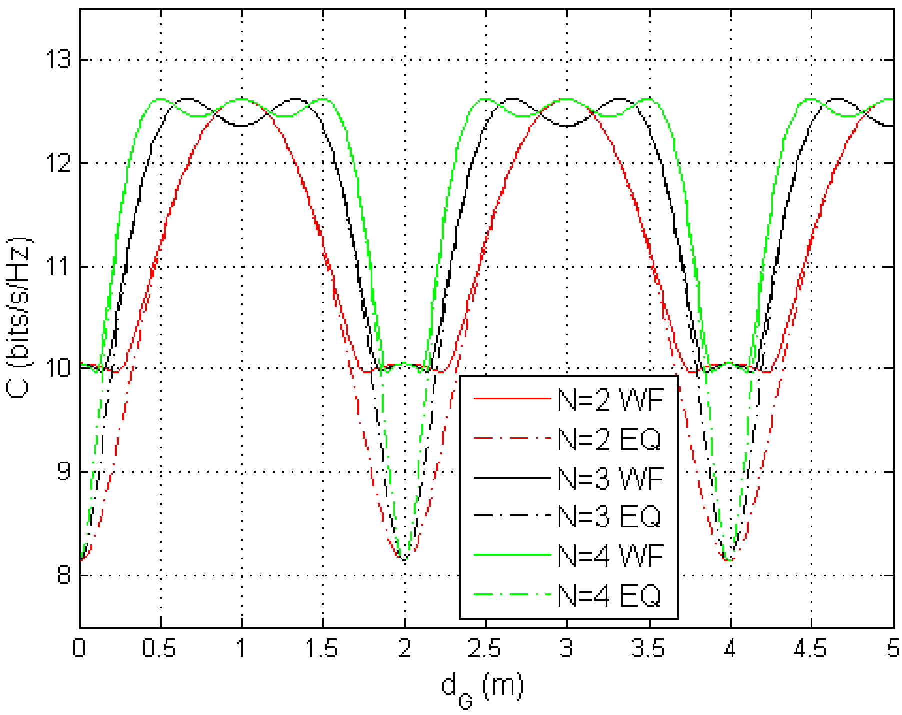


Figure 4.9: Tx antenna size scaled with respect to N: Capacity with respect to $d_G$ at 15 dB SNR with ideal DP antennas and comparison of WF and EQ power allocations

the water-filling power allocation method benefits the capacity by beamforming instead of spatial multiplexing. Single satellite SISO capacity is shown for comparison to appreciate the benefit of MIMO.

## 4.5 Non-Ideal DP Antennas

It is shown in Section 4.3 that in a MIMO context, the term polarization parallelity is a significant performance indicator when using multiple polarizations, and is more indicative of the performance than AR, XPD or XPI. A random uniform error distribution in amplitude $U(\frac{1}{1.3}, 1.3)$ and phase $U(-10^o, +10^o)$ using equation (4.13) gives a histogram for $p$ from $-24$ dB to $-6$ dB and mode lies at $-9$ dB as shown in Figure 4.11. The histogram analysis on the $p$ value for the given distribution range shows the most occurrence between approximately -11 to -7 dB. This can be used to asses

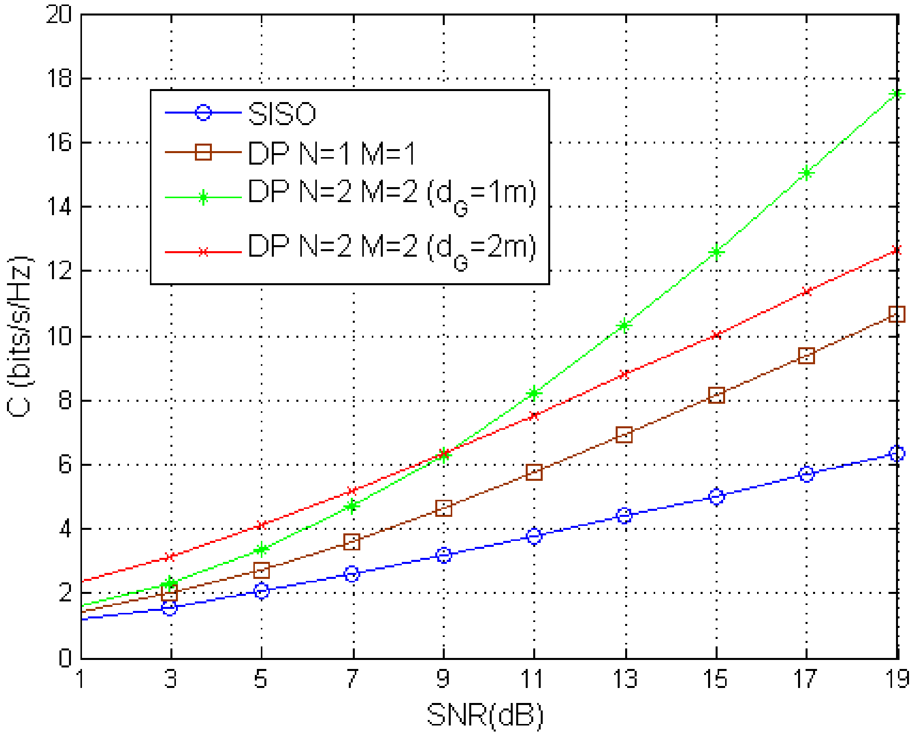


Figure 4.10: Tx antenna size scaled with respect to $N$: Capacity with respect to SNR with ideal DP antennas

the impact of non-ideal DP antennas using the case study analysis presented in the previous section.

The effect of different $p$ values on the achievable capacity is shown in Figure 4.12 using (4.28)[2]. The 'green' plot in Figure 4.12 can be compared with the 'green' plot in Figure 4.10, both represents the same capacity values in an ideal polarization state. As the $p$ values of the antennas increase from zero (ideal state) and approach toward one, we can see the drop in achievable channel capacity in Figure 4.12. The histogram analysis in Figure 4.11 shows that in practice $p = -9$ dB is a likely value for polarization parallelity for DP antennas in a MIMO link. For $p = -9$ dB, approximately ten percent of the capacity is lost at high SNRs due to non-ideal DP antennas.

In a MIMO system, this capacity loss due to non-ideal DP antennas is practically expected while taking advantage of multiplexing in the polarization domain. However,

[2]Note that the equation (4.28) takes into account the effects of both spatial and polarization multiplexing.

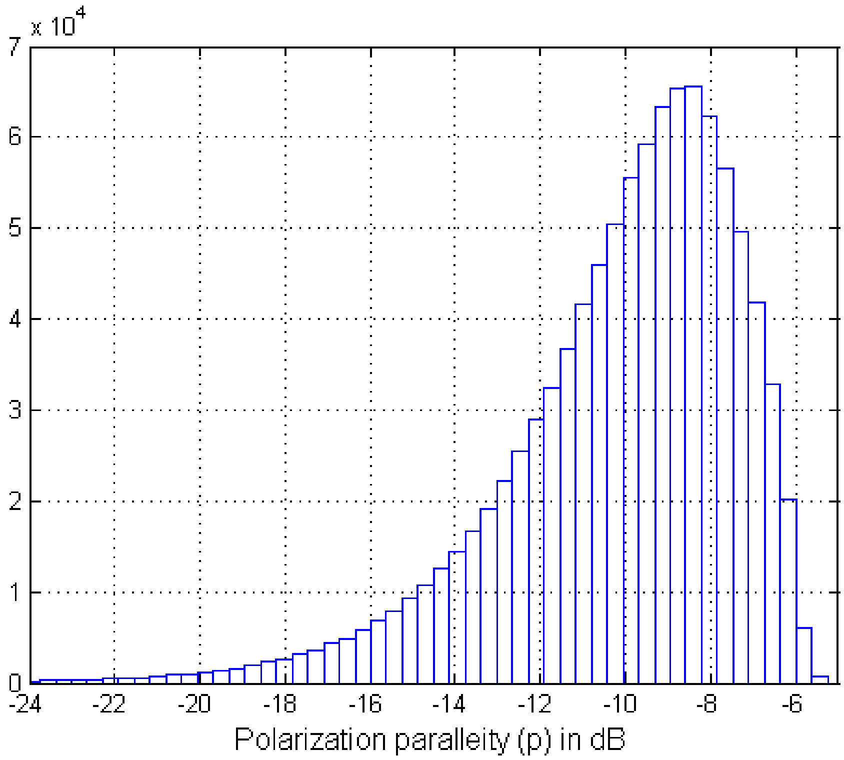


Figure 4.11: Histogram for polarization parallelity with uniform error distribution in amplitude $U(\frac{1}{1.3}, 1.3)$ and phase $U(-10^o, +10^o)$

the capacity loss in a MIMO context is significantly less compared to the XPI impact scenario analysed in Section 4.2.1, when the two polarizations are simultaneous used as two independent SISO systems.

The capacity using non-ideal DP antennas is analysed along with antenna spacing constraints in Figure 4.13 and Figure 4.14 for $N = 2$ and $N = 3$, respectively. The ideal DP antenna state is denoted by $p = -\infty$ and corresponds with the plots in Figure 4.9. The results shows that the non-ideal DP antennas used for polarization multiplexing does not alter the spatial antenna spacing requirement for spatial multiplexing. However, depending on the $p$ value, there is an inevitable loss in the channel capacity irrespective of the spatial antenna spacing. Note that for a given $p$ value in the analysis, all the antennas both in the transmit and receive have same $p$ value, but may have different amplitude and phase polarization excitation errors. In all the scenarios, the results show that there's no tangible advantage in using WF transmit

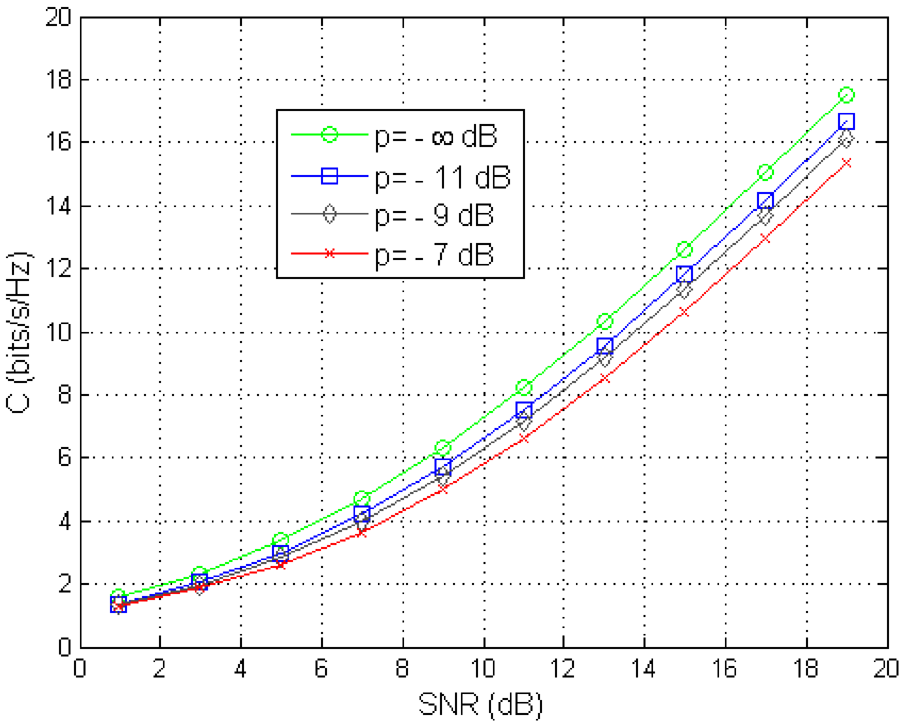


Figure 4.12: Polarization impact on capacity at optimal $d_T$ (1m) ($N = M = 2$) using EQ power allocation

power allocation technique over EQ power allocation to counter the effects of non-ideal DP antennas when the spatial arrangement is near optimum.

## 4.6 Chapter Review

The use of orthogonal polarizations is a well known frequency reuse technique in SATCOM. However, poor cross polar isolation can significantly degrade system performance. In this chapter, the XPI impact on communications system performance was analysed and it was shown that the poor cross polar isolation can be caused by non-ideal circular DP antennas and due to tilt angle differences. In this chapter, an antenna model for circular DP antennas was given and it was shown that the orthogonality of the antenna polarization can be expressed in-terms of polarization parallelity. In a MIMO context, the term polarisation parallelity is shown to have more significance in-terms of assessing the MIMO capacity than traditionally used power ratios includ-

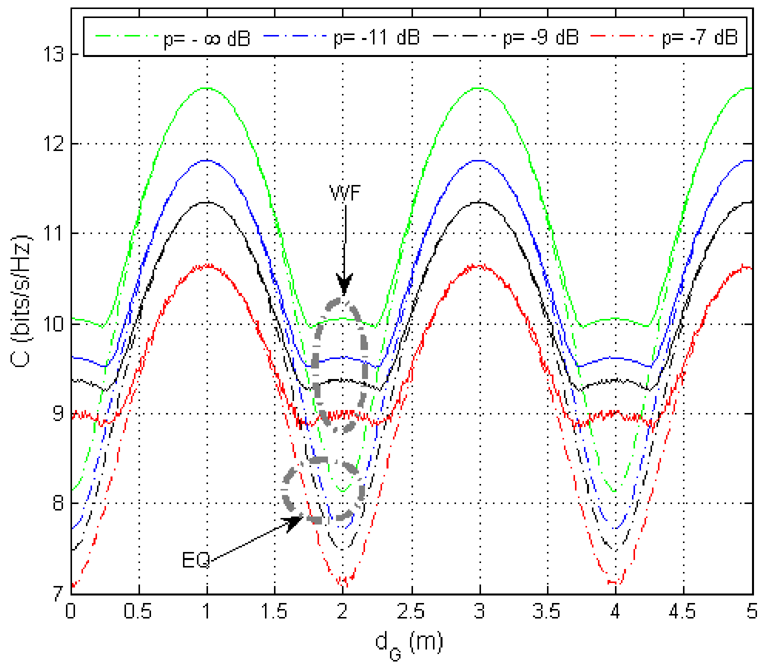


Figure 4.13: Tx antenna size scaled with respect to $N = 2$: Capacity with respect to $\mathrm{d_G}$ at 15 dB SNR under different $p$ values

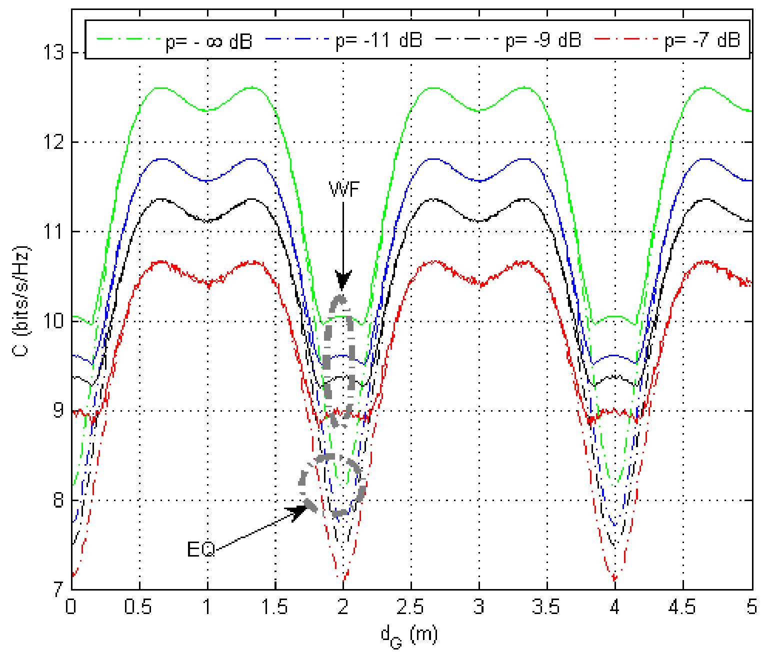


Figure 4.14: Tx antenna size scaled with respect to $N = 3$: Capacity with respect to $\mathrm{d_G}$ at 15 dB SNR under different $p$ values

ing XPD and XPI. The MIMO polarization multiplexing was investigated along with spatial multiplexing for SATCOM using a case study with two satellites in X-band MILSATCOM. The advantage of MIMO polarization is two fold. The first is as a technique to counter poor cross polar isolation (XPI) and the second is to approximately double the available spatial multiplexing gain and is less sensitive to the degradation from poor XPI than using the two SISO approach. Capacity analysis shows that at high signal-to-noise ratios (SNR) significant capacity gain can be achieved through spatial multiplexing. However, at low SNR especially with channel state information available at the transmitter (CSIT) the MIMO channel benefits from beamforming.

# Chapter 5

# MIMO Spatial Multiplexing: Single Satellite Systems

Next generation geo-stationary SATCOM systems in Ka-band are positioning aggressively in-terms of throughput and capacity. High Throughput Satellites (HTS) and High Capacity Satellites (HiCapS) are two main categories of satellite systems that have emerged [16]. A HTS system typically utilises many fixed spot beams covering multiple small footprints on the ground. The main aim of a HTS system is to increase the overall throughput of a satellite by frequency reuse between the spot beams, using at-least four or more frequency colours. In contrast, the aim of a HiCapS system is to focus capacity in a smaller region. HiCapS systems typically have multiple steerable spot beams serving any area of Earth visible from the satellite. WGS[1] is an example of HiCapS system with eight steerable spot beams in Ka-Band.

A number of possible selection criteria may influence the choice between HTS or HiCapS systems. Military users may tend to favour HiCapS, as they demand more capacity in a single region rather than overall global throughput from HTS. Reducing the number of frequency colours in a HTS system will increase the bandwidth available in each spot beam and can boost the overall throughput, but at a cost of increased interference to the users at the edge of the beams. The application of MIMO and

[1]Wideband Global SATCOM (WGS) is US DOD's high capacity satellites, where Australia is a partner

multi-user detection (MUD) techniques have been analysed to mitigate the interference [34, 35, 36] and these studies show an improvement in the system performance.

The SATCOM channel, especially at X, Ku and Ka band frequencies, is principally dominated by the LOS path. It is well known that the absence of scatterers may lead to rank deficiency in the channel matrix as LOS conditions are not suited for point-to-point MIMO. However, it was explained in Chapter-2 that geometrical optimisation using geographically displaced antenna separation at the ground or space can provide extra degrees of freedom. In Chapter-3, it was shown that MIMO using multiple satellites is an attractive application at lower frequency bands, especially at UHF SATCOM to enhance capacity by orbital frequency reuse.

A multi-user (MU) MIMO spatial multiplexing technique is proposed in this chapter to enhance the channel capacity of a HiCapS system in a constrained geographical region by enabling frequency reuse. The main advantages of the MU-MIMO technique are; each user requires only a single antenna terminal and it is applicable in LOS channels. The channel capacity can be linearly increased utilising multiple spot beam antennas on a single satellite serving the considered geographical region. In [14], MU-MIMO has been suggested as a potential solution to achieve frequency reuse in SATCOM with a scattered user distribution. In this chapter, we expand on the MU-MIMO and spatial multiplexing techniques to show how this can be applied to SATCOM to increase the capacity of a HiCapS system.

A system model is presented in Section-5.1 to introduce the concept. Optimal location contours for multiple orthogonal users using $2 \times 2$ and $4 \times 4$ MIMO scenarios are described in Section-5.2. The channel capacity is analysed in Section-5.3 and the impact of sub-optimal user location is analysed in Section-5.4. A simulation framework is presented in Section-5.5 using linear MIMO decoding techniques such as the Zero Forcing (ZF) filter and Minimum Mean Square Error (MMSE) filter. This section also includes BER simulation results using an uplink $4 \times 4$ MU-MIMO channel.

Table 5.1: System parameters for MU-MIMO SATCOM in Ka-band

| **Parameter** | **Value** |
|---|---|
| Satellite | $156^o$ E |
| Frequency $f$ | 30 GHz |
| Beam centre | $34^o$S $145^o$E |
| Beam coverage radius | $\approx$ 2000 km |
| Minimum $\mathrm{d_G}$ | $\approx$ 95 km |

## 5.1 System Model

The system concept is show in Figure 5.1. A notional satellite in the 156°E location is considered with multiple antennas pointing to a constrained region in the order of 1000 km diameter. For $M$ antennas in space, in this case on a single satellite, the idea is to group multiple sets of $N$ users from a distributed user set on the ground to reuse the same frequency. Each user has a single antenna. In Figure 5.1, $M = 2$ antennas on the satellite can support orthogonal user groups of $N = 2$ users for spatial multiplexing. It is assumed that the demodulation and decoding are done on board the satellite or orthogonal parallel paths exist between the satellite and the anchor stations. The analysis in this chapter is restricted only to the MU-MIMO channel between the users and the satellite and assumes an ideal link between the satellite and anchor stations. MIMO decoding and precoding are required at the satellite or at anchor stations to support the user uplink and downlink, respectively. In either the user uplink or downlink, the multiple user are not required to be cooperative with each other. However, the users are assumed to be spatially distributed in the region. This chapter mainly focuses on the uplink channel analysis from multiple users to the satellite in Ka-band. The system parameters are listed in Table 5.1. The channel matrix is denoted by $\mathbf{H} \in \mathbb{C}^{M \times N}$, where $M$ is the number of antennas in use on the satellite and $N$ is the number of single antenna users on the ground. Ideally, to maximise channel capacity, the requirement would be to have $N$ $(= M)$ spatially orthogonal users from a distributed user set, to reuse the same frequency $M$ times. We

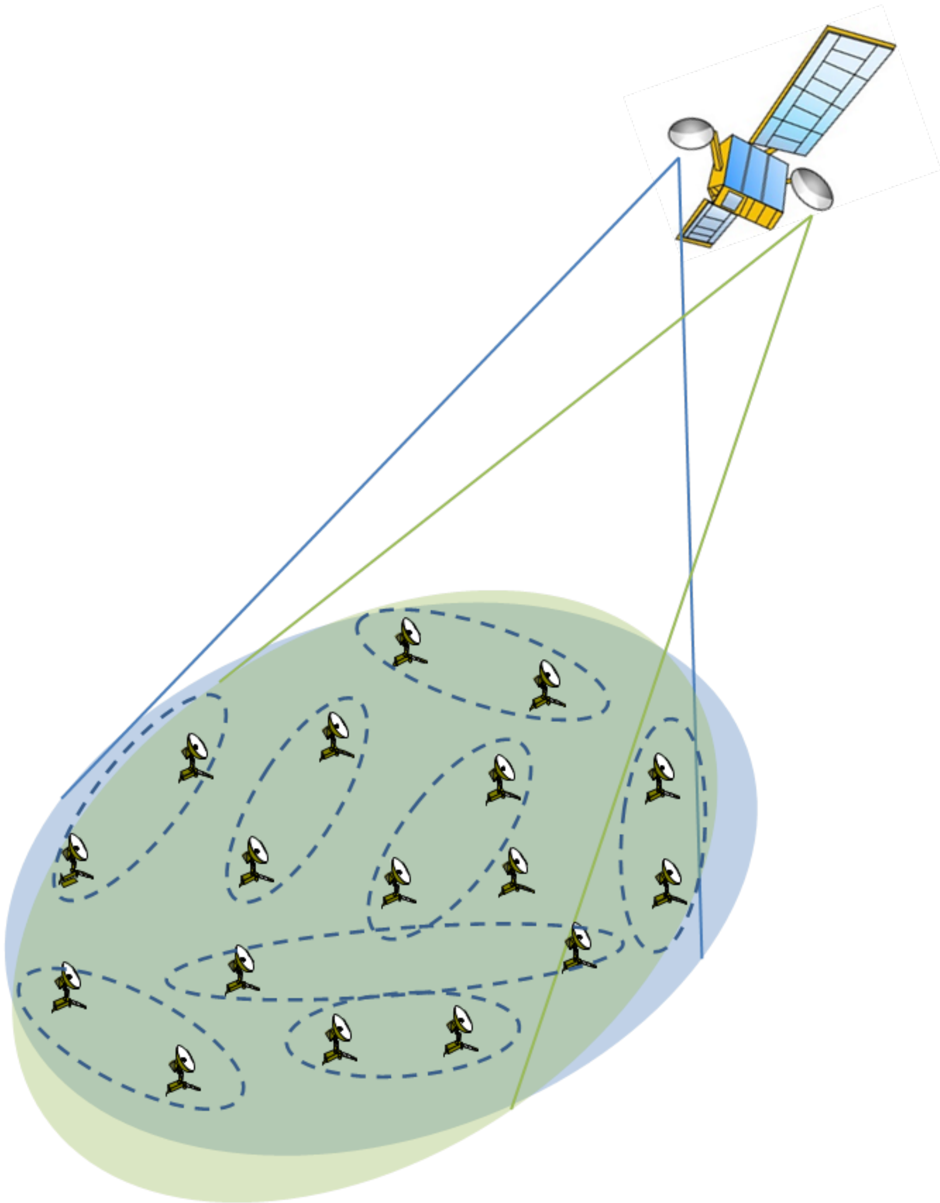

Figure 5.1: System concept for spatial multiplexing in single satellite systems

define the user to satellite channel matrix as:

$$\mathbf{H} = \begin{pmatrix} h_{11} & h_{12} & . & . & h_{1N} \\ h_{21} & h_{22} & . & . & h_{2N} \\ . & . & . & . & . \\ . & . & . & . & . \\ h_{M1} & h_{M2} & . & . & h_{MN} \end{pmatrix}, \tag{5.1}$$

$$h_{mn} = a_{mn} g_{mn} e^{-j\phi_{mn}}, \tag{5.2}$$

where the channel path attenuation $a_{mn}$ and the deterministic phase component $\phi_{mn}$ in each channel path element are given in (2.4) and (2.3), respectively. It is reasonable to approximate the channel path attenuation as $a_{mn} \approx a$ for simplification purposes and to assume that antenna gain is constant across all users, $g_{mn} \approx g$ [2], such that:

$$\mathbf{H} = ag\widetilde{\mathbf{H}}. \tag{5.3}$$

Let $\Upsilon \in \mathbb{C}^{M \times M}$ denote the matrix product $\widetilde{\mathbf{H}}\widetilde{\mathbf{H}}^{\dagger}$, $\Upsilon$ is required to be a diagonal matrix to ensure orthogonality between the users:

$$\Upsilon = \widetilde{\mathbf{H}}\widetilde{\mathbf{H}}^{\dagger} = \begin{pmatrix} \zeta_{11} & \zeta_{12} & . & . & \zeta_{1M} \\ \zeta_{21} & \zeta_{22} & . & . & \zeta_{2M} \\ . & . & . & . & . \\ . & . & . & . & . \\ \zeta_{M1} & \zeta_{M2} & . & . & \zeta_{MM} \end{pmatrix}, \tag{5.4}$$

$$\zeta_{il} = \sum_{n=1}^{N} e^{-j2\pi \frac{f}{c}(r_{in} - r_{ln})} \qquad i, l \in \{1, 2...M\}, \tag{5.5}$$

$$\zeta_{li} = \zeta_{il}^{*}, \tag{5.6}$$

where $\{i, l\}$ are index for the satellite antennas. Since $\widetilde{\mathbf{H}}$ is a square matrix, the channel is spatially orthogonal if the off-diagonal elements of $\Upsilon$ are zeros.

$$\zeta_{il} = \begin{cases} N, & \text{if } i = l, \\ 0, & \text{otherwise.} \end{cases} \tag{5.7}$$

Distinct phase relationships are required in $\widetilde{\mathbf{H}}$ to satisfy (5.7). Alternatively, for a given frequency $f$, a distinct range relationship is required between the user terminals (UT) and the satellite antennas. In Chapter-2, the required range relationship from

[2] In the real world, this would vary by up to 3 dB between the users. However, the gain variation will not be an issue to achieve user orthogonality.

geometrical optimisation is given in (2.9)[3]. The solution in (2.9) is limited to $M = 2$, in this chapter we extend the geometrical optimisation technique to achieve full $M$ spatial degrees of freedom, as given in (5.8).The first user (UT1) is treated as a primary user and the other users denoted by $q \in \{2, 3...N\}$ are chosen with reference to UT1 to satisfy (5.8).

$$(r_{i1} - r_{l1}) - (r_{iq} - r_{lq}) = (l - i)\{M\kappa_q + (q - 1)\}\frac{c}{f}\frac{\nu}{M}, \tag{5.8}$$

where $\kappa_q$ and $\nu$ are integer-valued phase periodicity factors. The range relationship in (5.8) is an extended version of (2.9) for $M > 2$. The greatest common divisor (GCD) between $\nu$ and $M$ must be equal to one, i.e. they are relatively prime:

$$\mathrm{GCD}\{\nu, M\} = 1, \tag{5.9}$$

$$\kappa_q \in \{... - 2, -1, 0, 1, 2...\}. \tag{5.10}$$

Later in this chapter, it is shown in (5.12) and (5.16), how the sum value of the complex coefficients equals to zero in the $2 \times 2$ and $4 \times 4$ scenarios, respectively. The spatial range relationship values from (5.8) for all satellite antenna pairs $\{i, l\}$ with respect to UT$q$ are given in Table 5.2 for a $4 \times 4$ MU-MIMO channel example. Each row in Table 5.2 represents a UT with index $q$ and each column represent a satellite antenna pair with index $\{i, l\}$.

## 5.2 MU-MIMO Scenarios

In this scenario, we consider a uniform linear array (ULA) configuration for the satellite antennas as shown in Figure 5.2, where $\mathrm{d_S}$ is the uniform spacing between each antenna.

[3]However, the case here is different from Chapter-2. In this case the UTs are independent and are not required to communicate with each other.

Table 5.2: Spatial range relationship (4 × 4 MU-MIMO channel scenario)

| $\{i,l\}$ | **{1,2}** | **(1,3)** | **{1,4}** | **{2,3}** | **{2,4}** | **{3,4}** |
|---|---|---|---|---|---|---|
| $q=2$ | $(4\kappa_2+1)\frac{c}{f}\frac{\nu}{4}$ | $(8\kappa_2+2)\frac{c}{f}\frac{\nu}{4}$ | $(12\kappa_2+3)\frac{c}{f}\frac{\nu}{4}$ | $(4\kappa_2+1)\frac{c}{f}\frac{\nu}{4}$ | $(8\kappa_2+2)\frac{c}{f}\frac{\nu}{4}$ | $(4\kappa_2+1)\frac{c}{f}\frac{\nu}{4}$ |
| $q=3$ | $(4\kappa_3+2)\frac{c}{f}\frac{\nu}{4}$ | $(8\kappa_3+4)\frac{c}{f}\frac{\nu}{4}$ | $(12\kappa_3+6)\frac{c}{f}\frac{\nu}{4}$ | $(4\kappa_3+2)\frac{c}{f}\frac{\nu}{4}$ | $(8\kappa_3+4)\frac{c}{f}\frac{\nu}{4}$ | $(4\kappa_3+2)\frac{c}{f}\frac{\nu}{4}$ |
| $q=4$ | $(4\kappa_4+3)\frac{c}{f}\frac{\nu}{4}$ | $(8\kappa_4+6)\frac{c}{f}\frac{\nu}{4}$ | $(12\kappa_4+9)\frac{c}{f}\frac{\nu}{4}$ | $(4\kappa_4+3)\frac{c}{f}\frac{\nu}{4}$ | $(8\kappa_4+6)\frac{c}{f}\frac{\nu}{4}$ | $(4\kappa_4+3)\frac{c}{f}\frac{\nu}{4}$ |

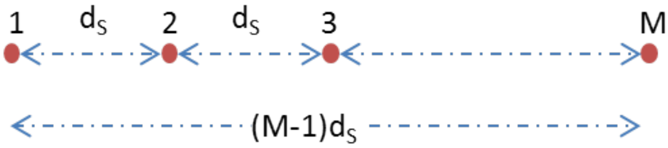


Figure 5.2: Satellite antennas in an ULA configuration

### 5.2.1 2 × 2 MU-MIMO scenario

In the 2 × 2 MU-MIMO scenario, the satellite has $M = 2$ spot beam antennas, both pointing to the same geographical region on the ground. In this scenario, for a given UT1 location the intention is to find an orthogonal user (UT2) such that both UT1 and UT2 can simultaneously reuse frequency as two parallel channels. The range relationship equation simplifies to (2.9):

$$(r_{11} - r_{21}) - (r_{12} - r_{22}) = \frac{c}{f}\frac{\nu}{2}. \tag{5.11}$$

The integer $\kappa_q = 0$ in this case and is ignored, because it has no significance in the 2 × 2 scenario. By satisfying (5.11), the channel will be spatially orthogonal for all values of $\nu$ that satisfy (5.9). From (5.5) and applying (5.11), we have:

$$\begin{aligned}\zeta_{12} &= e^{-j2\pi\frac{f}{c}(r_{11}-r_{21})} + e^{-j2\pi\frac{f}{c}(r_{12}-r_{22})} \\ &= e^{-j2\pi\frac{f}{c}(r_{11}-r_{21})}\{1 + e^{j\nu\pi}\}.\end{aligned} \tag{5.12}$$

Equation (5.12) will be zero for $\nu \in \{..., -3, -1, 1, 3...\}$.

At $f = 30$ GHz, $\mathrm{d_S} = 1$ m with UT1 located near Melbourne, Australia, another spatially orthogonal user (UT2) can be anywhere in locations shown by the contours in Figure 5.3[4]. Each contour line traces the locations on the Earth's surface that satisfies (5.11). From right to left, the $\nu$ values correspond to $\{-3, -1, 1, 3\}$, respectively. Numerical values corresponding to $(\frac{c}{f}\frac{\nu}{2})$ are displayed by each contour line. It is also important to note that the orientation of the satellite ULA configuration with respect to the East-West will change the orientation of the contours on the ground.

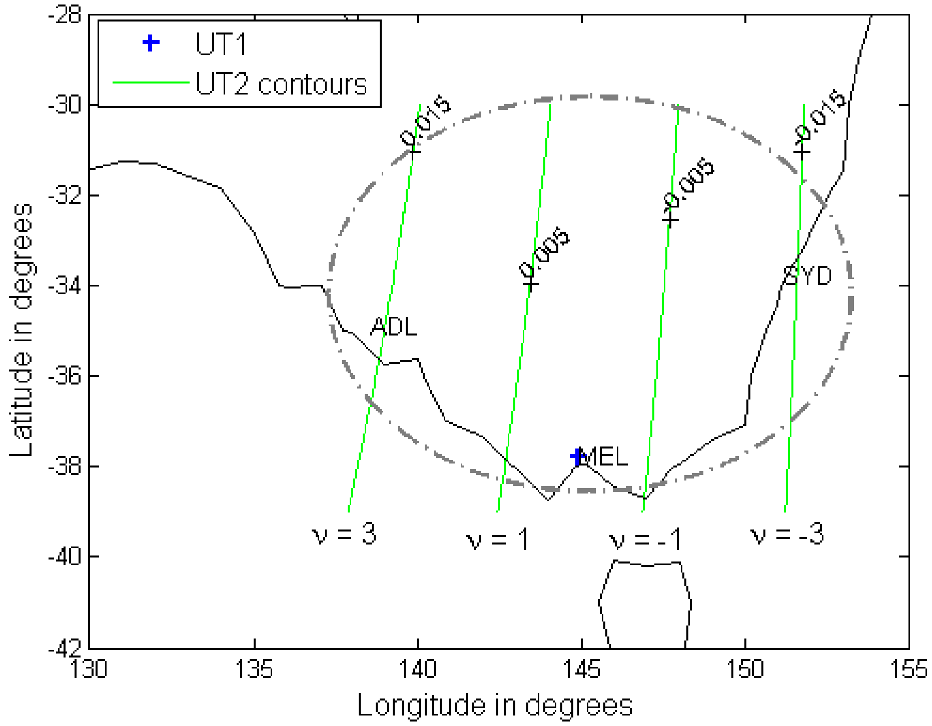


Figure 5.3: UT2 location contours for $f = 30$ GHz, $\mathrm{d_S} = 1$ m and $M = N = 2$

### 5.2.2 $4 \times 4$ MU-MIMO scenario

The concept is linearly scalable to any increasing value of $M$, but generally will be limited by practicality on the satellite. In the $4 \times 4$ scenario, for a given UT1 location, the intention is to find other orthogonal users UT2, UT3 and UT4 that are orthogonal in the channel to both UT1 and to each other. Thus all UTs can simultaneously reuse

[4] A circular spot beam footprint is shown for convenience. However, note that for the given satellite location and geographical location of the beam, the shape may not be circular as shown.

the same frequency creating $M$ parallel channels. A set of range relationship criteria must be met (as in Table 5.2) for all satellite antenna pairs $\{i,l\}$ and UTs with respect to UT1 location.

Let's assume $\nu = 1$ and $\kappa_q = 0$, the range relationship equation (5.8) simplifies as below for the satellite antenna pair $\{i,l\} = \{1,2\}$:

$$(r_{11} - r_{21}) - (r_{12} - r_{22}) = \frac{c}{f}\frac{1}{4}, \tag{5.13}$$

$$(r_{11} - r_{21}) - (r_{13} - r_{23}) = \frac{c}{f}\frac{2}{4}, \tag{5.14}$$

$$(r_{11} - r_{21}) - (r_{14} - r_{24}) = \frac{c}{f}\frac{3}{4}. \tag{5.15}$$

Using (5.5) and substituting (5.13),(5.14) and (5.15), it can be shown that an off-diagonal element of $\Upsilon$ can be equal to zero:

$$\begin{aligned}\zeta_{12} &= e^{-j2\pi\frac{f}{c}(r_{11}-r_{21})} + e^{-j2\pi\frac{f}{c}(r_{12}-r_{22})} + e^{-j2\pi\frac{f}{c}(r_{13}-r_{23})} + e^{-j2\pi\frac{f}{c}(r_{14}-r_{24})} \\ &= e^{-j2\pi\frac{f}{c}(r_{11}-r_{21})}\{1 + e^{j\frac{\pi}{2}} + e^{j\pi} + e^{j\frac{3\pi}{2}}\} = 0. \end{aligned} \tag{5.16}$$

The contour plots in Figure 5.4 correspond to optimal user locations for UT2, UT3 and UT4 that satisfy equations (5.13), (5.14) and (5.15), respectively. The contour numerical values in Figure 5.4 represents the respective range differences in meters.

Any locations on the green, red and magenta contour plots are optimal user locations for UT2, UT3 and UT4, respectively, for satellite antenna pair $\{1,2\}$. However, to satisfy the overall orthogonality of the channel matrix, the spatial range relationship must also be met for other satellite antennas pairs $\{1,3\}$,$\{1,4\}$, $\{2,3\}$, $\{2,4\}$ and $\{3,4\}$: such that the intersection point of all six contours determine the required location for each UT. A best solution is achieved when all the six contours completely overlap with each other, so any locations on the contour line can be an optimal user location rather than an intersection point. Based on the values in Table 5.2, two UT2 contours corresponding to satellite antenna pairs $\{1,2\}$ and $\{1,3\}$, respectively, can

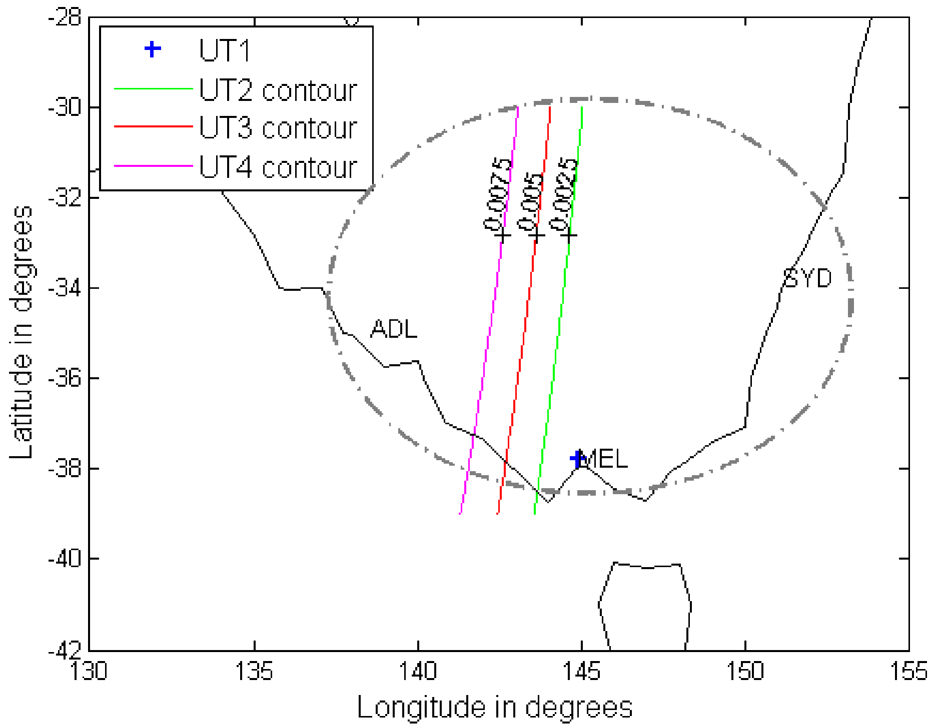


Figure 5.4: Location contours ($i = 1, l = 2$) at $f = 30$ GHz, $\mathrm{d_S} = 1$m, $\nu = 1$ and $\kappa_q = 0$

completely overlap each other if the following equation is held true:

$$(r_{11} - r_{31}) - (r_{12} - r_{32}) = 2\big\{(r_{11} - r_{21}) - (r_{12} - r_{22})\big\}. \tag{5.17}$$

This can be satisfied if:

$$(r_{11} - r_{31}) = 2(r_{11} - r_{21}), \tag{5.18}$$

$$(r_{12} - r_{32}) = 2(r_{12} - r_{22}). \tag{5.19}$$

This can be expressed in a generalised form for all UTs:

$$(r_{in} - r_{ln}) = (l - i)(r_{1n} - r_{2n}). \tag{5.20}$$

Equation (5.20) can be met if the satellite antennas are arranged in an ULA configuration as in Figure 5.2. To prove this, let's consider a geometrical representation of the satellite antenna with respect to UT as shown in Figure 5.5.

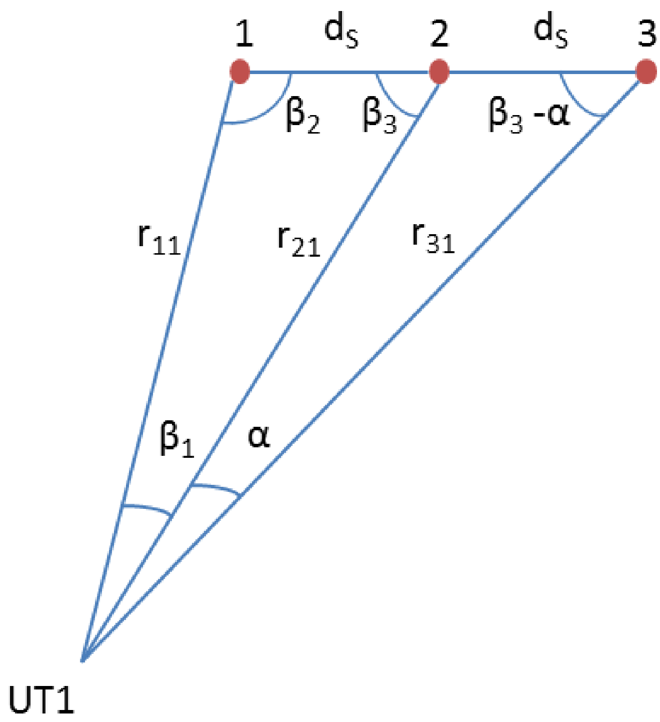


Figure 5.5: UT and Satellite ULA geometry

Using the law of sine for triangles:

$$\frac{\sin(\beta_1)}{\mathrm{d_S}} = \frac{\sin(\beta_2)}{r_{21}} = \frac{\sin(\beta_3)}{r_{11}}, \tag{5.21}$$

$$(r_{11} - r_{21}) = \mathrm{d_S}\{\frac{\sin(\beta_3) - \sin(\beta_2)}{\sin(\beta_1)}\}, \tag{5.22}$$

$$\frac{\sin(\beta_1 + \alpha)}{2\mathrm{d_S}} = \frac{\sin(\beta_2)}{r_{31}}, = \frac{\sin(\beta_3 - \alpha)}{r_{11}} \tag{5.23}$$

$$(r_{11} - r_{31}) = 2\mathrm{d_S}\{\frac{\sin(\beta_3 - \alpha) - \sin(\beta_2)}{\sin(\beta_1 + \alpha)}\}. \tag{5.24}$$

To prove (5.20) from (5.22) and (5.24), it is essential that the below equation must be satisfied from the antenna geometry:

$$\frac{\sin(\beta_3) - \sin(\beta_2)}{\sin(\beta_1)} = \frac{\sin(\beta_3 - \alpha) - \sin(\beta_2)}{\sin(\beta_1 + \alpha)}. \tag{5.25}$$

Since $\beta_1$ and $\alpha$ are extremely tiny angles, the sine and cosine function of those angles can be approximated as $\sin(\alpha) \approx \alpha$, $\cos(\alpha) \approx 1$ and $\sin(\beta_1 + \alpha) \approx \beta_1 + \alpha$:

$$\frac{\sin(\beta_3) - \sin(\beta_2)}{\beta_1} \approx \frac{\sin(\beta_3 - \alpha) - \sin(\beta_2)}{\beta_1 + \alpha}, \tag{5.26}$$

$$(\beta_1 + \alpha)\{\sin(\beta_3) - \sin(\beta_2)\} \approx \beta_1\{\sin(\beta_3) - \alpha\ \cos(\beta_3) - \sin(\beta_2)\}, \tag{5.27}$$

$$\alpha\{\sin(\beta_3) - \sin(\beta_2) + \beta_1\ \cos(\beta_3)\} \approx 0. \tag{5.28}$$

Equation (5.28) is valid, as long as the angles $\beta_1$ and $\alpha$ are extremely small angles, which holds if $\mathrm{d_S} \lll \mathrm{r}_{mn}$. Hence if the satellite antennas are in an ULA configuration, the generalised form of the requirement in (5.20) can be similarly proved geometrically for any $\{i, l\}$ and $n$.

The contours for UT2, UT3 and UT4 in Figure 5.6 and Figure 5.7 correspond to satellite antenna pairs $\{1, 3\}$ and $\{1, 4\}$, respectively. The contours completely overlap with each other and this can also be compared with Figure 5.4. However, please note that the respective range difference values (in meters) are different compared to Figure 5.4.

A complete set of user location contours are given in Figure 5.8 that satisfy the orthogonality of the channel matrix. Figure 5.8 is an example for case $\nu = 1$ and different $k_q$ values. However, all other users will be mutually orthogonal to each other and with UT1 if UT2, UT3 and UT4 are anywhere on the green, red and magenta coloured contour lines, respectively [5]. Similarly, Figure 5.9 shows the contours for $\nu = 3$, where the contours appear wide apart denoting the next periodic factor.

If the inter-antenna distance between the antennas on the satellite increases, the distance between each optimal user location contour decreases. An example is shown in Figure 5.10, where $\mathrm{d_S}$ is doubled to 2 m from the previous analysis in Figure 5.8 and the distance between the optimal location contours is approximately halved. This can be useful to satellite systems with high gain spot beam antennas with smaller spot diameter. This shows the technique can be applied to satellites with high gain antennas

[5] Note that only one UT can be located on each colour to maintain the mutual orthogonality

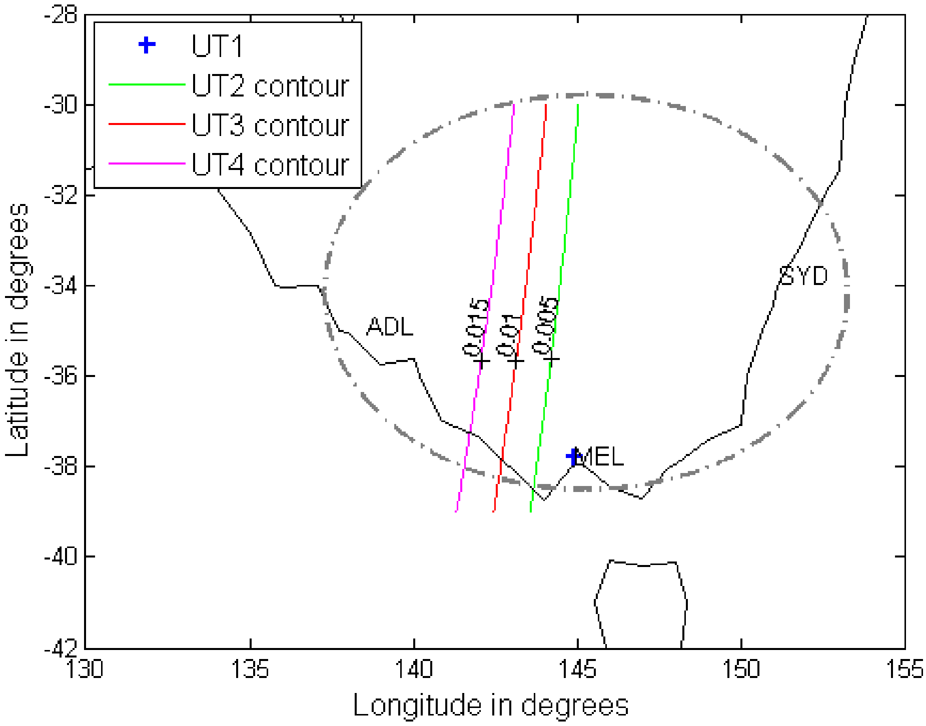


Figure 5.6: Location contours ($i = 1, l = 3$) at $f = 30$ GHz, $\mathrm{d_S} = 1$m, $\nu = 1$ and $\kappa_q = 0$

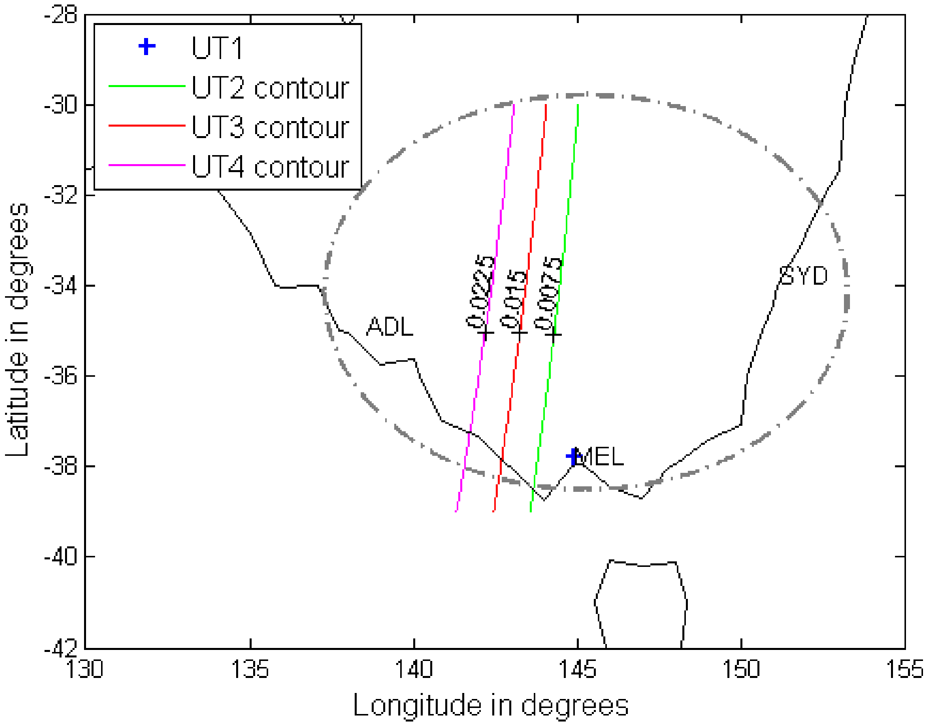


Figure 5.7: Location contours ($i = 1, l = 4$) at $f = 30$ GHz, $\mathrm{d_S} = 1$m, $\nu = 1$ and $\kappa_q = 0$

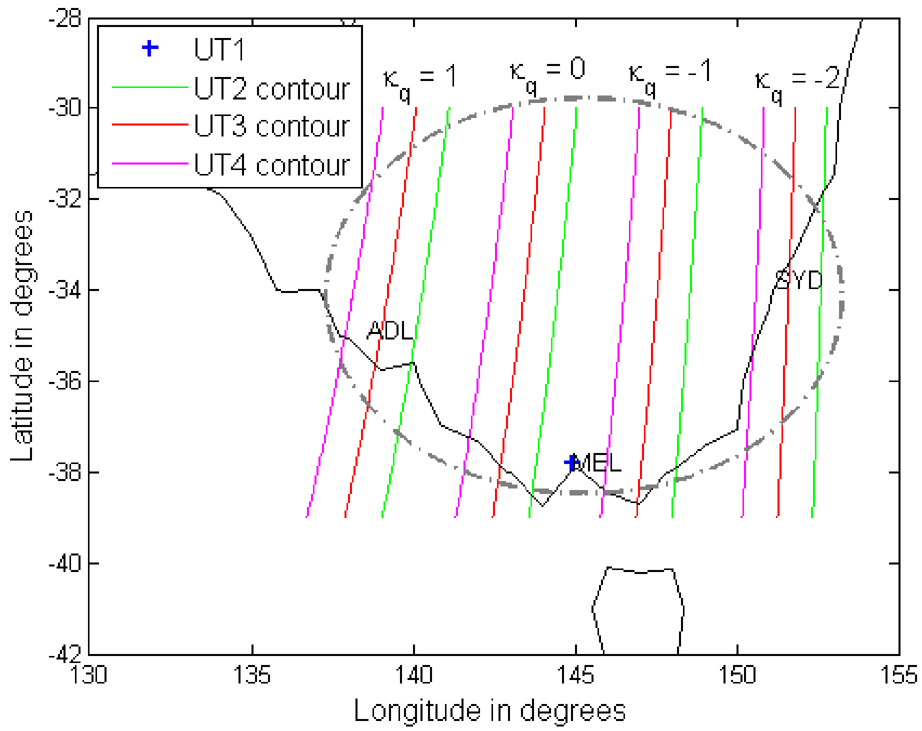


Figure 5.8: Location contours at $\nu = 1$, $f = 30$ GHz and $\mathrm{d_S} = 1$m

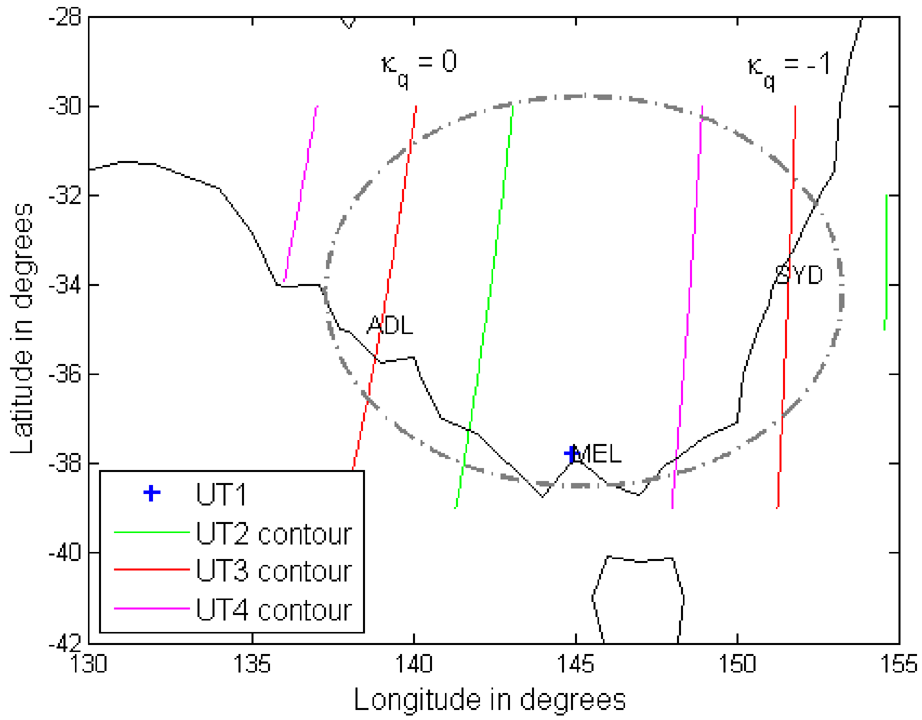


Figure 5.9: Location contours at $\nu = 3$, $f = 30$ GHz and $\mathrm{d_S} = 1$m

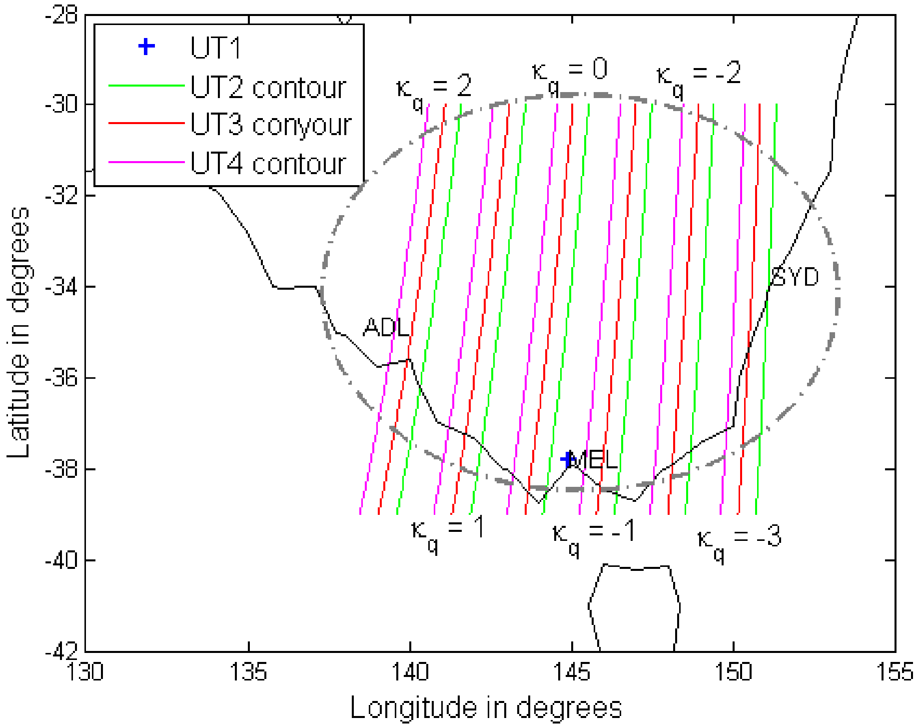


Figure 5.10: Location contours at $\nu = 1$, $f = 30$ GHz and $\mathrm{d_S} = 2$ m

that produce smaller spot beams. Interestingly, the high gain antennas are physically large and necessitate greater spacing.

## 5.3 Channel Capacity

The uplink performance of the MU-MIMO channel can be analysed in-terms of the overall sum spectral efficiency gain. The MU-MIMO channel capacity can be expressed in-terms of the SNR ($\rho$) and the channel matrix, where the single antenna multiple users are part of the channel matrix [5][6] :

$$C = \log_2 \det \left( I_M + \frac{\rho}{N} \widetilde{\mathbf{H}} \widetilde{\mathbf{H}}^{\dagger} \right) \quad \text{bits/s/Hz.} \tag{5.29}$$

In [5], the authors assume that the total uplink power in MU-MIMO is $N$ times greater compared to the single user MIMO. In a MU-MIMO scenario, it is more natural to

[6] Section-1.2 in [5]

have a total uplink power that increases with the number of users. However, in our analysis the total uplink power is a constant irrespective of the multiple users, hence the SNR is scaled by the number of users in (5.29). The reason for this SNR scaling is to show that the capacity increment is achieved purely from spatial degrees of freedom gain.

Figure 5.11 shows the channel capacity with respect to SNR and compares the performance of SISO with different MU-MIMO scenarios. In each MU-MIMO scenario, the users are assumed to be in spatially orthogonal locations and the channel matrix is fully orthogonal. For a fair comparison, in all the scenarios the sum transmit power is kept constant across the users. Significant performance increase can be noticed by using MU-MIMO. For example, a 12 dB improvement to achieve 4 bits/s/Hz from four orthogonal users compared to the SISO scenario.

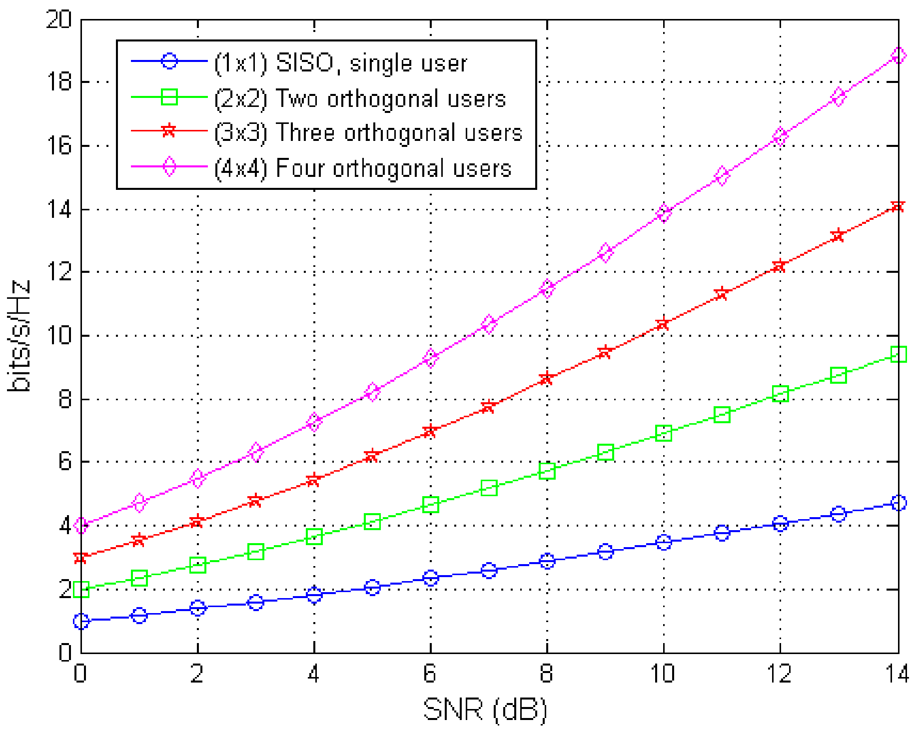


Figure 5.11: Channel capacity with respect to SNR (optimal orthogonal users)

Figure 5.12 shows the channel capacity with respect to $d_G$ at 10 dB SNR, where $d_G$ is the distance between each user on the ground when they are arranged along a line, with uniform spacing. Unlike the satellite antennas, the users are not required to be in a strict ULA configuration. However, the capacity achieved does degrade when the UT's are not ideally spaced. A linear arrangement is used initially to analyse the sensitivity in the inter-distance relationship between the users, this is expanded upon in Section-5.4 considering random locations.

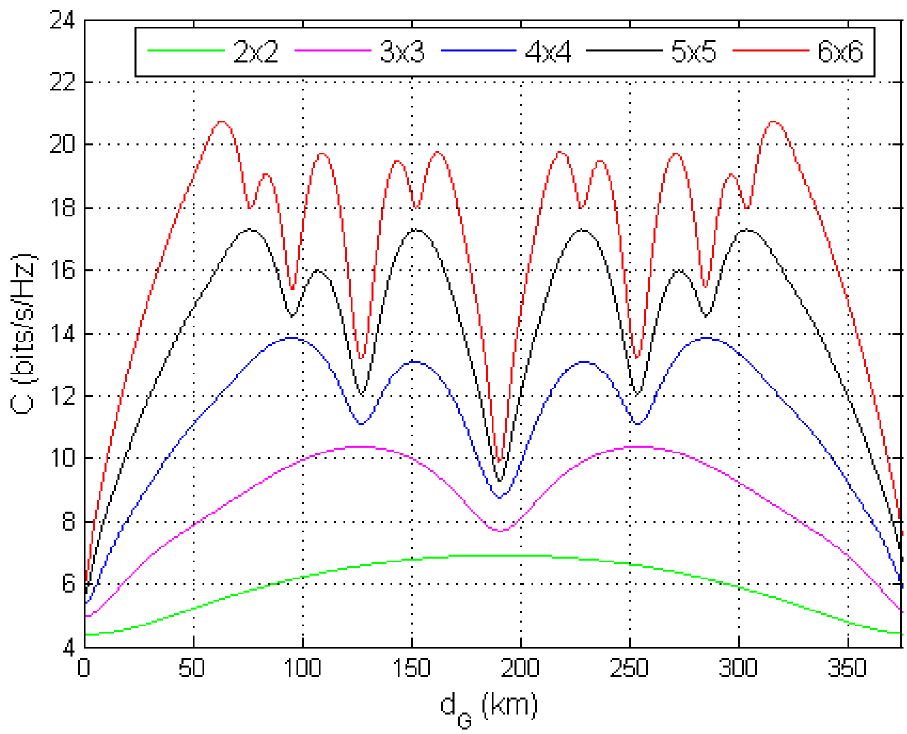


Figure 5.12: Channel capacity with respect to $d_G$ at 10 dB SNR and $d_S = 1$ m

In the $2 \times 2$ scenario, the optimal channel capacity is achieved when the minimum distance between the two users (at the same latitude) is approximately 190 km at $f = 30$ GHz. Similarly, for other MU-MIMO scenarios $3 \times 3$, $4 \times 4$, $5 \times 5$ and $6 \times 6$ the optimal channel capacity is achieved when the minimum distance between the users are 127 km, 95 km, 76 km and 64 km, respectively.

In the above case, it is assumed that $d_S = 1$ m in all the MU-MIMO scenarios. The channel capacity linearly increases with the number of satellite antennas and achievable users. As $M$ increases, the minimum distance requirement between the users decreases. However, the sensitivity due to non optimal $d_G$ increases along with the MU-MIMO order. This can be seen by the variations of capacity for each $M$ in Figure 5.12.

The channel capacity can also be expressed in terms of the channel singular values as in (2.23). The distribution of singular values is a measure of usefulness of different spatial paths in the channel.

## 5.4 Sub-optimal User Location

In an ideal case, the users would be at the optimal orthogonal positions. However, in practice this may not always be possible. The impact of sub-optimal user location is analysed in this section using Monte-Carlo simulation. For each user, let's consider a location square with uniform distribution from an optimal position $\mathcal{U}(-\Omega, +\Omega)$, where $\Omega$ denotes independent displacement angle in both latitude and longitude.

The simulation results are shown in Figure 5.13. Normalised mean capacity ($C/C_{\text{opt}}$) with respect to $\Omega$ at 10 dB SNR is shown in the top subplot, where $C_{\text{opt}}$ is the optimal capacity when each user in a $4 \times 4$ MU-MIMO architecture is in an optimal orthogonal position. The middle subplot shows the mean location error from all users with respect to $\Omega$. The bottom subplot shows the mean singular values, they are expected to be equal when the channel matrix is fully orthogonal.

The sensitivity due to sub-optimal user location increases with the number of satellite antennas. Figure 5.14 shows the mean normalised capacity for different MU-MIMO scenarios. The sensitivity increases with $M$, the mean capacity in each scenario asymptotes to specific value that also implies the mean capacity if the users are arbitrary grouped from a distributed user set. At worst case sub-optimal user locations, the mean achievable capacity of a MU-MIMO scenario is still significantly better in comparison to the conventional SISO scenario. For example, in a $4 \times 4$ scenario, the achievable mean capacity asymptotes to 80% capacity optimum. From Figure 5.11, numerically 80% of optimal capacity in a $4 \times 4$ scenario at 10 dB SNR is 11.2 bits/s/Hz as compared to around 1.8 bits/s/Hz in a SISO scenario.

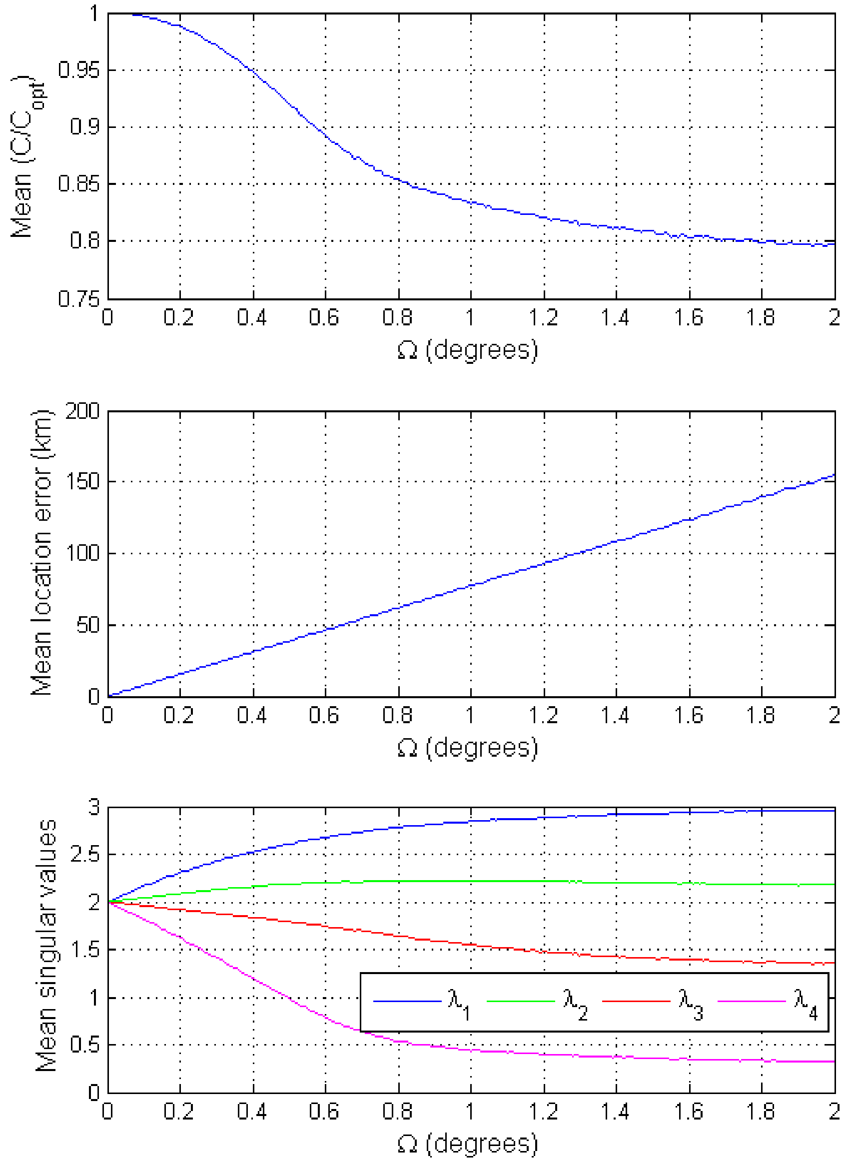


Figure 5.13: Sub-optimal user location analysis with respect to $\Omega$: (Top) Normalised mean capacity, (Middle) Mean location error and (Bottom) Singular values

## 5.5 BER Simulation

A Matlab based simulation framework was developed to analyse the communications performance of the channel in-terms of bit error rate (BER). A $4 \times 4$ uplink scenario is

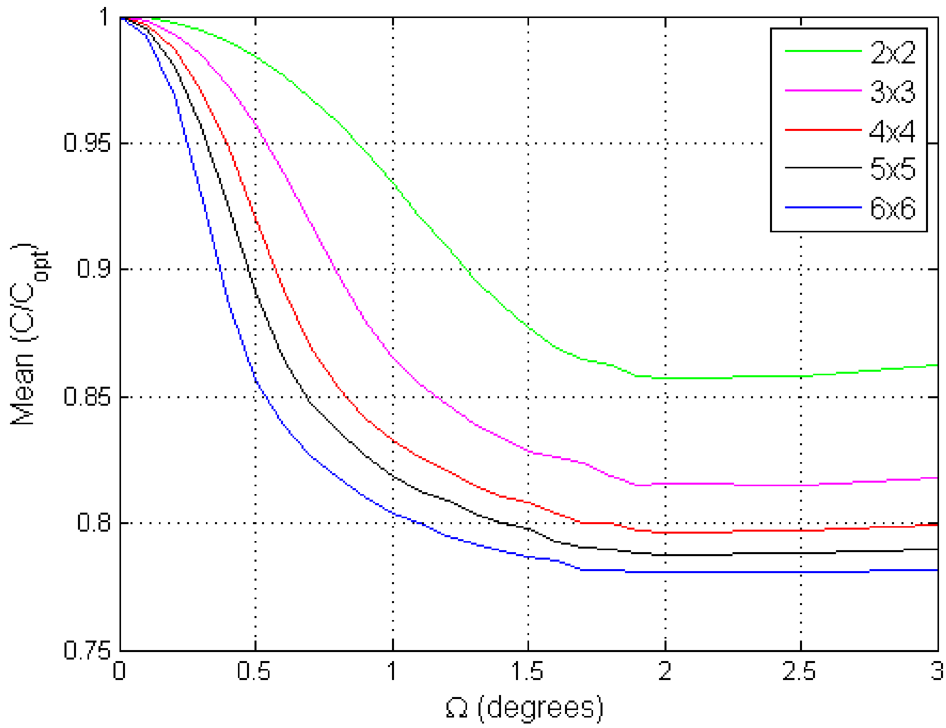


Figure 5.14: Normalised mean capacity, MU-MIMO architecture with users distributed randomly with respect to ideal locations

considered for analysis. Each UT independently transmits a symbol at the same time, the received signal at the satellite is given by:

$$\mathbf{y} = \mathbf{H}\mathbf{x} + \mathbf{w}, \tag{5.30}$$

where $\mathbf{x} \in \mathbb{C}^{N\times 1}$, $\mathbf{y} \in \mathbb{C}^{M\times 1}$ and $\mathbf{w} \sim \mathcal{CN}(0, \sigma^2\mathbf{I}_M)$ denote the transmitted signal, received signal and additive white Gaussian noise, respectively, at a symbol time (the time index is omitted for simplicity) and $\sigma^2$ is the noise variance at each receive antenna. The analysis is undertaken with two popular types of linear MIMO decoding receivers: One is based on the Zero-Forcing (ZF) filter and the other is based on the Minimum Mean Square Error (MMSE) filter.

$$\widetilde{\mathbf{y}} = \mathbf{G}\mathbf{y}, \tag{5.31}$$

where $\widetilde{\mathbf{y}}$ denotes the received estimates of the transmitted symbols and $\mathbf{G}$ denotes a linear MIMO decoding filter based on either ZF or MMSE equalisation methods. The filter performs a linear separation of each individual user signal from the combined received signals. In the ZF case, the filter is computed as below:

$$\mathbf{G}_{\mathrm{ZF}} = (\widetilde{\mathbf{H}}^{\dagger}\widetilde{\mathbf{H}})^{-1}\widetilde{\mathbf{H}}^{\dagger}. \tag{5.32}$$

The ZF filter completely eliminates other user signals in each user stream. However, a known drawback of using ZF is the amplification of the noise component that arises from the modification of the noise covariance matrix.

An alternative linear receiver design is based on the minimization of the mean square error. In the MMSE case, the preprocessing filter is computed as follows:

$$\mathbf{G}_{\mathrm{MMSE}} = (\widetilde{\mathbf{H}}^{\dagger}\widetilde{\mathbf{H}} + \Sigma_w)^{-1}\widetilde{\mathbf{H}}^{\dagger}, \tag{5.33}$$

where $\Sigma_w = \sigma_w^2\mathbf{I}_M$ denotes noise covariance matrix. In both cases, it is assumed that the channel state information is available and $\mathbf{H}$ is perfectly known at the receiver. This is a realistic assumption, where it is expected that the orthogonal users are grouped based on a-priori location knowledge. The simulation also assumes perfect synchronisation at the receiver for carrier phase and symbol timing recovery.

Each UT transmits an uncoded QPSK waveform. The combined BER performance for all four users is shown in Figure 5.15. Although for simplicity reason the signal formation is given as a complex baseband example, the actual signal processing in simulation includes oversampling at four samples per symbol and independent known frequency offset from each UT. Results for three different user location scenarios are plotted in Figure 5.15 and in each scenario the effect of the ZF and MMSE preprocessing filters are compared. In a $4 \times 4$ MIMO scenario, the optimal spacing between each user is approximately 95 km from Figure 5.12. The three different user location scenarios are analysed with different ($\mathrm{d_G}$) values, corresponding to 95, 85 and 75 kilometres, respectively. The corresponding channel singular values are given in Table 5.3.

The BER performance in Figure 5.15 is optimum as expected at $\mathrm{d_G} = 95$ km, when the users are in optimal orthogonal locations. The communications performance deteriorates when the users are not in orthogonal locations, at $\mathrm{d_G} = 85$ km and 75 km.

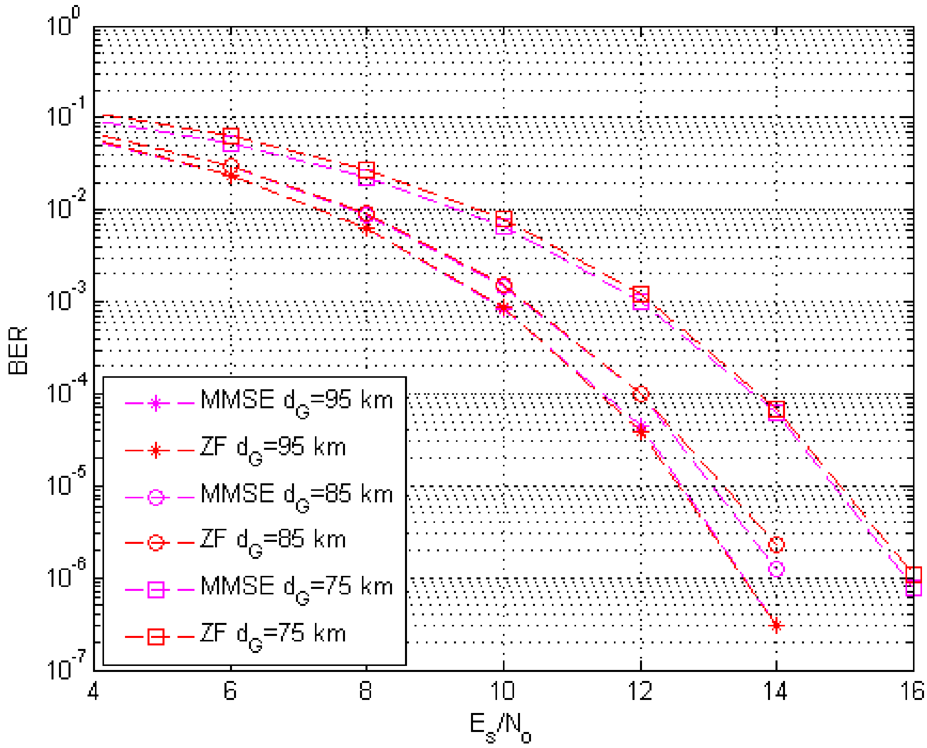


Figure 5.15: BER for $4 \times 4$ MIMO scenario with QPSK and no coding

Table 5.3: Channel singular values ($4 \times 4$ MIMO channel analysis)

| $d_G$ (km) | $\lambda_1$ | $\lambda_2$ | $\lambda_3$ | $\lambda_4$ |
|---|---|---|---|---|
| 95 | 2.01 | 2.00 | 2.00 | 1.99 |
| 85 | 2.24 | 2.12 | 2.10 | 1.45 |
| 75 | 2.25 | 2.25 | 2.22 | 0.95 |

Since the operating SNR was high, there's no visible performance improvement gained by using MMSE over ZF preprocessing filter.

In Figure 5.16, BER results are shown with LDPC channel coding at 0.5 code rate and QPSK modulation. The LDPC code structure is according to DVB-S2 standard, with frame length of 64,800 bits [47]. The combined spectral efficiency from four users is 4 bits/s/Hz. From Figure 5.11 $4 \times 4$ MIMO scenario, the achievable capacity without signal set constraints at 0 dB SNR is 4 bits/s/Hz. The simulation results in Figure 5.16 with MMSE filter at $d_G$ = 95 km matches the BER performance at approximately 1 dB SNR. For the chosen coding and modulation, according to [47], the ideal SNR is approximately 1 dB to achieve a BER of $10^{-7}$.

In all three user location scenarios, due to the low operating SNR, the MMSE receiver performance is better compared to the ZF based receiver. The MMSE performance is significantly better at $d_G$ = 75 km. However, neither MMSE nor ZF are optimum receivers. MMSE with successive interference cancellation (SIC) MMSE-SIC receivers should achieve the best possible sum capacity for any given channel matrix [27].

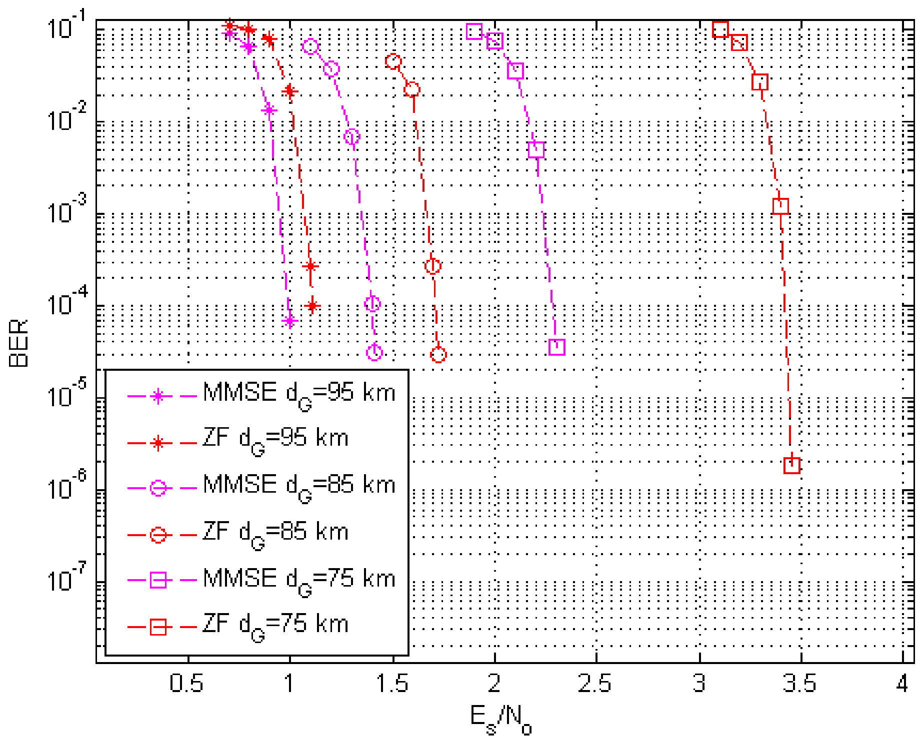


Figure 5.16: BER for 4 × 4 MIMO with QPSK and LDPC (code rate = 0.5)

## 5.6 Chapter Review

A MU-MIMO spatial multiplexing technique is proposed in this chapter for single satellite systems to benefit from MIMO. MU-MIMO provides a capacity enhancement framework to increase the throughput of a High Capacity Satellite (HiCapS) system in a given geographical region. WGS is an example of HiCapS system with multiple spot beam antennas, so using MU-MIMO the capacity of a satellite similar to WGS can be increased using overlapping spot beams on the same frequency plan. It is shown that the channel spectral efficiency can be linearly increased in a given region by using multiple antennas at the satellite, overlapping the beams and adopting a MU-MIMO spatial multiplexing architecture. However, the channel state information is required at the satellite or the anchor station to implement MIMO decoding and precoding for user side uplink and downlink, respectively. Although this method may draw some parallels with other antenna beamforming and null steering techniques [58], the MU-MIMO approach allows easy evaluation of the capacity when the users are not orthogonal.

# Chapter 6

# Channel Measurement: Passive Experimental Campaigns

SATCOM links using geostationary satellites rely heavily on the line-of-sight (LOS) path to achieve a healthy link budget. Despite the LOS nature of the channel, in Chapter-3 and Chapter-5, it was shown that MIMO spatial multiplexing is achievable either using multiple satellites or with a single satellite (with multiple antennas) respectively. It has been established that to obtain an orthogonal MIMO channel matrix in a LOS dominated channel, a distinct phase relationship is required in the channel matrix and that this is achieved through geometrical optimisation method for antenna spatial separation and placement [19]. The theoretical framework explained in Chapter-2 shows that a large antenna separation distance is required, either in space or on the ground. For MIMO SATCOM to be validated, it is imperative that the theoretical concepts are proven by channel measurements

In this chapter, a novel passive measurement technique is presented to measure MIMO SATCOM channel orthogonality. The technique uses downlinks from two satellites that have overlapping frequency coverage and beam footprints. Differential phase measurements are obtained using cross-correlation analysis. These phase measurements are subsequently used to verify the orthogonality of the MIMO channel matrix. Accuracy analysis of the measurement method is also presented in this chapter, together with simulated and measured results.

Two independent, passive channel measurement campaigns have been successfully conducted, one in Ku-band and another in X-band. The Ku-band experiment was conducted in Munich during November 2015 in collaboration with the Munich University of Bundeswehr[1]. The Ku-band experiment was conducted using two EUTELSAT satellites, 7B and 10A in geostationary orbit at 7°E and 10°E respectively. The X-band measurement was conducted during October 2016 at the Defence Science and Technology Group, Edinburgh, South Australia. The second measurement campaign provided channel measurement results using a WGS satellite and a SKYNET satellite in 88.4°E and 95.2°E respectively [59]. The results from both the measurement campaigns were successful and show very close agreement with the theoretical framework for MIMO SATCOM.

## 6.1 Measurement Setup

The downlink MIMO channel matrix under measurement is denoted by $\mathbf{H} \in \mathbb{C}^{Z \times M}$, where $M$ is the number of satellites and $Z$ denotes the number of receive antennas on the ground. In this case the channel is represented by a $2 \times 2$ matrix:

$$\mathbf{H} = \begin{bmatrix} h_{11} & h_{12} \\ h_{21} & h_{22} \end{bmatrix}. \tag{6.1}$$

Each channel path element $h_{zm}$ (2.2) is a complex coefficient with a channel path attenuation and a deterministic channel phase $\phi_{zm}$:

$$h_{zm} = |h_{zm}|e^{-j\phi_{zm}} \qquad z, m \in \{1, 2\}, \tag{6.2}$$

$$\phi_{zm} = 2\pi \frac{f}{c} r_{zm}, \tag{6.3}$$

[1]While the researchers at the Munich university had developed a measurement technique based on active transmission to the satellites, as reported in [31]; the passive measurement technique discussed in this chapter was fully developed and tested by the author.

The information capacity of a MIMO channel is given in (2.13). However, in this case there are $M$ antennas in space and $Z$ receive antennas at the source, hence the capacity $C$ is given by:

$$C = \log_2 \det \left( I_Z + \frac{S}{M\sigma_w^2} \mathbf{H}\mathbf{H}^\dagger \right) \qquad \text{bits/s/Hz}, \tag{6.4}$$

The channel is said to be fully orthogonal if the matrix product $\mathbf{H}\mathbf{H}^\dagger$ results in a diagonal matrix. The required condition to achieve the channel orthogonality is given in (2.9). Dependent on the wavelength, specific antenna spacing is required to satisfy (2.9). It is shown in Chapter-2 that either the antennas on the ground must be separated by tens of kilometres to accommodate the small antenna separation on a single satellite or multiple satellites are required to enable closer antenna placement on the ground.

In the channel measurement campaigns, the latter case is considered with two satellites. The passive measurement setup is shown in Figure 6.1. The two large antennas $\mathrm{v}_1$ and $\mathrm{v}_2$ have narrow antenna beamwidth. They are pointed directly to the satellites $\mathrm{s}_1$ and $\mathrm{s}_2$, respectively. The two small antennas $\mathrm{y}_1$ and $\mathrm{y}_2$ have broad beamwidths and each of them is pointed to the mid-point between the two satellites; this forms a $2\times 2$ MIMO channel between the two small antennas on the ground and the satellites in space. All four receive antennas in the measurement setup are co-located at the same site.

The aim of the measurement setup is to measure the phase relationship ($\psi$) of the channel matrix.

$$\psi = (\phi_{11} - \phi_{21}) - (\phi_{12} - \phi_{22}). \tag{6.5}$$

The channel is fully orthogonal when $\psi = \pm\pi$, whereas $\psi = 0$ denotes a keyhole channel [2] [61]. In the setup for Ku-band experiments, the expected phase relationship (6.5) and channel capacity (6.4) with respect to $\mathrm{d_G}$ is shown in Figure 6.2. The expected results are based at $f$ = 12.5 GHz, where the two EUTELSAT satellites were located at 10°E and 7°E and the ground antennas were located at 48.08°N and 11.64°E and oriented at $\delta_\mathrm{G} = -20.6^\circ$ with respect to the local East-West direction. Maximum

[2] In MIMO literature, the term keyhole is used to indicate the channel environment where the channel capacity of the MIMO system becomes very low [60]

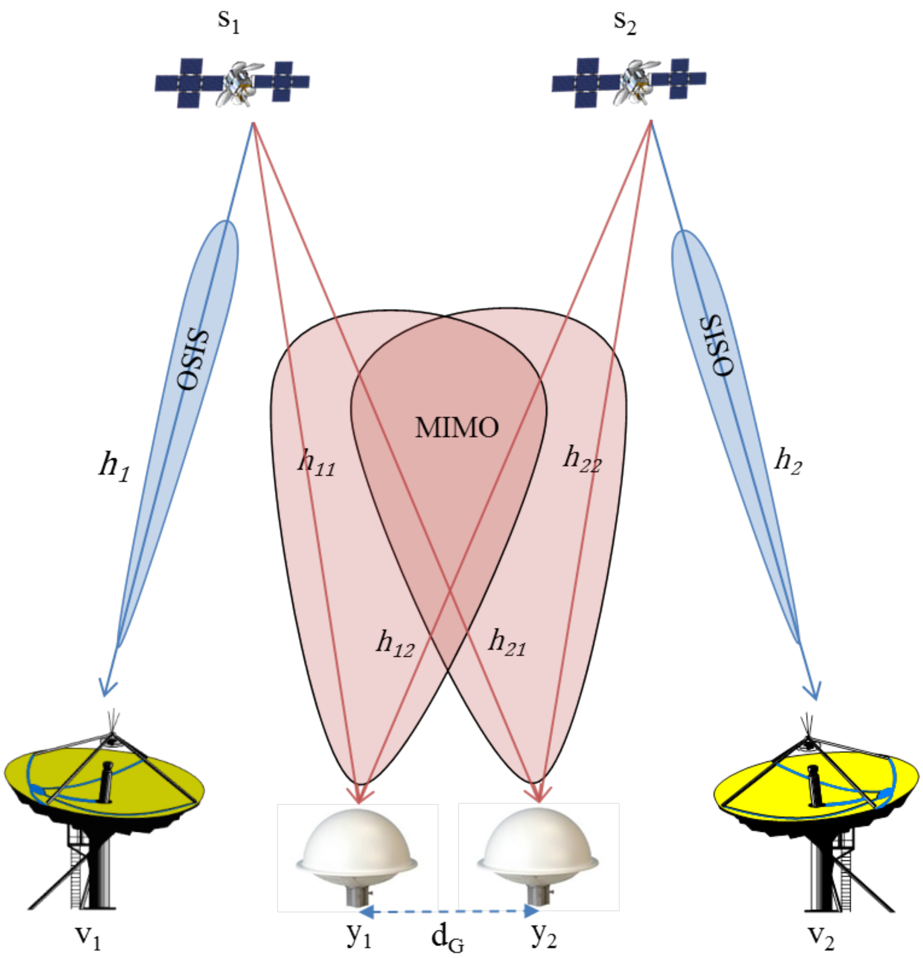


Figure 6.1: Experimental setup for passive channel orthogonality measurement technique for MIMO SATCOM (no uplink, downlink only)

channel capacity is achieved at values of $\mathrm{d_G}$ where $|\psi| = \pi$. The periodicity of maxima points corresponds to $\nu = 1, 3, ...$ in (2.9).

Similarly, the expected results for the X-band setup are shown in Figure 6.3. The expected results are based on the parameters: $f = 7.645$ GHz, where the two geostationary satellites are located at 88.4°E and 95.2°E and the ground antennas are located at 34.9°S and 138.648°E oriented at $\delta_{\mathrm{G}} = -90^{\mathrm{o}}$ with respect to the local East-West direction.

The optimal location contours for the second antenna $\mathrm{y}_2$, calculated based on (2.9), are shown in Figure 6.4 and Figure 6.5 in Ku-band and X-band, respectively. The horizontal and vertical axes in these figures represents the relative longitude and relative

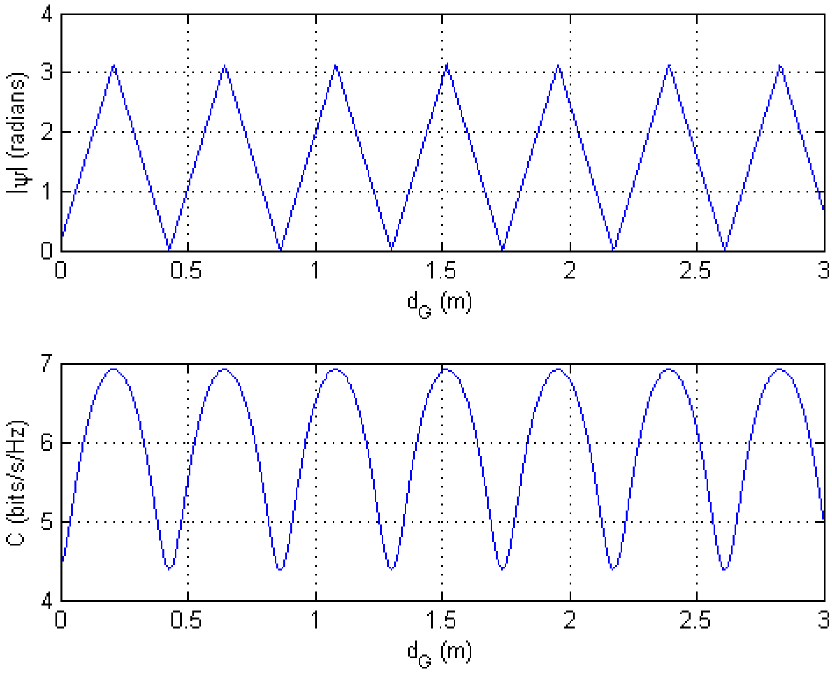


Figure 6.2: Expected result for Ku-band setup:(top) $|\psi|$ verses $d_G$, (bottom) capacity verses $d_G$ at SNR=10dB,

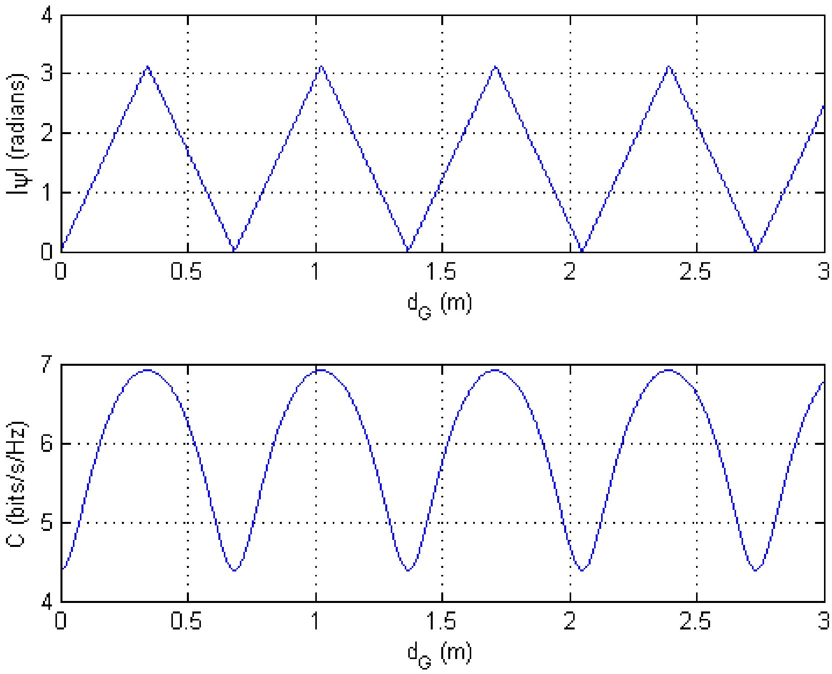


Figure 6.3: Expected result for X-band setup:(top) $|\psi|$ verses $d_G$, (bottom) capacity verses $d_G$ at SNR=10dB,

latitude with respect to the $y_1$ position, respectively. The main aim of the measurement campaigns was to measure the phase relationship in the channel and compare to the theoretically calculated results. In both measurement campaigns, the antenna $y_2$ was placed on a movable rail and moved away from $y_1$ to measure the channel phase under different $d_G$ values.

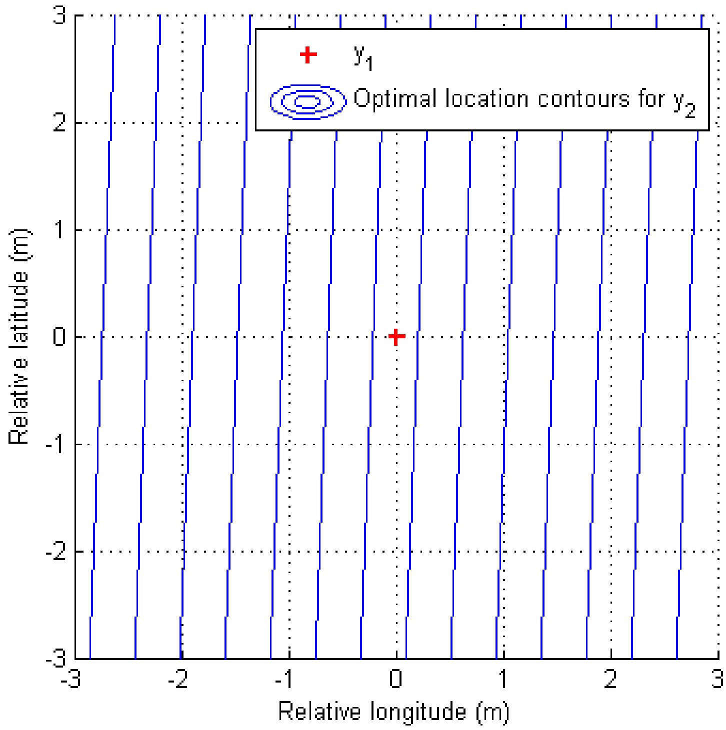


Figure 6.4: Optimum location contours for $y_2$ in Ku-band experiment

## 6.2 Passive Measurement Technique

Let $y_1$ and $y_2$ be the received signals through the MIMO channel and $v_1$ and $v_2$ be the received signals in the SISO channel

$$\begin{bmatrix} y_1 \\ y_2 \end{bmatrix} = \mathbf{H} \begin{bmatrix} s_1 \\ s_2 \end{bmatrix} + \begin{bmatrix} w_{y,1} \\ w_{y,2} \end{bmatrix}, \tag{6.6}$$

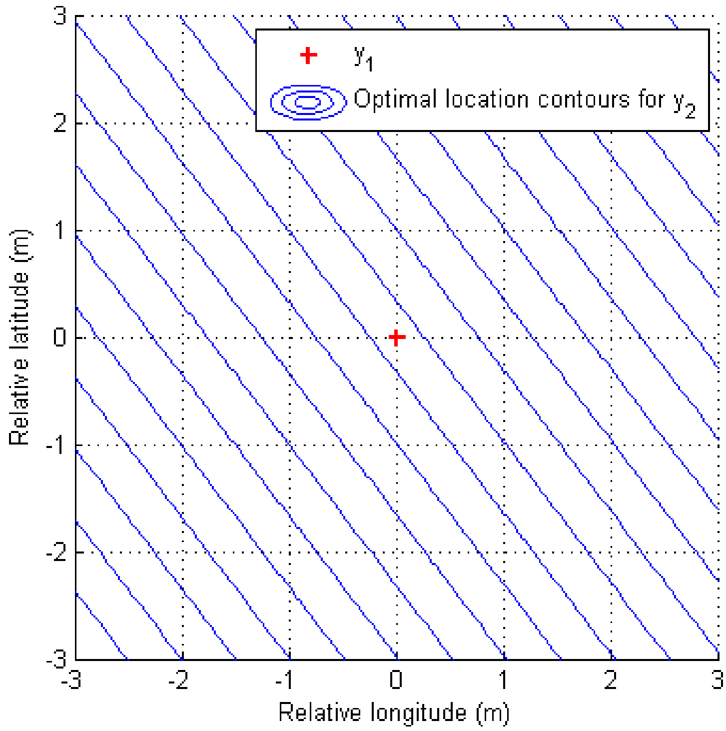


Figure 6.5: Optimum location contours for $\mathrm{y}_2$ in X-band experiment

$$\begin{bmatrix} v_1 \\ v_2 \end{bmatrix} = \mathbf{J} \begin{bmatrix} s_1 \\ s_2 \end{bmatrix} + \begin{bmatrix} w_{v,1} \\ w_{v,2} \end{bmatrix}, \tag{6.7}$$

where $s_1$ and $s_2$ are respective satellite downlink signals in a specified bandwidth, $w_{y,1}$, $w_{y,2}$, $w_{v,1}$ and $w_{v,2}$ are statistically independent receiver noises and $\mathbf{J} \in \mathbb{C}^{M \times M}$ is channel matrix between the satellites and the large antennas and $\mathbf{H}$ as in (6.1). In this case, $\mathbf{J}$ is a $2 \times 2$ matrix, the diagonal elements of $\mathbf{J}$ denote the SISO channel paths $h_1$ and $h_2$, respectively, and the off-diagonal elements $\alpha_1$ and $\alpha_2$ are respective antenna discrimination coefficients in the direction of the alternate satellite, where $|h_m| >> |\alpha_m|$:

$$\mathbf{J} = \begin{bmatrix} h_1 & \alpha_1 \\ \alpha_2 & h_2 \end{bmatrix}, \tag{6.8}$$

$$h_m = |h_m| e^{-j\phi_m} \qquad m \in \{1, 2\}. \tag{6.9}$$

Let $R_{yv,zm}$ denote the cross-correlation coefficient between the MIMO receive antenna $y_z$ and SISO receive antenna $v_m$ at zero time lag

$$R_{yv,zm} = \quad < y_z(t)v_m^*(t) > \qquad z, m \in \{1, 2\}, \tag{6.10}$$

$$= \frac{1}{T} \int_{-T/2}^{T/2} y_z(t)v_m^*(t)dt, \tag{6.11}$$

where $< . >$ denotes time averaging operation and $T$ is signal integration time. It is assumed that $s_1$ and $s_2$ are fully uncorrelated and there are no other significant signal sources from the direction of the two satellites at overlapping frequencies, which is a reasonable assumption due to the strict frequency coordination in the geo-stationary orbit. In an ideal case, when $|\alpha_m| = 0$, the cross-correlation function at zero time lag is given by:

$$R_{yv,zm} = h_{zm}h_m^*\sigma_{s_m}^2 \qquad z, m \in \{1, 2\}, \tag{6.12}$$

where $\sigma_{s_1}^2$ and $\sigma_{s_2}^2$ denote signal power of $s_1$ and $s_2$, respectively. Using (6.6), (6.7), the expected value of the cross-correlation between the received signals can be expressed in a matrix form:

$$\mathbb{E}\left(\begin{bmatrix} y_1 \\ y_2 \end{bmatrix}\begin{bmatrix} v_1 \\ v_2 \end{bmatrix}^\dagger\right) = \begin{bmatrix} R_{yv,11} & R_{yv,12} \\ R_{yv,21} & R_{yv,22} \end{bmatrix}$$

$$= \mathbf{H}\begin{bmatrix} \sigma_{s_1}^2 & 0 \\ 0 & \sigma_{s_2}^2 \end{bmatrix}\mathbf{J}^\dagger, \tag{6.13}$$

The argument of each correlation coefficient gives a differential phase estimate $(\widehat{\phi}_{zm})$:

$$\widehat{\phi}_{zm} = \arg\{R_{yv,zm}\} \approx \phi_{zm} - \phi_m. \tag{6.14}$$

These differential phase estimates are used to estimate the phase relationship in the channel matrix ($\widehat{\psi}$)

$$\begin{aligned}\widehat{\psi} &= (\widehat{\phi}_{11} - \widehat{\phi}_{12}) - (\widehat{\phi}_{21} - \widehat{\phi}_{22}) \\ &\approx (\phi_{11} - \phi_{12}) - (\phi_{21} - \phi_{22}).\end{aligned} \tag{6.15}$$

For the correlation process to work, all the receivers must be frequency locked to a common reference source and the signals captured at the same centre frequency on all of the four receive channels. However, each receiver may have its own phase noise, but the phase noise from each receiver cancels in equation (6.15). The passive channel measurement technique is a simple, yet a powerful solution to accurately measure the orthogonality of a MIMO SATCOM channel.

## 6.3 Accuracy Analysis

The standard deviation of the differential phase estimate is analysed in this section. The accuracy of the phase estimate from each correlation is dependent on the post correlation SNR. The cross-correlation and auto-correlation of the received signals can be related by Schwarz's inequality [62]

$$|R_{yv,zm}|^2 \leq R_{yy,z} R_{vv,m} \qquad \{z, m = 1, 2\}, \tag{6.16}$$

where $R_{yy}$ and $R_{vv}$ denote the auto-correlation values at zero time lag:

$$R_{yy,z} =< y_z(t) y_z^*(t) > \qquad \{z = 1, 2\}, \tag{6.17}$$

$$R_{vv,m} =< v_m(t) v_m^*(t) > \qquad \{m = 1, 2\}. \tag{6.18}$$

$$\mathbf{C}_{yv,zm} = \frac{|R_{yv,zm}|^2}{R_{yy,z} R_{vv,m}} \qquad \{z, m = 1, 2\}, \tag{6.19}$$

where the coherency function $0 \leq \mathbf{C}_{yv,zm} \leq 1$ is a measure of correlation between the two received signals $y_z$ and $v_m$ and $\mathbf{C}_{yv,zm} = 1$ indicates full correlation. The standard deviation of the phase estimate can be approximated by [63]

$$\sigma_{\phi_{zm}} \approx \sin^{-1}\left[\frac{1-\mathbf{C}_{yv,zm}}{2\mathrm{N_s}\mathbf{C}_{yv,zm}}\right]^{1/2}, \tag{6.20}$$

where $\mathrm{N_s}$ denotes the number of discrete samples. Since the local noise at the receivers is statistically independent, the variance for the overall channel phase estimate will be the sum of the variance of all individual phase estimates. Hence, the corresponding standard deviation in estimating the phase of the channel matrix is given as:

$$\sigma_{\psi} = \sqrt{\sum_{z}^{2}\sum_{m}^{2}\sigma^2_{\phi_{zm}}}. \tag{6.21}$$

In Figure 6.6, under different SNR values, the comparison between theoretically estimated $\sigma_{\psi}$ and simulation is shown. Approximately equal SISO SNRs are assumed at receivers $\mathrm{v_1}$ and $\mathrm{v_2}$. The simulation framework is executed with $\mathrm{N_s} = 10^5$ samples in each receiver and 1000 iterations to calculate the standard deviation. In each iteration, random phase values in the range from 0 to $2\pi$ are chosen for elements in the $\mathbf{H}$ and $\mathbf{J}$ matrices. The magnitude values of the matrices are unit normalized and $\alpha_1 = \alpha_2 = 0$. The SNRs at $\mathrm{y_1}$ and $\mathrm{y_2}$ will be significantly less compared to the SISO case, because of the smaller antenna size and gain. Two different cases are analysed in Figure 6.6; case-1 and case-2, where the MIMO SNRs are 12 dB and 22 dB less than the SISO SNRs, respectively. For the SNR values considered, the simulation closely agrees with theoretically estimated $\sigma_{\psi}$ (6.21).

### 6.3.1 Phase estimation bias

In the ideal case, it is assumed that $|\alpha| = 0$. However, in practice each SISO antenna receives a weak signal from the alternate satellite due to non-ideal antenna discrimination, such that $|\alpha| > 0$. This may introduce a phase bias in the channel orthogonality

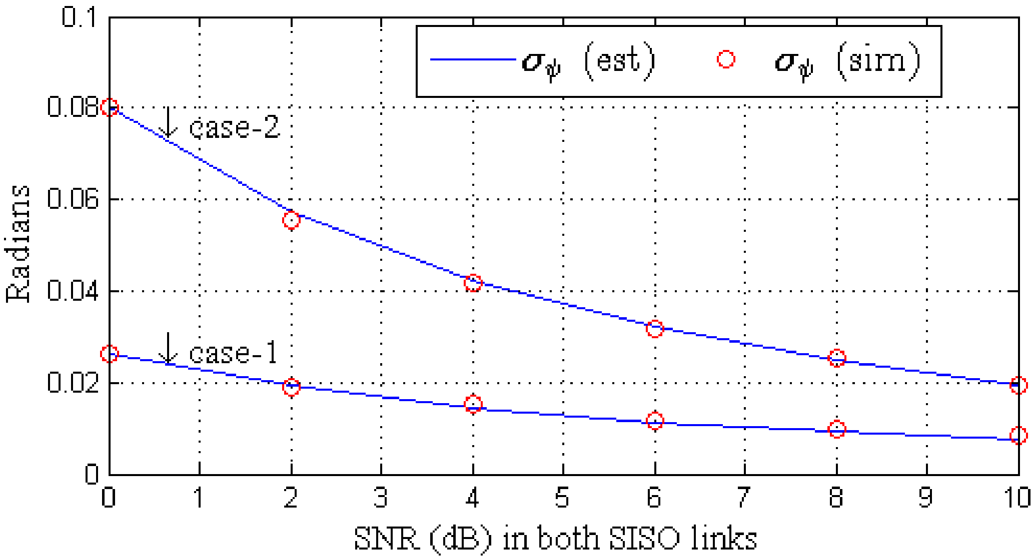


Figure 6.6: Comparison between theoretically estimated $\sigma_\psi$ and simulation

estimation process. By expanding (6.13):

$$R_{yv,11} = h_{11}h_1^*\sigma_{s_1}^2 + h_{12}\alpha_1^*\sigma_{s_2}^2. \tag{6.22}$$

To analyse the bias, let's define variables[3] $a = |h_{11}h_1|\sigma_{s_1}^2$, $b = |h_{12}\alpha_1|\sigma_{s_2}^2$, $\theta_a = \angle h_{11}h_1^*$ and $\theta_b = \angle h_{12}\alpha_1^*$. Such that:

$$R_{yv,11} = a(\cos\theta_a + j\sin\theta_a) + b(\cos\theta_b + j\sin\theta_b), \tag{6.23}$$

$$\tan\widetilde{\phi}_{11} = \frac{a\sin\theta_a + b\sin\theta_b}{a\cos\theta_a + b\cos\theta_b}, \tag{6.24}$$

$$\tan\widehat{\phi}_{11} = \frac{\sin\theta_a}{\cos\theta_a}, \tag{6.25}$$

where $\widetilde{\phi}_{11}$ and $\widehat{\phi}_{11}$ are the biased and unbiased phase estimates of the correlation function. Although it is not directly possibly to estimate $\widehat{\phi}_{11}$ without the bias, it is

[3]Since these local variables are used only in this section, they are not listed in the notation

useful to analyse the parameters that cause the phase error ($\phi_{e,11} = \widehat{\phi}_{11} - \widetilde{\phi}_{11}$):

$$\begin{aligned} \tan \phi_{e,11} &= \tan(\widehat{\phi}_{11} - \widetilde{\phi}_{11}) \\ &= \frac{\tan \widehat{\phi}_{11} - \tan \widetilde{\phi}_{11}}{1 + \tan \widehat{\phi}_{11} \tan \widetilde{\phi}_{11}}, \end{aligned} \tag{6.26}$$

where,

$$\begin{aligned} \tan \widehat{\phi}_{11} - \tan \widetilde{\phi}_{11} &= \frac{\sin \theta_a}{\cos \theta_a} - \left( \frac{a \sin \theta_a + b \sin \theta_b}{a \cos \theta_a + b \cos \theta_b} \right) \\ &= \frac{a \cos \theta_a \sin \theta_a + b \sin \theta_a \cos \theta_b - a \cos \theta_a \sin \theta_a - b \cos \theta_a \sin \theta_b}{a \cos^2 \theta_a + b \cos \theta_a \cos \theta_b} \\ &= \frac{b \sin(\theta_a - \theta_b)}{a \cos^2 \theta_a + b \cos \theta_a \cos \theta_b} \end{aligned} \tag{6.27}$$

and

$$\begin{aligned} 1 + \tan \widehat{\phi}_{11} \tan \widetilde{\phi}_{11} &= 1 + \frac{\sin \theta_a}{\cos \theta_a} \left( \frac{a \sin \theta_a + b \sin \theta_b}{a \cos \theta_a + b \cos \theta_b} \right) \\ &= \frac{a \cos^2 \theta_a + b \cos \theta_a \cos \theta_b + a \sin^2 \theta_a + b \sin \theta_a \sin \theta_b}{a \cos^2 \theta_a + b \cos \theta_a \cos \theta_b} \\ &= \frac{a + b \cos(\theta_a - \theta_b)}{a \cos^2 \theta_a + b \cos \theta_a \cos \theta_b}. \end{aligned} \tag{6.28}$$

After substituting (6.27) and (6.28) in (6.26):

$$\phi_{e,11} = \tan^{-1} \left[ \frac{\chi \sin(\theta_a - \theta_b)}{1 + \chi \cos(\theta_a - \theta_b)} \right], \tag{6.29}$$

where, $\chi = \frac{b}{a}$, since $|h_{11}| \approx |h_{12}|$, the $\chi$ factor is directly proportional to the product of the SISO antenna discrimination ($|\alpha|$) and signal power difference between the two satellite signals. Similarly $\phi_{e,zm}$ can be analysed for all values of $\{z, m = 1, 2\}$

$$\psi_e = (\phi_{e,11} - \phi_{e,12}) - (\phi_{e,21} - \phi_{e,22}), \tag{6.30}$$

where $\psi_e$ denotes the overall phase error in the channel orthogonality estimation process. The impact of the phase bias is shown in Figure 6.7, where antenna discrimination for both SISO antennas are -30 dB and with equal signal power from both satellite signals. Theoretically predicated channel orthogonality (red solid line) from (6.5), estimated impact of phase bias from (6.30) and (6.5) and simulation results are shown with respect to $d_G$. The biased phase of the channel matrix is denoted by $\widetilde{\psi}$

$$\widetilde{\psi} = \widehat{\psi} - \psi_e. \tag{6.31}$$

A small phase bias can be seen in Figure 6.7 due to the -30 dB SISO antenna discrimination. A poorer antenna discrimination between $v_1$ and $v_2$ will increase the phase bias, as shown in Figure 6.8 for -18 dB SISO antenna discrimination.

There appears to be least phase bias, when the antennas $v_1$ and $v_2$ are placed in a position where the channel **J** is fully orthogonal. However, further analysis of this approach is required and this is outside the scope of this thesis. This approach could be useful at lower frequency bands, for example at UHF band, where antenna discrimination can be significantly low compared to X-band or Ku-band.

Figure 6.9 shows the estimated and simulated outcome with -30 dB SISO antenna discrimination and 10 dB signal power difference in the satellite signals. The impact of the phase bias is greater as expected, which highlights the need to have approximately equal signal power level from both the satellites for accurate channel orthogonality measurement.

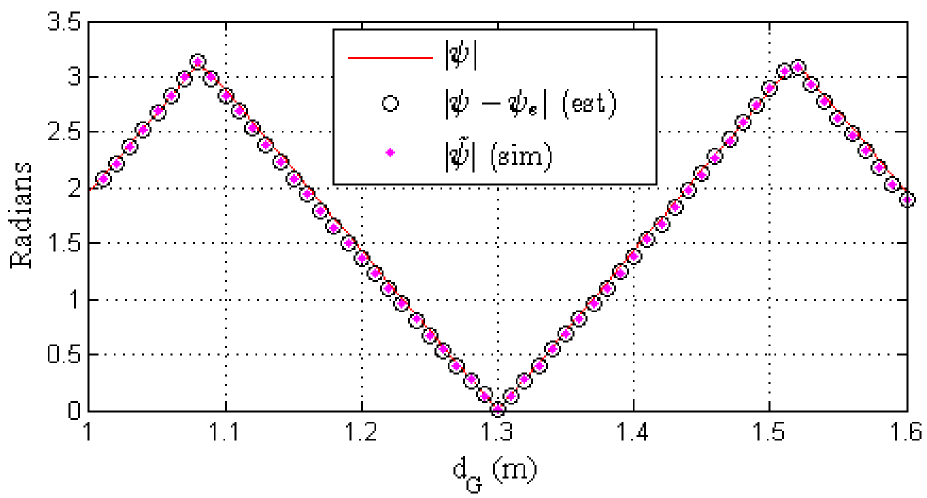


Figure 6.7: At -30 dB SISO antenna discrimination and $\sigma^2_{s_1} = \sigma^2_{s_2}$

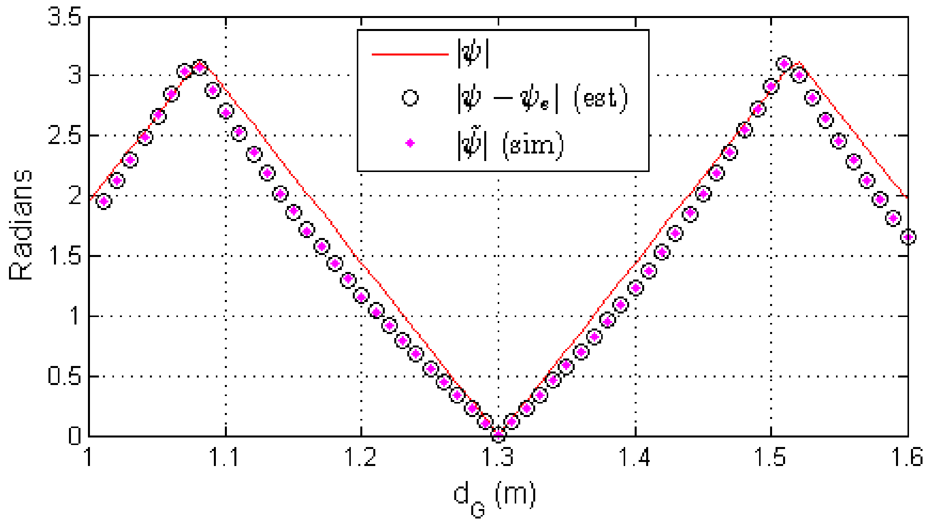


Figure 6.8: At -18 dB SISO antenna discrimination and $\sigma_{s_1}^2 = \sigma_{s_2}^2$

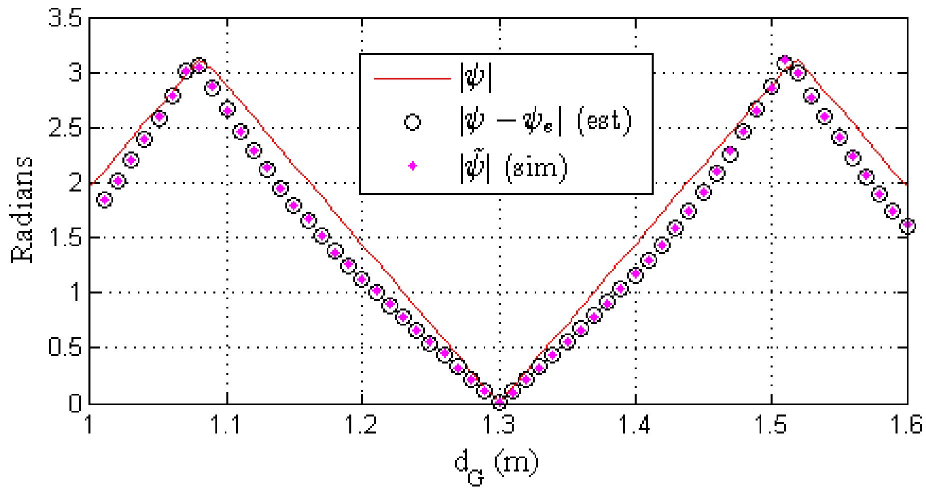


Figure 6.9: At -30 dB SISO antenna discrimination and $\sigma_{s_1}^2 = \frac{\sigma_{s_2}^2}{10}$

## 6.4 Ku-band Measurement Campaign Results

The Ku-band experiment using the passive measurement technique was conducted at the University of the Bundeswehr, Munich during November 2015. The experimental setup is shown in Figure 6.10, where $v_1$ and $v_2$ are parabolic antennas with 1.8 m diameter and a bore-sight receive gain at 12 GHz of approximately 45 dBi. These two antennas are arranged in a SISO setup to receive the downlink from the two EUTELSAT satellites 7A and 10B at 7° E and 10° E, respectively. The 3 dB beamwidth of these antennas are 0.8 degrees. The antenna discrimination for each antenna towards the alternate satellite at 3 degrees orbital separation is approximately -30 dB.


Figure 6.10: Picture of the Ku-band measurement setup

The two small antennas $y_1$ and $y_2$ are elliptical aperture dishes with an equivalent diameter of 0.75 m. At 12 GHz, these antennas have a bore-sight receive gain of approximately 37 dBi and the 3 dB beamwidth is 2 degrees. Both the small antennas were pointed midway between the two satellites, that is to 8.5° E. Thus the effective antenna gain in the direction of the satellites is reduced to $37 - 12(\frac{1.5^o}{2.0^o})^2 = 30.25$ dB [46] for both antennas $y_1$ and $y_2$.

To measure the channel orthogonality at different inter-antenna spacing $d_G$ between $y_1$ and $y_2$, one antenna $y_2$ was seated on a movable platform with rails to guide the movement, as can be seen in Figure 6.10. For all the antennas, the LNBs in the receive chain used a common 10 MHz GPS reference source. The received signals from all the receivers are down converted to an IF and simultaneously captured using a four channel R&S Real Time Oscilloscope (RTO) [64], controlled through a host PC using a Matlab interface, as shown in Figure 6.11. The RTO digitises the IF signals and uses an inbuilt I/Q software interface for digital signal processing to down-convert the IF signals to complex baseband, followed by filtering and decimation to store I/Q samples at a reduced sample rate.

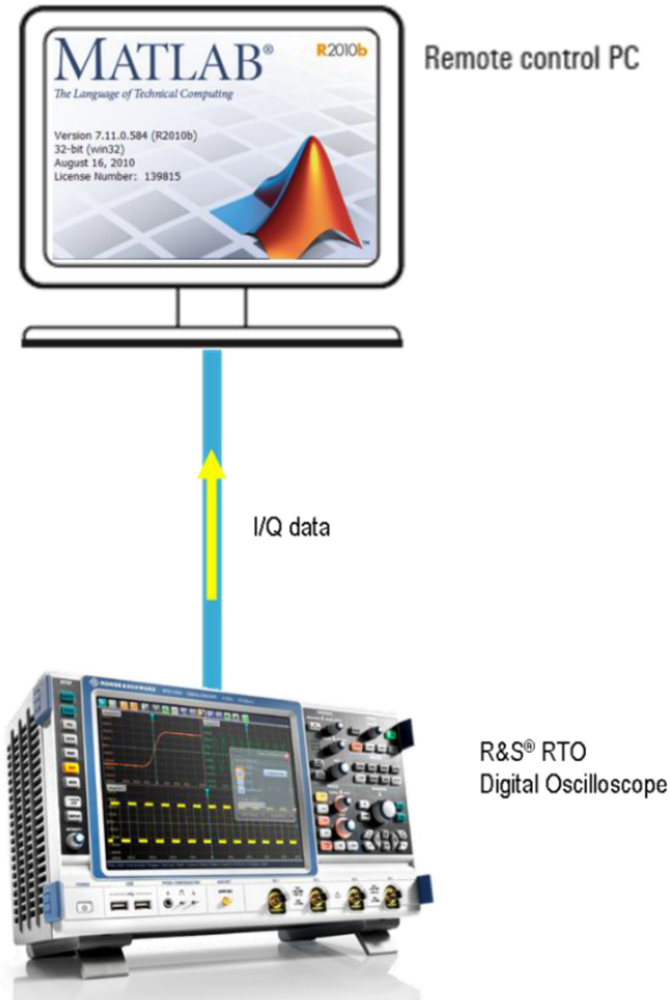


Figure 6.11: Data acquisition setup using RTO and Matlab

In four channel I/Q data capture mode, the RTO can capture up to 6 million complex samples per channel. In each channel, the complex baseband I/Q samples are captured at regular intervals in a burst of one second and one MHz bandwidth, resulting in capture length of $\mathrm{N_s} = 10^6$ samples per channel.

The cross-correlation analysis of the received signals at baseband is shown in Figure 6.12, the results show a single peak at zero time lag in each correlation. The peak value at zero time lag in each subplot denotes a complex coefficient $R_{yv,zm}$ as in (6.10). The signals were captured at a carrier frequency $f = 12.50895$ GHz, where there was a confirmed TV broadcast downlink on one of the satellites and an unknown third-party signal present at the same overlapping frequency on the other satellite. A one MHz of signal bandwidth with frequency overlap was available for capture, opportunistically making use of existing downlink from both the satellites.

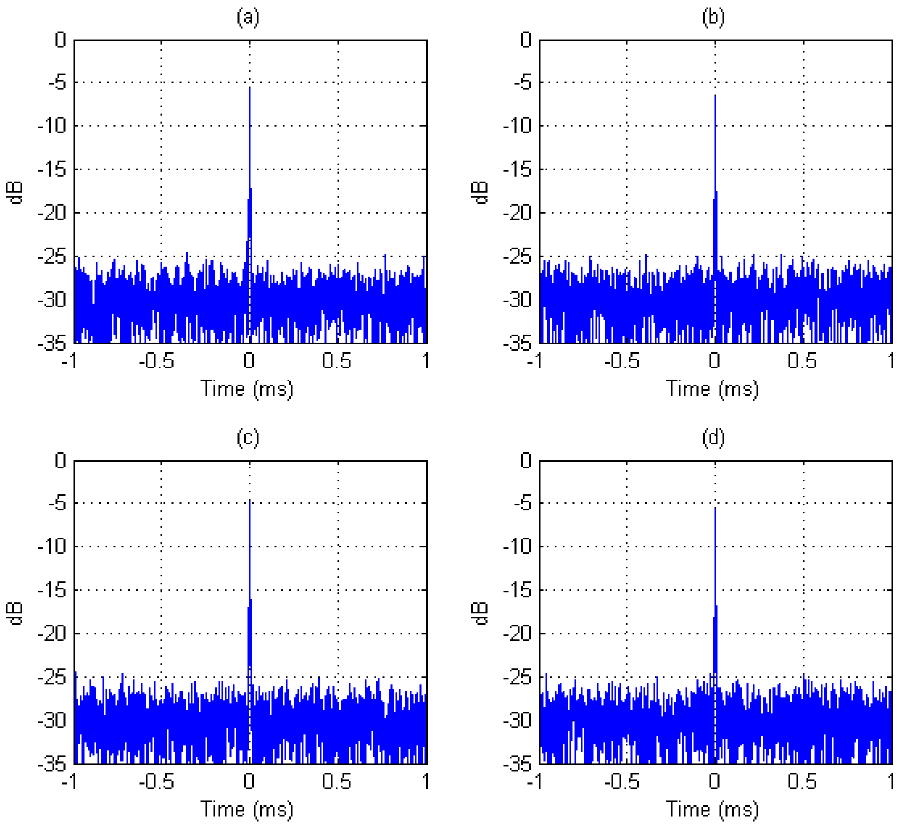


Figure 6.12: Cross correlation analysis between: (a) $y_1$ and $v_1$ (b) $y_1$ and $v_2$ (c) $y_2$ and $v_1$ (d) $y_2$ and $v_2$

### 6.4.1 Antenna separation test

The main aim of the antenna separation test is to measure the phase relationship in the channel matrix to estimate the channel orthogonality at different $d_G$ values. The measurement results shown in Figure 6.13 are obtained by advancing $v_2$ by one cm every 30 seconds. Approximately three burst of measurements are made at each antenna separation position. The top plot shows the channel phase relationship (6.5), where the channel is fully orthogonal when $|\psi| = \pi$ and denotes a key-hole region when $|\psi| = 0$. Starting from a key-hole region at $d_G = 1.3$ m, $v_2$ is swept across the fourth maxima position ($d_G = 1.5$ m) to the fifth maxima position at $d_G = 1.92$ m.

The predicted result is based on the theoretical calculation from known location of the satellites at the time of the measurement using operator provided ephemeris data and known geometry of $\mathrm{y}_1$ and $\mathrm{y}_2$. The orientation of antennas $\mathrm{y}_1$ and $\mathrm{y}_2$ ($\delta_{\mathrm{G}} = -20.6^{\mathrm{o}}$) with respect to the local East-West direction and the height difference (0.22 m) between $\mathrm{y}_1$ and $\mathrm{y}_2$, due to placement of $\mathrm{y}_2$ in a raised platform are taken into consideration to theoretically predict the channel phase relationship.

The measured and predicted channel phase relationship values match very well. The bottom subplot in Figure 6.13 shows the normalised channel capacity with respect to $\mathrm{d}_{\mathrm{G}}$, and again both the measured and predicted values match well. The channel capacity in this case is derived from the differential phase estimates $\widehat{\phi}_{zm}$ (6.14):

$$\begin{aligned}
\Phi_{yv} &= \begin{bmatrix} e^{-j2\pi\widehat{\phi}_{11}} & e^{-j2\pi\widehat{\phi}_{12}} \\ e^{-j2\pi\widehat{\phi}_{21}} & e^{-j2\pi\widehat{\phi}_{22}} \end{bmatrix} \\
&\approx \begin{bmatrix} e^{-j2\pi\phi_{11}} & e^{-j2\pi\phi_{12}} \\ e^{-j2\pi\phi_{21}} & e^{-j2\pi\phi_{22}} \end{bmatrix} \begin{bmatrix} e^{j2\pi\phi_1} & 0 \\ 0 & e^{j2\pi\phi_2} \end{bmatrix} \\
&\approx \widetilde{\mathbf{H}} \begin{bmatrix} e^{j2\pi\phi_1} & 0 \\ 0 & e^{j2\pi\phi_2} \end{bmatrix},
\end{aligned} \tag{6.32}$$

where $\widetilde{\mathbf{H}}$ (2.5) denotes phase components of the channel matrix without path attenuation and antenna gain. Irrespective of the phases $\phi_1$ and $\phi_2$ from the two SISO channel paths, the singular values or the capacity of the channel will remain unaffected, hence the channel capacity from the measured phase data can be calculated from:

$$C \approx \log_2 \det \left(\mathbf{I}_2 + \frac{\rho}{2}\Phi_{yv}\Phi_{yv}^{\dagger}\right) \quad \text{bits/s/Hz}. \tag{6.33}$$

The predicted capacity using (6.4) from the known geometry of the setup and the measured values of the channel capacity using (6.33) are compared in Figure 6.13 bottom subplot (6.33). This is the result of a well balanced measurement setup, i.e. high spatial discrimination between antennas $\mathrm{v}_1$ and $\mathrm{v}_2$, and approximately equal measurement SNRs, respectively. The top subplot of Figure 6.14 shows the standard deviation of the phase measurements, from the captured samples as per (6.21). All values are suf-

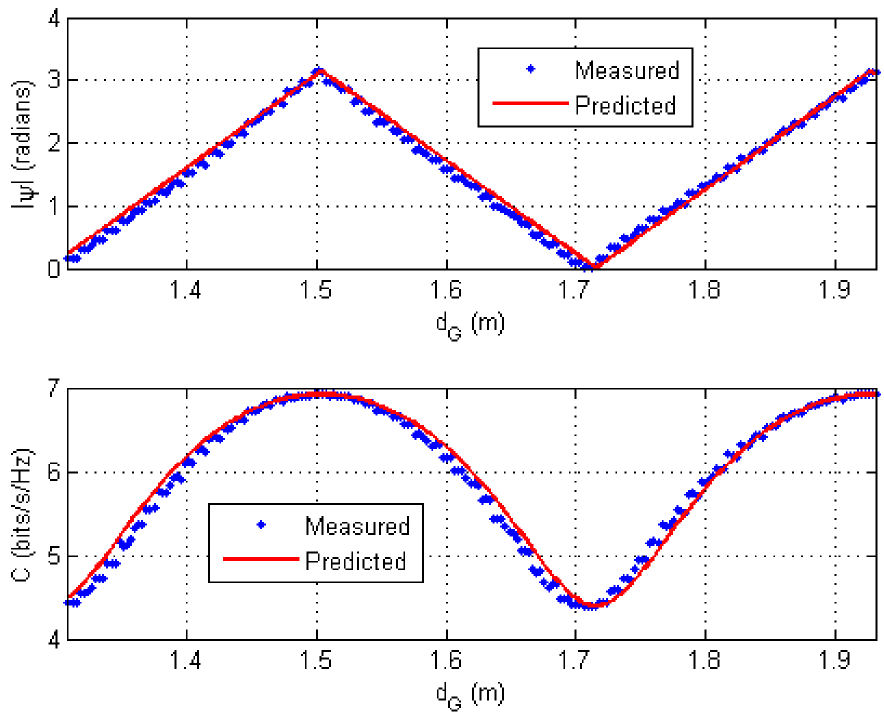


Figure 6.13: Ku-band antenna separation measurement: (top) Phase relationship in the channel matrix and (bottom) capacity

ficiently low, which also confirms reliable phase estimates from measurements. Finally, the bottom subplot of Figure 6.14 shows the absolute values of the cross-correlation coefficient peaks at zero time lag, in decibels. The interest in this is to analyse the relative level between the coefficients. From the setup, it is known that the channel gain of all MIMO channel path elements and SISO path elements are approximately equal: $|h_{11}| \approx |h_{12}| \approx |h_{21}| \approx |h_{22}|$ and $|h_1| \approx |h_2|$, respectively. Since the difference between the correlation coefficients are within 1 dB and nearly constant for all antenna spacings, this satisfies that the downlink power from the two satellites are approximately equal $\sigma_{s_1}^2 \approx \sigma_{s_2}^2$.

### 6.4.2 Satellite orbital drift

Although the geo-stationary satellites appear to be stationary in space to the observer on the ground, in practice it is impossible to maintain the satellite absolutely immobile with respect to the Earth. Due to the consequence of orbital perturbations, the satellite

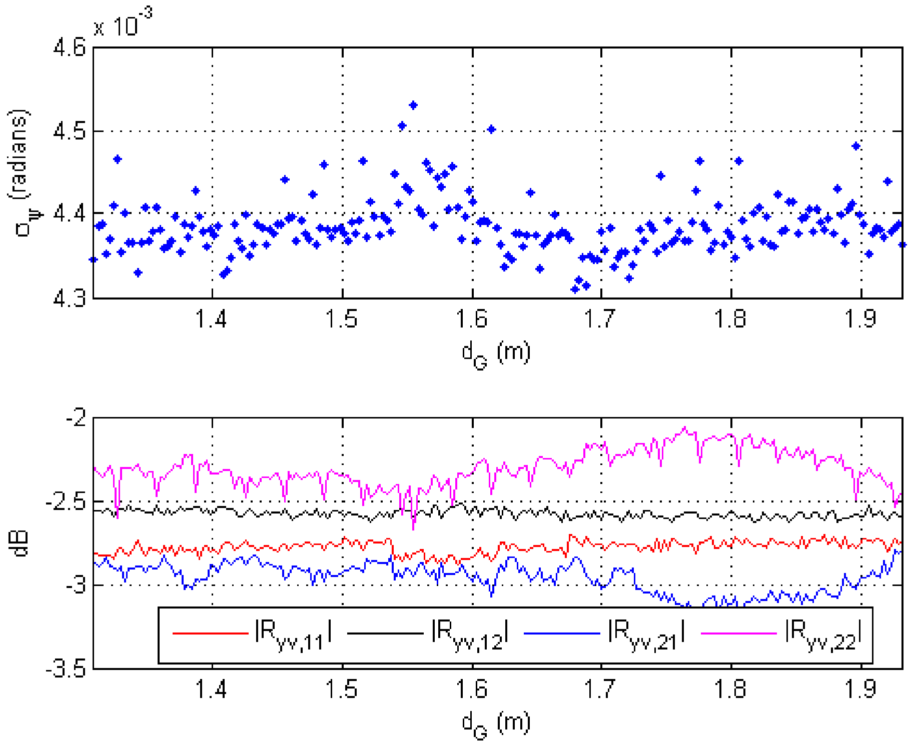


Figure 6.14: Ku-band antenna separation measurement: (top) standard deviation of phase measurements and (bottom) absolute value of cross-correlation coefficients

is never stationary at the nominal position. As described by the non-zero eccentricity and inclination, each satellite will tend to oscillate from its nominal longitudinal position and with respect to the equatorial plane [46].

For a given fixed spacing between the antennas $y_1$ and $y_2$ at an optimal $d_G$ value, the movement of satellites will affect the channel orthogonality. During the measurement week, a period of four days of satellite movements are shown in Figure 6.15, based on the operator provided satellite ephemeris data. These orbital movements are typical of a geo-stationary satellite and are within a nominally defined station keeping volume. The satellite movement impact on the optimal location contours using the ephemeris data is shown in Figure 6.16. The smearing effect (see Section-3.6) in the contours compared to Figure 6.4 is a consequence of the 24-hour period of the satellite movement.

It can be observed from Figure 6.16 that for a small optimal spacing between $y_1$ and $y_2$, the impact is less pronounced. However, at farther spacing between the antennas, the channel orthogonality varies by a greater amount in a 24-hour period. Many hours

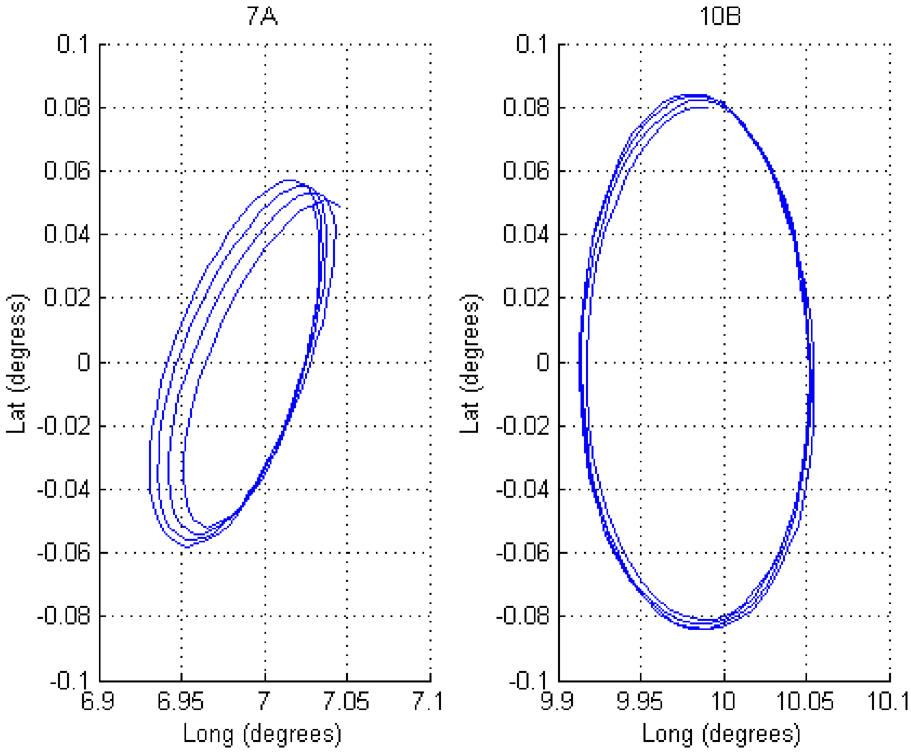


Figure 6.15: Satellite movement: (left) EUTELSAT-7A and (right) EUTELSAT-10B: Period (4 days of data from 23 Nov 2015 00:00:00 UTC)

of channel measurements were recorded at multiple maxima positions (i.e. fixed $d_G$), as shown on Figure 6.16. Due to the physical constraint in the setup, close antenna spacing could not be achieved, hence the channel measurement were recorded only at the $4^{th}$, $5^{th}$ and $6^{th}$ maxima positions corresponding to $d_G = 1.51$ m, $1.93$ m and $2.35$ m, respectively.

The measurement results from the $4^{th}$ maxima position are shown in Figure 6.17, the top subplot shows the channel orthogonality and bottom subplot shows the normalised capacity. The signals are captured in one second bursts at an interval of once every 36 seconds approximately. The oscillation in the channel orthogonality is measured owing to the satellite orbital movements with respect to the ground, the results are compared with predicted pattern based on the satellite ephemeris. Throughout the 39 hours, the measured results match the predicted periodic pattern. In this case, the normalised capacity reduces down to 97%, which is an expected behaviour.

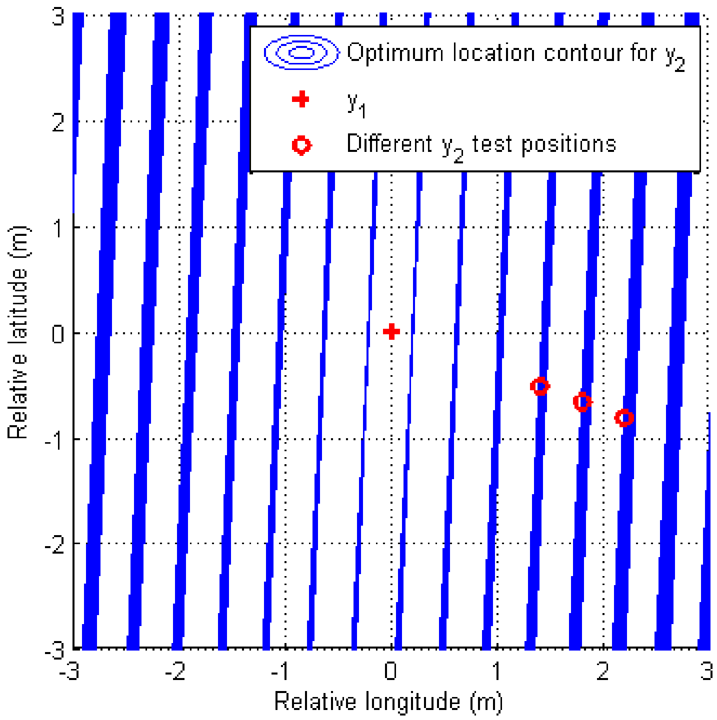


Figure 6.16: Satellite movement impact on the optimal user location contours

The standard deviation of the phase measurements and the absolute values of the cross-correlation coefficients for the 4$^{\text{th}}$ maxima position are given in the top and bottom subplots in Figure 6.18, respectively. Throughout, $\sigma_\psi$ is approximately around 0.01 radians. Such a low value indicates reliable phase measurements with sufficient accuracy. The $|R_{yv,zm}|$ data are roughly within a 2 to 3 dB range and this ensures the error in the phase estimation due to the phase bias is kept low in (6.30). The ratios $\frac{|R_{yv,11}|}{|R_{yv,12}|}$ and $\frac{|R_{yv,21}|}{|R_{yv,22}|}$ approximately measure the power level difference between the two satellites $\frac{\sigma_{s_1}^2}{\sigma_{s_2}^2}$. The significance of the having equal power level on both satellite signals were discussed in Figure 6.7 and Figure 6.9 .

The drop in the received signal power level at elapsed time around the 18$^{\text{th}}$ hour and 26$^{\text{th}}$ hour in the cross-correlation coefficients is an one-off event, possibly highlights a measurement glitch or antenna blockage. However, a series of events at around the 19$^{\text{th}}$ hour and 27$^{\text{th}}$ hour, highlights the disappearance and appearance of the signal from $s_2$ for a brief period of time. This is one drawback of this passive measurement method, but nevertheless, it isn't a significant hindrance to the channel measurement.

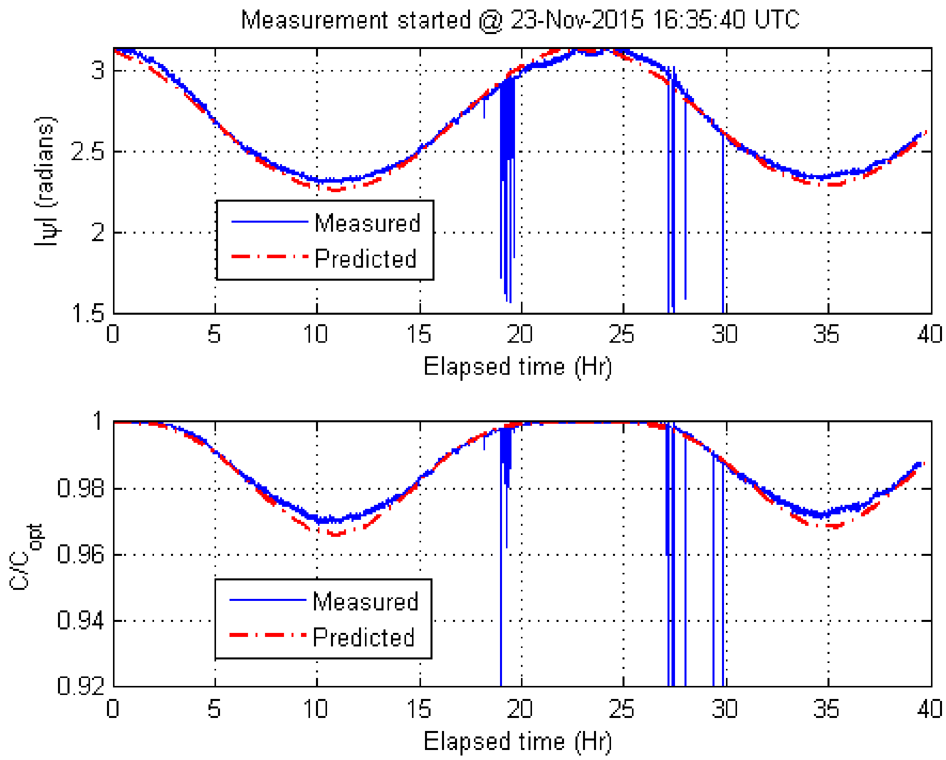


Figure 6.17: Ku-band 4$^{\text{th}}$ maxima position: (top) Phase relationship in the channel matrix and (bottom) normalised capacity

Similar results for $\mathrm{d_G}$ for the 5$^{\text{th}}$ and 6$^{\text{th}}$ maxima positions are shown in Figure 6.19 and Figure 6.21, respectively. Close agreement is found between the measured and predicted results. It is evident that the variation in the channel orthogonality is more pronounced at 6$^{\text{th}}$ maxima position compared to 5$^{\text{th}}$ or 4$^{\text{th}}$ maxima position, as predicted. The normalised capacity reduces down to 97%, 96% and 93% in 4$^{\text{th}}$, 5$^{\text{th}}$ and 6$^{\text{th}}$ maxima positions, respectively.

The corresponding standard deviation of the phase measurement and absolute values of the cross-correlation coefficients for 5$^{\text{th}}$ and 6$^{\text{th}}$ maxima positions are shown in Figure 6.20 and Figure 6.22, respectively. In both cases, the $\sigma_\psi$ values are around .005, better than the measurements at the 4$^{\text{th}}$ maxima position, mainly attributing to the increase in the correlation peak due to increased SNR of the received signals.

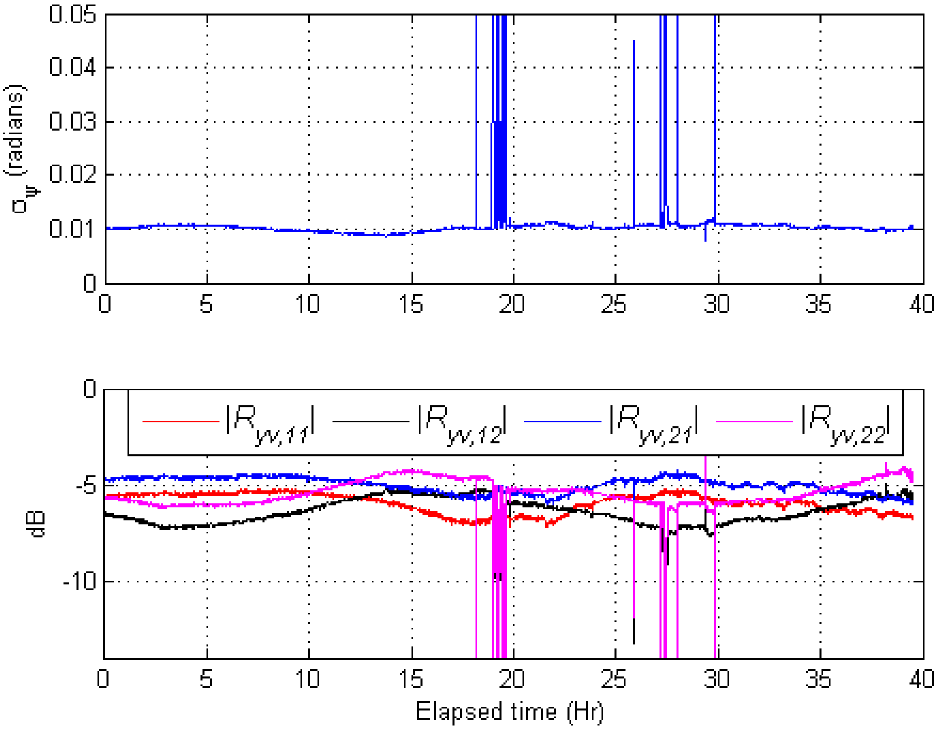


Figure 6.18: Ku-band 4$^{\text{th}}$ maxima position: (top) standard deviation of phase measurement sand (bottom) absolute value of cross-correlation coefficients

## 6.5 X-band Measurement Campaign Results

The X-band measurement campaign using the passive channel measurement technique was conducted during November 2016, using facilities at the DST Group, Edinburgh, South Australia. The Ku-band results from the passive channel measurement technique are sufficient to prove the spatial MIMO SATCOM concept. However, the X-band measurement results are significant to independently validate the theory in a different frequency band, antenna setup and with different orbital separation in space and in the ground.

A picture of the X-band measurement setup is shown in Figure 6.23, where $v_1$ and $v_2$ are parabolic antennas with 2.0 m diameter with bore-sight receive gain at 7.6 GHz of approximately 42 dBi. These two antennas are arranged in a SISO setup to receive the downlink from a WGS satellite and a SKYNET satellite at 88.4° E and 95.2° E, respectively. The 3 dB beamwidth of these antennas are 1.4 degrees. The

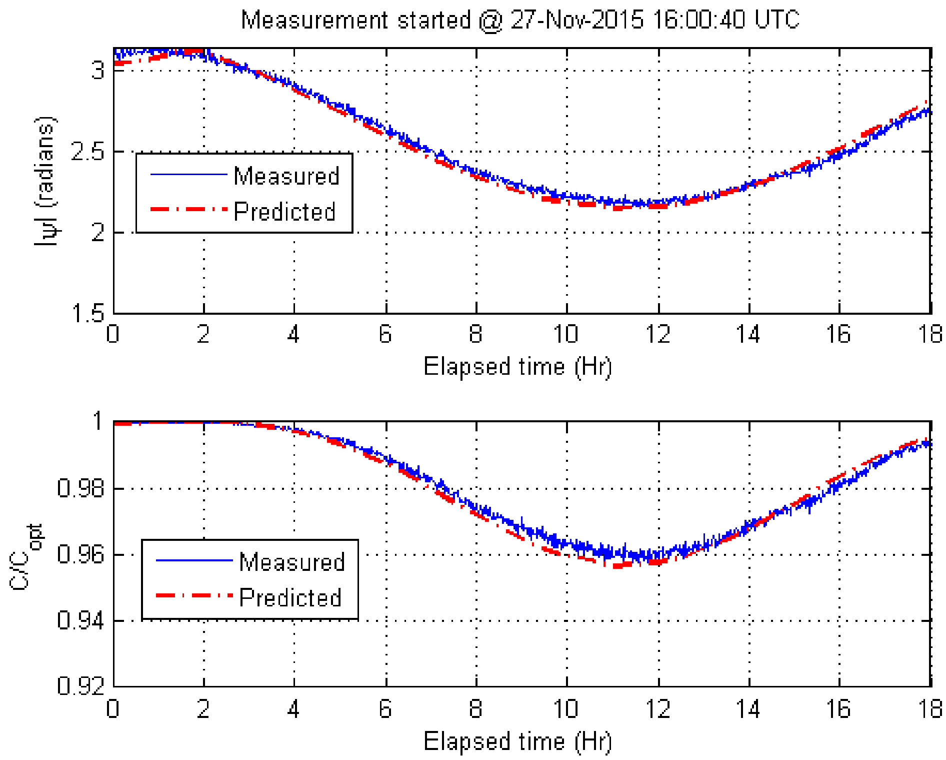


Figure 6.19: Ku-band 5$^{\text{th}}$ maxima position: (top) Phase relationship in the channel matrix and (bottom) normalised capacity

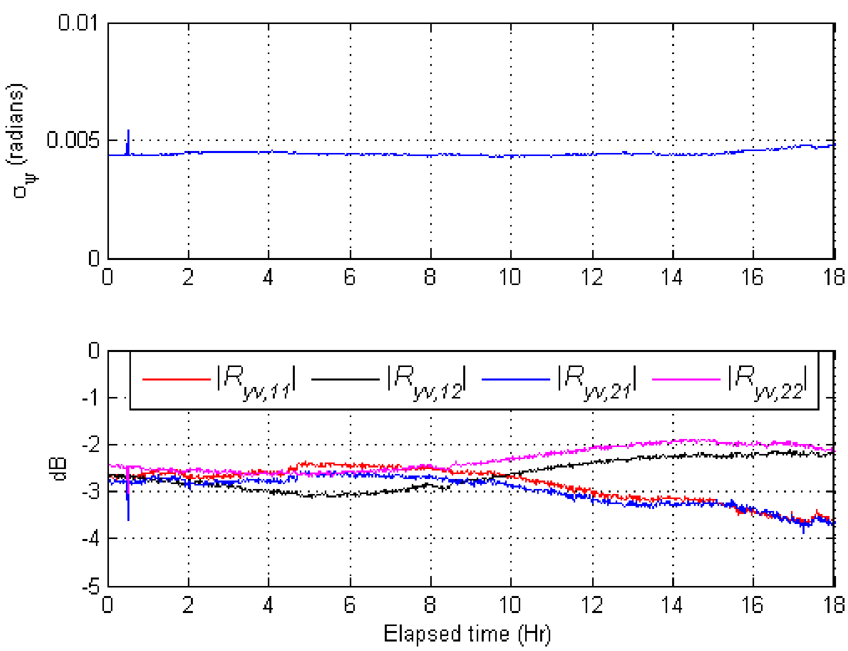


Figure 6.20: Ku-band 5$^{\text{th}}$ maxima position: (top) standard deviation of phase measurements and (bottom) absolute value of cross-correlation coefficients

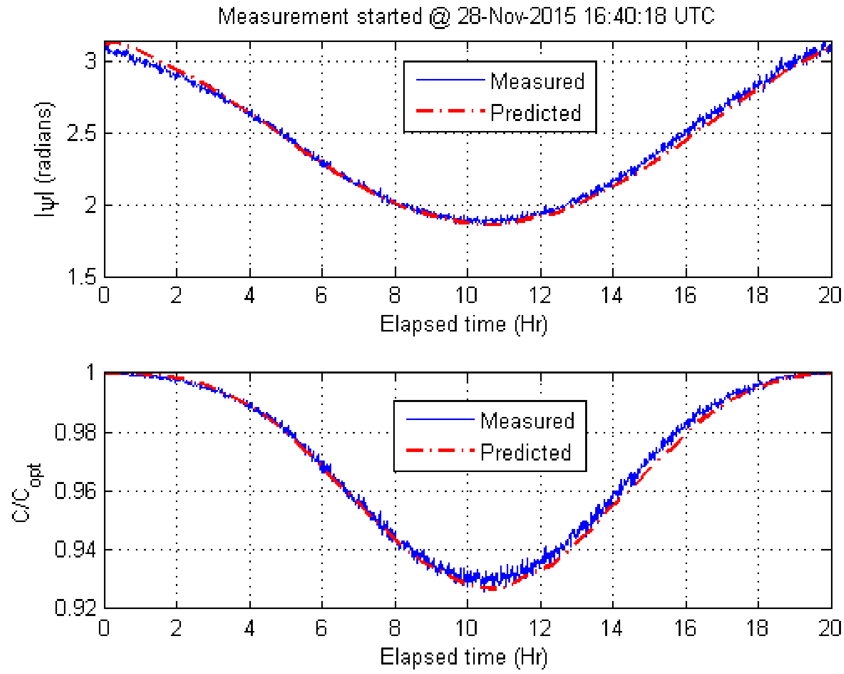


Figure 6.21: Ku-band 6$^{\text{th}}$ maxima position: (top) Phase relationship in the channel matrix and (bottom) normalised capacity

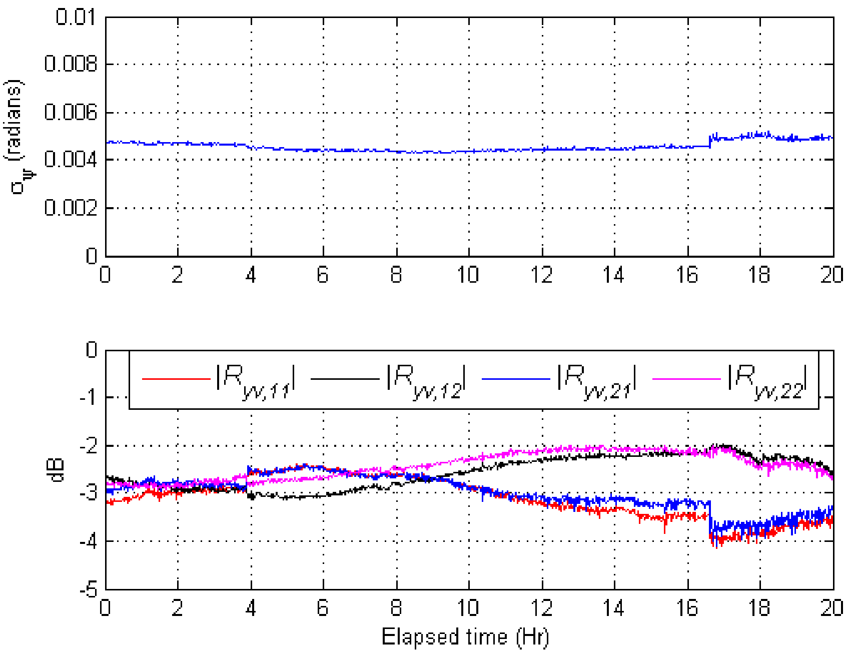


Figure 6.22: Ku-band 6$^{\text{th}}$ maxima position: (top) standard deviation of phase measurements and (bottom) absolute value of cross-correlation coefficients

antenna discrimination for each antenna towards the alternate satellite at 6.8 degrees is approximately -33 dB.

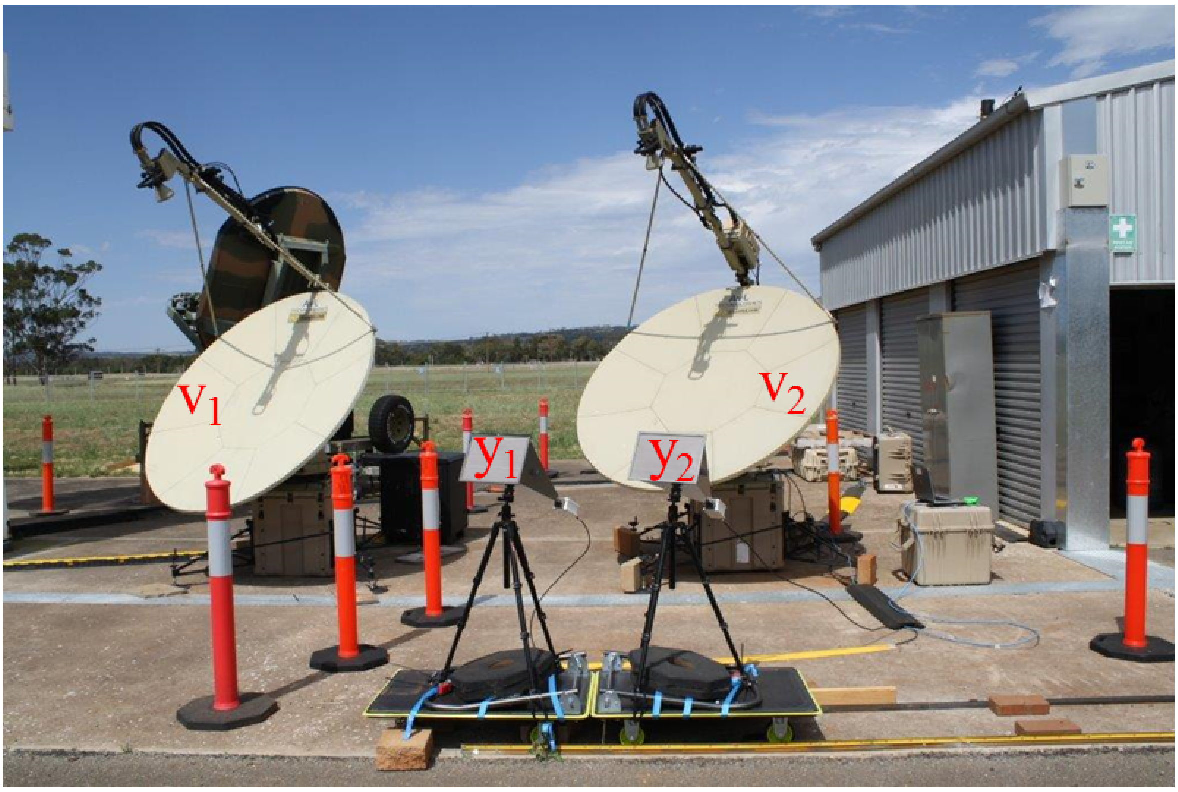


Figure 6.23: Picture of the X-band measurement setup

However, $y_1$ and $y_2$ are linearly polarized horn antennas with 24 dBi gain and 3 dB beamwidth equal to 10.5 degrees. Since the downlink signals from the satellites are circularly polarized, the effective boresight gain will be reduced to 21 dBi. Due to 6.8 degrees orbital separation between the two satellites, both the horn antennas are pointed midway between the two satellites. Thus the the effective antenna gain in the direction of the satellites is further reduced to $21 - 12(\frac{3.4^o}{10.5^o})^2 = 19.75$ dB [46] for both the antennas $y_1$ and $y_2$.

Both horn antennas are mounted using a tripod and firmly attached on top of a trolley, where $y_1$ is left fixed and $y_2$ is movable with rails to guide the movement in a straight line, as shown in Figure 6.23. In the setup, to enable channel measurements at multiple capacity maxima positions, the distance between $y_1$ and $y_2$ is variable from as low as $d_G = .80$ m to $d_G = 3.51$ m. The orientation of $y_1$ and $y_2$ is exactly in the North-South direction, that is $\delta_G = -90$ degrees.

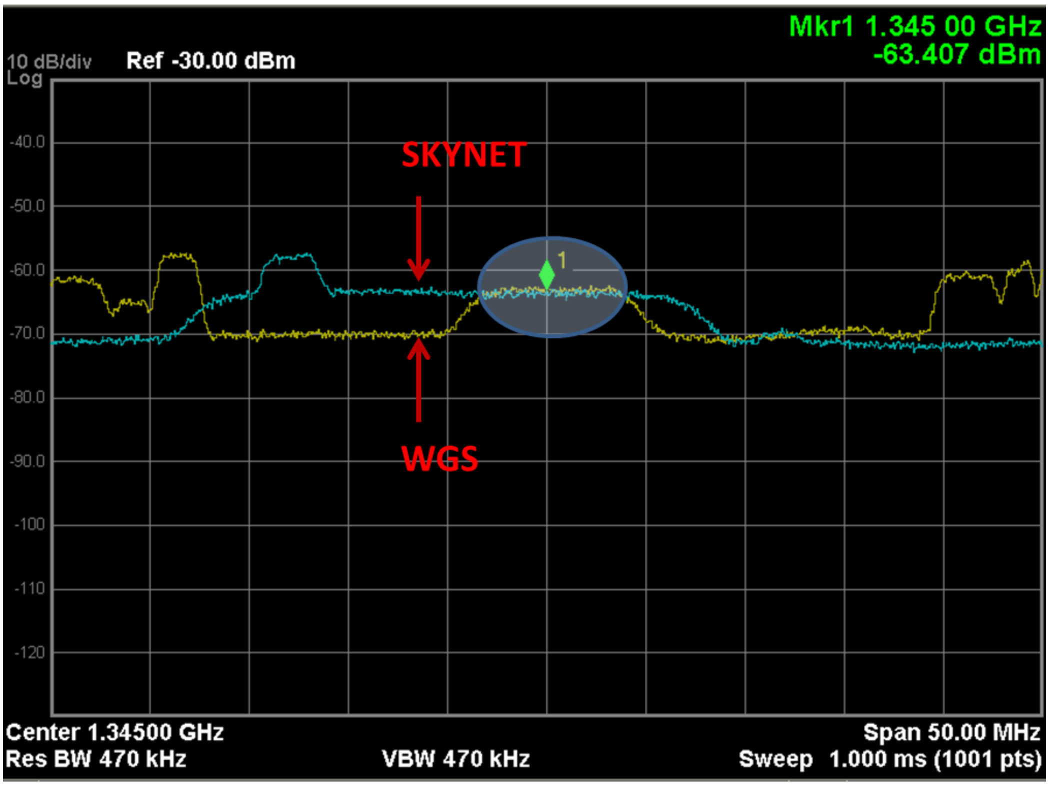


Figure 6.24: Spectral overlap of the X-band signals (shown at L-band IF)

Similar to the Ku-band setup, in the X-band setup, all the LNBs in the receive chain use a common 10 MHz reference source. The LNBs down-convert the X-band to an L-band IF, the RTO digitises and captures the baseband I/Q samples in all four channels. The spectral overlap of the X-band signals from the two satellites is shown in L-band IF in Figure 6.24 [4]. The spectral plot highlights the region where the downlink signal overlap between the two satellite at approximately the same power level. The signals are captured at $f$ = 7.545 GHz, in 6 MHz bandwidth, for one second duration, resulting in a capture length $N_s$ = 6 million baseband I/Q per channel. It can be noticed in Figure 6.24 that there is carrier signal at that frequency on WGS[5], whereas in the case of SKYNET, the transponder noise from the satellite is used in the analysis.

A sample of the cross-correlation analysis of the signals is shown in Figure 6.25. As expected, the correlation peak in all the cases occurs at the zero time. Please note that

[4]The spectral plot is captured using a high gain 4.6m dish, pointing at one satellite at a time and capturing the spectrum display

[5]The signals are not demodulated or analysed beyond the calculation of the correlations. During the measurement, the raw data were immediately discarded after the calculation.

the horizontal axis is denoted by correlation sample index. Comparing to the Ku-band cross-correlation analysis from Figure 6.12, the cross-correlation peak values in X-band are lower due to lower SNRs, resulting from a combination of reduced antenna gain and a lower satellite downlink power level. However, the cross-correlation is also increased, owing to increase in $N_s$ to 6 million samples per channel in X-band compared to 1 million samples per channel in Ku-band.

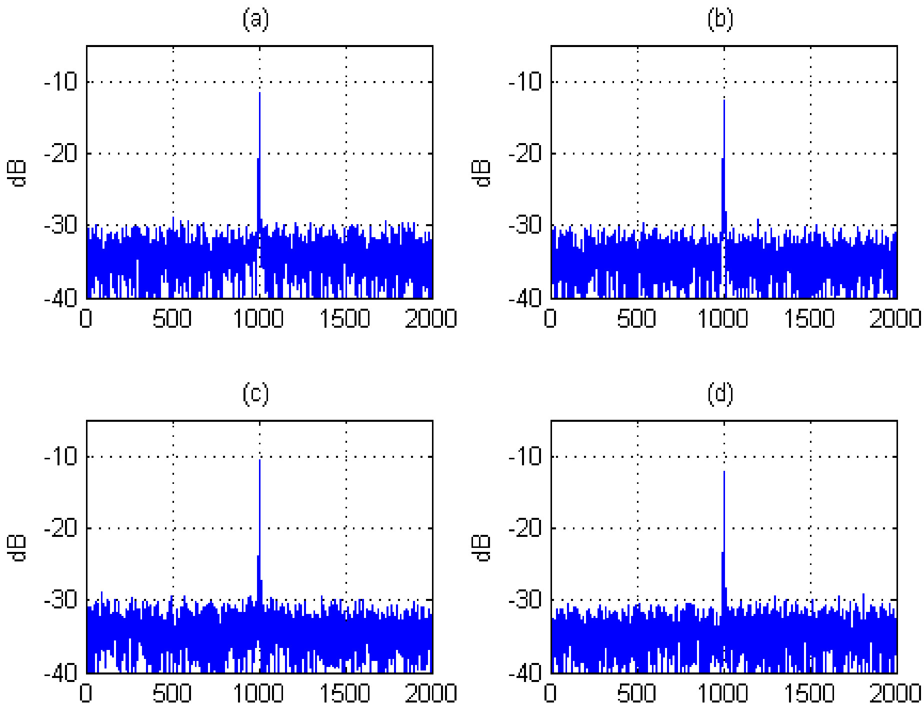


Figure 6.25: X-band cross-correlation analysis between: (a) $y_1$ and $v_1$ (b) $y_1$ and $v_2$ (c) $y_2$ and $v_1$ (d) $y_2$ and $v_2$

### 6.5.1 Antenna separation test

The channel measurement results from the X-band antenna separation test are given in Figure 6.26. The channel is measured by moving $y_2$ in 5 cm intervals. The interval is reduced at positions where $|\psi|$ is close to 0 or $\pi$ radians to measure the channel with a better precision. The results span over multiple maxima points, from the $2^{\text{nd}}$ maxima to the $5^{\text{th}}$ maxima position, corresponding from $d_G = .95$ m to $d_G = 2.94$ m, respectively. The measured channel phase relationship (6.15) matches well with the predicted results (6.5), which is based on the known location of the satellites at the time of the measurement and the known geometry of the antenna orientation on the ground.

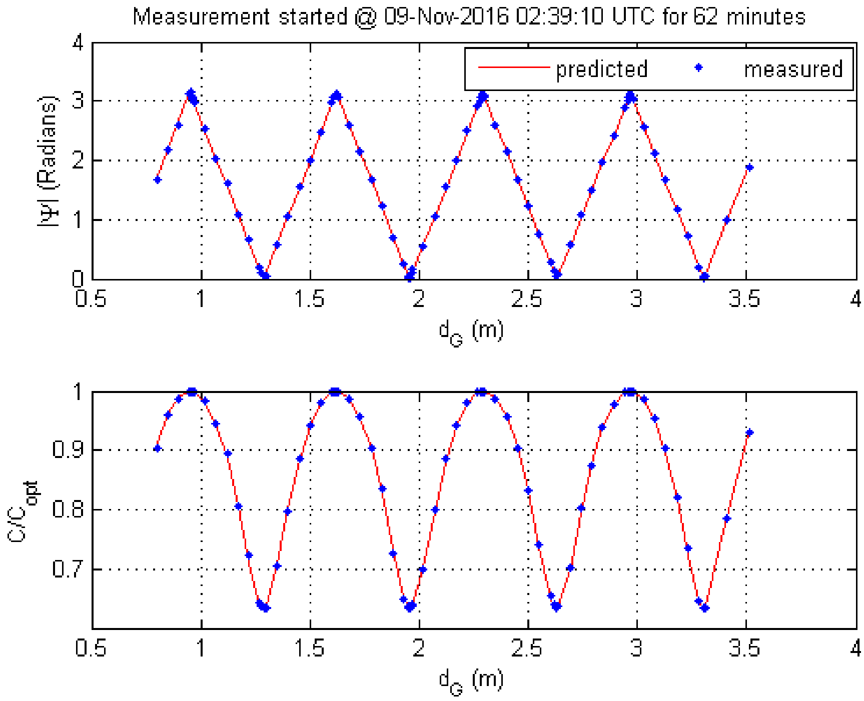


Figure 6.26: X-band antenna separation measurement: (top) Phase relationship in the channel matrix and (bottom) normalised channel capacity

The standard deviation of the phase measurement and the absolute values of the cross-correlation peak coefficients corresponding to the antenna separation is given in Figure 6.27. From the results, it can be concluded that reliable phase estimates were made from the measurement without any observable phase bias.

### 6.5.2 Satellite orbital drift

Similar to the Ku-band analysis, the orbital movement of the two satellites are shown in Figure 6.28. In this case, the satellite movement are tracked through an openly available web source [59] and the TLE data for the satellites are obtained from [65]. From the TLE data, satellite ephemeris data are then generated using the STK tool. The satellite ephemeris thus obtained are not guaranteed to be accurate. The smearing

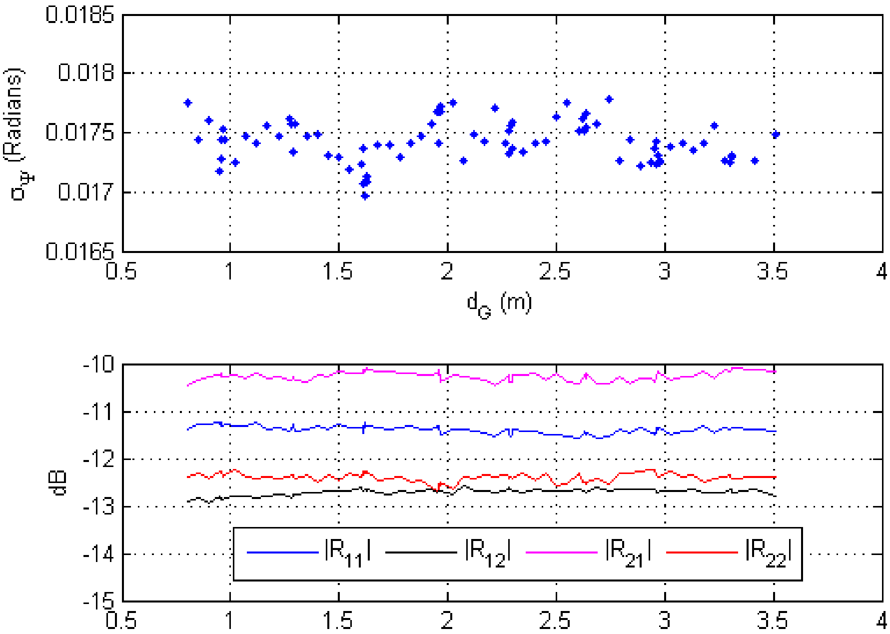


Figure 6.27: X-band antenna separation measurement: (top) standard deviation of phase measurement and (bottom) absolute value of cross-correlation coefficients

effect in the optimum location contours due to the satellites movement is shown in Figure 6.29.

Many hours of channel measurements were recorded at multiple maxima positions, as shown on Figure 6.29. Due to the physical constraint in the setup, close antenna spacing at the $1^{st}$ maxima position could not be achieved, hence the channel measurements were recorded only at the $2^{nd}$, $3^{rd}$, $4^{th}$ and $5^{th}$ maxima positions corresponding to $d_G = .95$ m, 1.62 m 2.29 m and 2.94 m, respectively. These results are provided in Appendix-A.

## 6.6 Chapter Review

In this chapter, a novel passive technique to measure and validate a two satellite MIMO SATCOM channel is presented. The measurement method uses cross-correlation analysis of the received signals to estimate differential phase measurements. These phase measurements are used to estimate the channel orthogonality. Accuracy analysis of

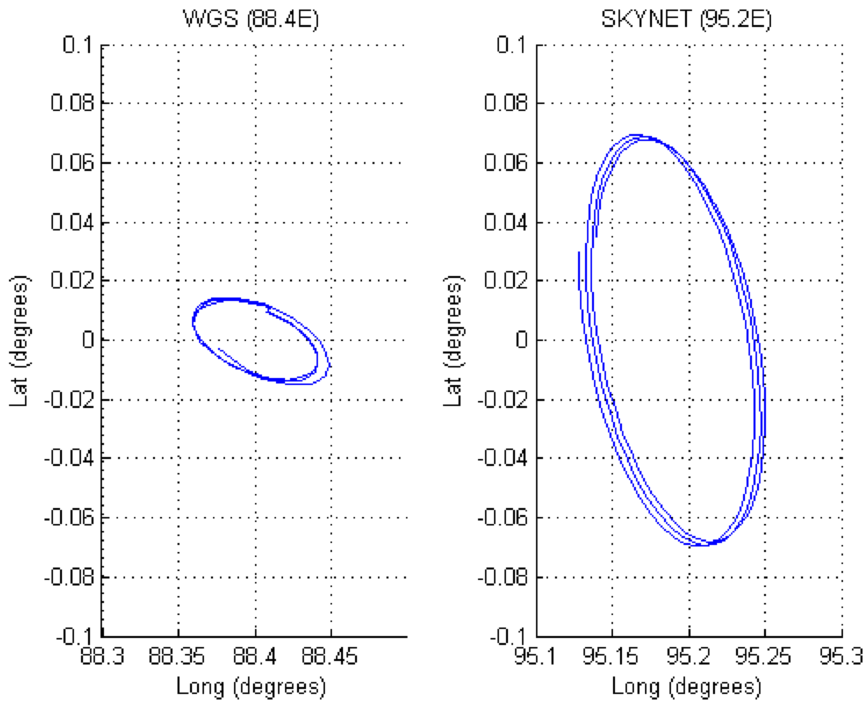


Figure 6.28: Satellite movement: (left) WGS and (right) SKYNET

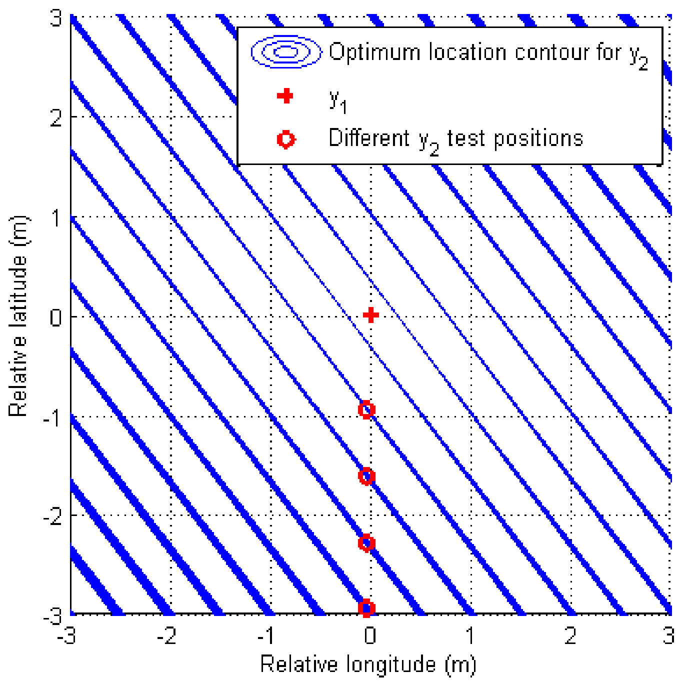


Figure 6.29: Satellite movement impact on the optimal locations contours

the proposed measurement method is presented and compared with simulation. The parameters that cause bias in phase estimates are analysed using simulations. Results from successful experimental campaigns in Ku-band and X-band using signals are significant in proving and validating the MIMO SATCOM channel. The proposed passive measurement technique is a useful and convenient method to validate the MIMO SATCOM channel, including the impact due to independent satellite ephemeris, different orbital spacing of satellites, different frequency bands and long term phase stability in the channel.

# Chapter 7

# Conclusions and Future Work

The main aim of this thesis was to study the application of Multiple Input Multiple Output (MIMO) techniques to Satellite Communications (SATCOM). The success realised from the application of MIMO techniques in terrestrial wireless communications has generated this interest to study MIMO for SATCOM. However, a SATCOM channel can be unlike the terrestrial channel in that it often does not exhibit the rich scattering environment and multi-path propagation that has traditionally provided opportunities for MIMO gain. The SATCOM channel is principally dominated by the Line of Sight (LOS) path. The absence of scatterers in the SATCOM propagation path leads to rank deficiency in the spatial MIMO channel matrix. Hence, at a first glance it appears that MIMO may not be able to provide spatial multiplexing gains in SATCOM. However, in spite of a strong LOS path in the SATCOM channel, this thesis shows the application of MIMO is possible and has explored the application to SATCOM through spatial geometrical optimisation methods.

## 7.1 Review of Polarization multiplexing

The majority of the MIMO SATCOM research in existing literature focus on using polarization in Land Mobile Satellite (LMS) channels at L-band and S-band frequencies. In this thesis, importance is given to analyse the circular polarization at X-band frequencies and above. Utilisation of orthogonal polarizations as two independent Single Input Single Output (SISO) systems is a well known frequency reuse concept in SATCOM at higher frequency bands. However, it is shown that poor Cross Polar Isolation (XPI) in the link, mainly due to antenna polarization misalignment, can significantly degrade the communications system performance. The commonly used polarization metrics are XPI, Cross Polar Discrimination (XPD) and Axial Ratio (AR). These metrics defines the state of the polarization in-terms of amplitude, but ignores the phase information.

In this thesis, a polarization antenna model is derived with both amplitude and phase errors in polarization excitation. Using the model, it is shown that in a MIMO context, the system performance degradation can be made negligible. For MIMO systems, it is shown that the term polarization parallelity has more significance than the conventional term XPD in defining the polarization state of an antenna.

Using an example case study, an analysis was presented using the Singular Value Decomposition (SVD) technique, with a channel model utilising both spatial and polarization multiplexing gains. The aim was to increase the channel capacity by up to four fold in X-band. The antenna polarization was analysed in-terms of the term polarization parallelity. The results show that approximately 10% of the total achievable capacity is lost with an average polarization parallelity.

## 7.2 Review of Multiple Satellite Systems

This work was motivated by the research done by Prof. Knopp and his team at the Munich University of the Bundeswehr, Germany, in spatial geometrical optimisation for MIMO SATCOM. It is shown that to achieve MIMO spatial multiplexing in LOS dominated SATCOM channels, either the antennas in space or antennas at the ground must be separated by a large distance. Typically, geostationary satellites with overlapping frequency bands are not placed in orbit at a narrow spacing to avoid adjacent satellite interference. A MIMO SATCOM approach using two satellites within the orbital separation between $0.5^o$ and $2^o$ can boost the overall channel capacity into a high demand region. At the same time, we've acknowledged that using multiple satellites for spatial multiplexing may not always be considered cost effective. However, in this thesis the focus has been given into investigating the application to narrowband Military SATCOM (MILSATCOM) in UHF band. The analysis shows that MIMO SATCOM in UHF band is one example where spatial multiplexing can be most useful to increase the channel spectral efficiency using two satellites.

A generic channel model has been derived based on Ricean distribution properties, to include both LOS and Non-LOS (NLOS) paths. The spatial antenna geometry was analysed with respect to channel capacity. The channel capacity formulation and analysis is based on a non-regenerative satellite payload, where uplink and downlink from satellite to the user are MIMO links and uplink and downlink from satellite to anchor are two SISO links. Irrespective of the Ricean distribution factor, the phase relationship in the channel was seen to be dominated by LOS paths. For a $30^o$ spacing between the two satellites, an inter antenna spacing of approximately one metre was required on the ground. Practical measurement results conducted by Prof. Knopp's team using two UHF satellites at $63^o$E and $13^o$E independently verify the theoretical analysis presented in this thesis [66, 67] .

A simple, yet an efficient receiver signal processing architecture was derived and presented to deal with different propagation time delay and Doppler in the channel paths; in both user uplink and downlink scenarios.

### 7.2.1 Future Direction: MIMO for MUOS

Although the MIMO analysis presented in thesis was targeted for narrowband SATCOM in UHF band, the same concept could also be applied to wider bandwidths in the UHF band. For example, MIMO spatial multiplexing approach could provide opportunities for the US DoD's Mobile User Objective System (MUOS). To achieve a better data rate and quality of service, MUOS is moving away from the conventional 5 kHz or 25 kHz bandwidth transponders to a cellular like service using Wideband Code Division Multiple Access (WCDMA) [68]. MUOS consists of four active satellites in geosynchronous orbit for a worldwide coverage. Each satellite employs 16 spot beams in its field of view, each beam operates at 300 to 320 MHz for user uplink and 360 to 380 MHz for user downlink. Each spot beam is further divided to four 5 MHz WCDMA channels, providing a total of 64 channels per satellite with full frequency reuse between the beams.

By the analysis done in this thesis, the capacity could be further enhanced by using MIMO for MUOS. This would enable more active satellites to operate in the geostationary orbit with overlapping beams. Secondly, even in the current single satellite operation scenario, the system performance can be increased by using a Multi-User MIMO (MU-MIMO) architecture to reduce inter-beam interferences. However, investigation of MIMO waveforms for frequency selective multi-user wideband UHF SATCOM channels is a subject topic for future research.

## 7.3 Review of Single Satellite Multi-User Systems

It has been shown that at lower frequency bands, spatial multiplexing using multiple satellites can provide an increase in the overall spectral efficiency. At higher frequency bands, application of spatial multiplexing in a single satellite scenario has been analysed using MU-MIMO. Next generation Ka-band SATCOM systems are ambitious in-terms of throughput and capacity using multiple spot beams. There are two categories of SATCOM systems that have emerged. The first is High Throughput Satellites (HTS) systems with an aim to increase overall throughput of a satellite. The second category is High Capacity Satellite (HiCapS) systems, where the aim is to increase the satellite's capacity in a given region. The application of MIMO techniques to improve the system performance is a subject topic for research in both these scenarios.

A MU-MIMO technique is proposed and analysed to enhance the capacity of an HiCapS in a given high demand region on the ground. It is known that the MU-MIMO technique can work favourably in LOS channel conditions. In this thesis it is shown that in a satellite with multiple antennas pointing to single beam location on the Earth, it is possible to achieve frequency reuse (in all the beams) based on a selective grouping users at specific locations on the ground. The users on the ground each have a single antenna and do not require cooperation with each other. A framework has been developed to find optimal user locations to maximise the overall spectral efficiency of the satellite in the required region. The analysis shows that the channel capacity can be increased linearly with the number of antennas on the satellite. However, the achievable capacity is sensitive due to non optimal user locations, this sensitivity increases along with the increase in the MIMO order. Communications system performance are assessed in terms of Bit Error Rate (BER) using two conventional linear MIMO decoding approaches, namely Zero Forcing (ZF) and Minimum Mean Square Error (MMSE). The simulation results show that even when the users in a group are not at ideal orthogonal locations, the MMSE approach outperforms the ZF approach when using powerful channel coding techniques such as Low Density Parity Check (LDPC) codes.

### 7.3.1 Future Direction: Multi-Satellite Multi-User Communications

Multi-Satellite Multi-User (MSMU) is an application of MIMO to SATCOM with a profound impact for MILSATCOM users. In a MILSATCOM context, SATCOM links can be subject to electronic attack through interference and satellites themselves are becoming increasing vulnerable. Radio Frequency (RF) emission from SATCOM can also be exploited by an adversary to detect the presence and/or locations of the terminal. MSMU is a novel concept in SATCOM to leverage MIMO techniques, multi beam antenna array technologies and management complexity to support a SATCOM user community. This concept breaks the paradigm of a given user operating on a single satellite at any one time. There is potential in this architecture to increase aspects of resilience for military users in areas such as protection, diversity and secrecy. Key enablers are multi-beam antennas for SATCOM user terminals and the design of physical layer and management systems that support the concept.

## 7.4 Review of Channel Measurement Campaigns

A novel MIMO SATCOM channel orthogonality measurement technique has been presented in this thesis. The experimental setup is based on a passive measurement technique, where no transmission to the satellites is required, instead relying on existing downlinks from two satellites that have overlapping frequency coverage and beam footprints. Differential phase measurements are obtained using cross-correlation analysis. These phase measurements are subsequently used to verify the orthogonality of the MIMO SATCOM channel. Accuracy analysis of the measurement setup together with simulated and measured results are presented in this thesis.

Measurement results from two separate and independent campaigns have been presented and analysed. The first one in Ku-Band using two EUTELSAT satellites 7A and 10B at $7^o$ E and $10^o$ E, respectively, measured at the Munich University of the Bundeswehr. The second one conducted at Defence Science and Technology (DST) Group, Edinburgh, South Australia in the MILSATCOM X-band, using two satellites WGS and SKYNET at $88.4^o$ E and $95.2^o$ E, respectively. Extensive channel measurements were obtained to verify and compare the spatial relationship geometry in the MIMO SATCOM channel. The results from both the measurement campaigns were successful and show very close agreement with the theoretical framework.

# Appendix A

# X-band channel measurement: Additional Results

The X-band channel measurement results at the $2^{nd}$, $3^{rd}$, $4^{th}$ and $5^{th}$ maxima positions corresponding to $\mathrm{d_G} = .95\ \mathrm{m}, 1.62\ \mathrm{m},\ 2.29\ \mathrm{m}$ and $2.94\ \mathrm{m}$ are given in Figure A.1, Figure A.2, Figure A.3, and Figure A.4, respectively. To predict the channel response for comparison with measured results, the satellite ephemeris data must be known for both the satellites. As mentioned in Chapter-6, the satellite orbital positions and TLE are obtained through openly available websites[1] [59] and [65]. It is found that the ephemeris data for WGS is completely out of sync and this was further confirmed by beacon Doppler tracking. Hence, the predicted response from the satellite ephemeris data may not accurately match with the measured results. However, since the station keeping volume for the WGS is very tight compared to other conventional satellites, the channel response from the satellite movements are mostly dominated by the motion of the SKYNET satellite.

The measurement results in Figure A.1, Figure A.2, Figure A.3, and Figure A.4 show the variation in the channel phase relationship $\psi$ (6.5) and normalised capacity with respect to time due to the movement of the orbital movement of the satellites. Due to erroneous ephemeris data for WGS4, a fixed orbital position is assumed for WGS.

[1] **SatFlare** for satellite tracking and **Mike McCant's** site for satellite TLE download

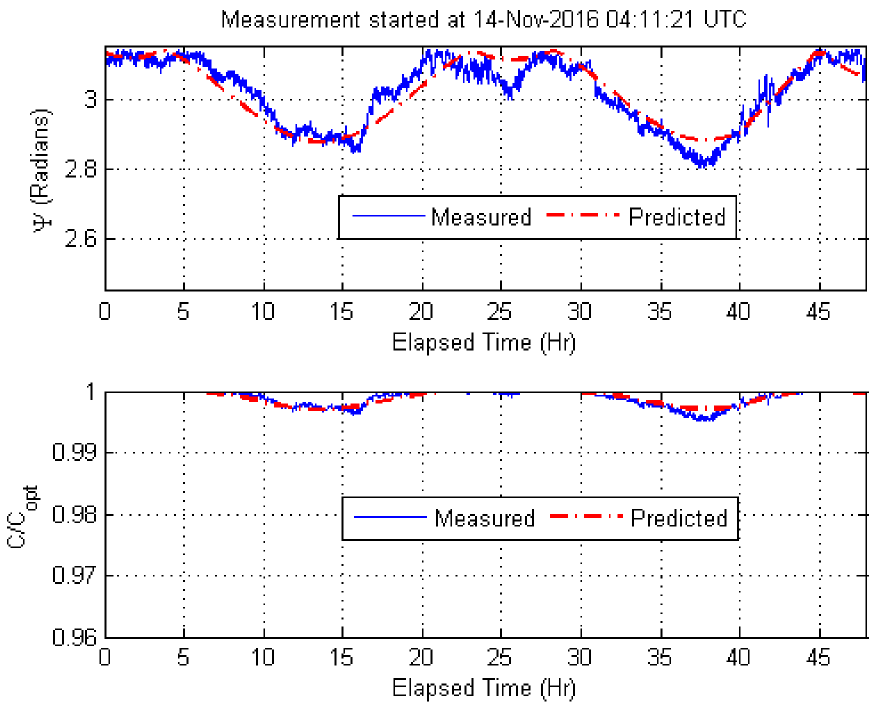


Figure A.1: X-band 2nd maxima position: (top) channel orthogonality and (bottom) normalised capacity

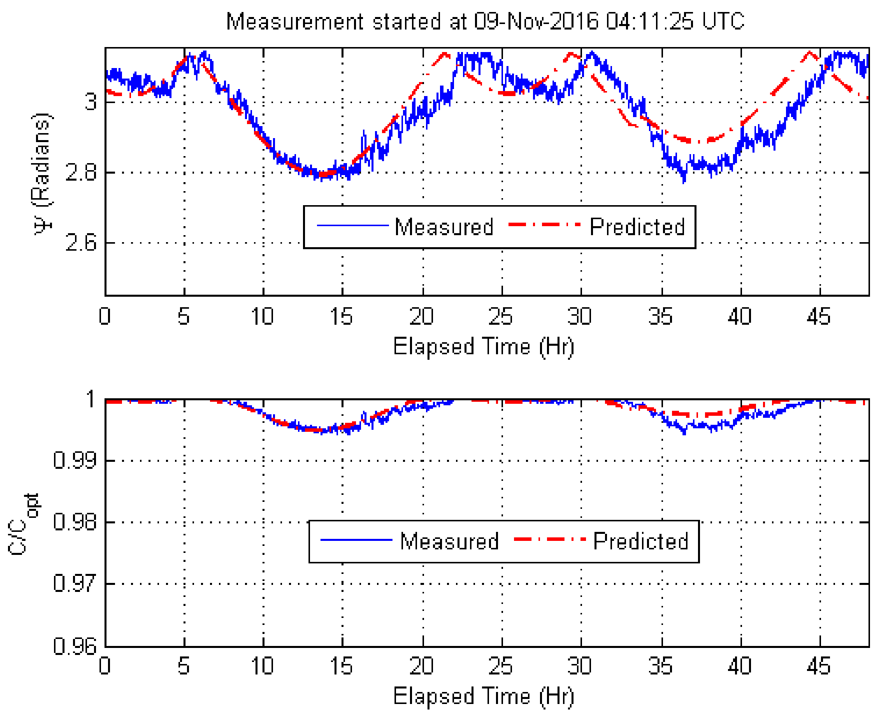


Figure A.2: X-band 3rd maxima position: (top) channel orthogonality and (bottom) normalised capacity

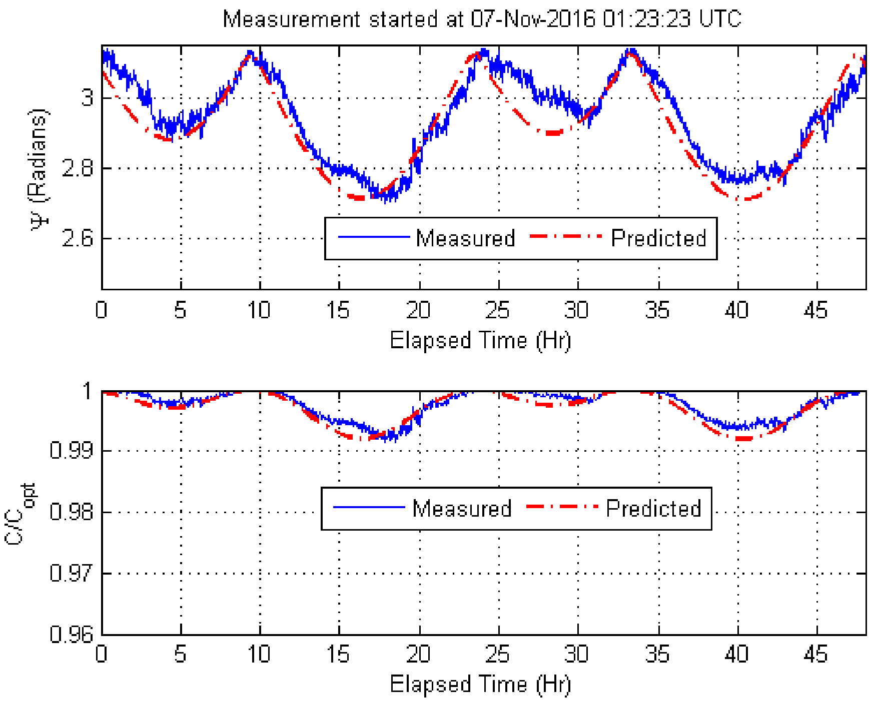


Figure A.3: X-band $4^{\text{th}}$ maxima position: (top) channel orthogonality and (bottom) normalised capacity

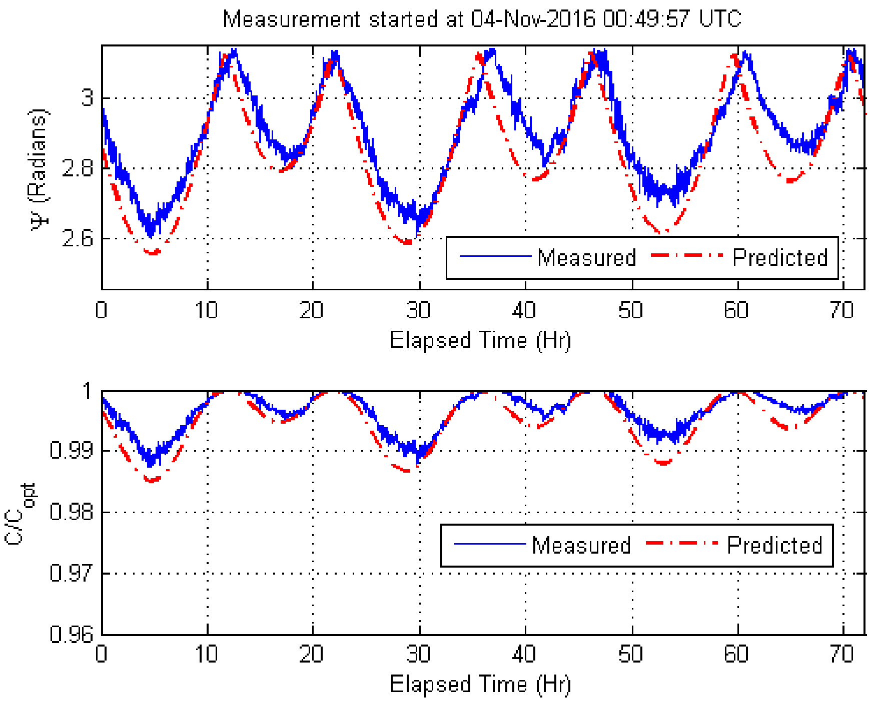


Figure A.4: X-band $5^{\text{th}}$ maxima position: (top) channel orthogonality and (bottom) normalised capacity

# Bibliography


[1] E. Telatar, "Capacity of multiple antenna Gaussian channels," *European Transactions on Telecommunications*, vol. 10, no. 6, pp. 585–595, 1999. [Online]. Available: https://onlinelibrary.wiley.com/doi/abs/10.1002/ett.4460100604

[2] A. J. Paulraj, D. A. Gore, R. U. Nabar, and H. Bolcskei, "An overview of MIMO communications - a key to gigabit wireless," *Proceedings of the IEEE*, vol. 92, no. 2, pp. 198–218, Feb 2004.

[3] S. M. Alamouti, "A simple transmit diversity technique for wireless communications," *IEEE Journal on Selected Areas in Communications*, vol. 16, no. 8, pp. 1451–1458, Oct 1998.

[4] V. Tarokh, N. Seshadri, and A. R. Calderbank, "Space-time codes for high data rate wireless communication: performance criterion and code construction," *IEEE Transactions on Information Theory*, vol. 44, no. 2, pp. 744–765, Mar 1998.

[5] T. L. Marzetta, E. G. Larsson, H. Yang, and H. Q. Ngo, *Fundamentals of massive MIMO*. Cambridge University Press, 2016.

[6] E. Biglieri, R. Calderbank, A. Constantinides, A. Goldsmith, A. Paulraj, and H. V. Poor, *MIMO wireless communications*. Cambridge University Press, 2007.

[7] R. T. Schwarz, A. Knopp, D. Ogermann, C. A. Hofmann, and B. Lankl, "On the prospects of MIMO SatCom systems: The tradeoff between capacity and practical effort," in *2009 6th International Multi-Conference on Systems, Signals and Devices*, March 2009, pp. 1–6.

[8] B. Ramamurthy, W. G. Cowley, and G. Bolding, "MIMO applicability to UHF SATCOM," in *2016 IEEE Global Communications Conference (GLOBECOM)*, Dec 2016, pp. 1–7.

[9] B. Ramamurthy and G. Bolding, "MIMO in UHF SATCOM for land vehicles," in *2016 Future Land Forces Conference (FLFC)*, Sep 2016.

[10] B. Ramamurthy, W. G. Cowley, L. M. Davis, and G. Bolding, "Dual polarization frequency reuse in SATCOM: A method to counter poor cross-polar isolation," in *2014 IEEE Military Communications Conference (MILCOM)*, Oct 2014, pp. 586–591.

[11] B. Ramamurthy, W. G. Cowley, L. M. Davis, and G. Bolding, "On MIMO SATCOM capacity analysis: Utilising polarization and spatial multiplexing," in *2015 IEEE Military Communications Conference (MILCOM)*, Oct 2015, pp. 163–168.

[12] R. Kumar, D. Taggart, R. Monzingo, and G. Goo, "Wideband gapfiller satellite (WGS) system," in *2005 IEEE Aerospace Conference*, March 2005, pp. 1410–1417.

[13] A. I. Perez-Neira, C. Ibars, J. Serra, A. del Coso, J. Gmez-Vilardeb, M. Caus, and K. P. Liolis, "MIMO channel modeling and transmission techniques for multi-satellite and hybrid satellite-terrestrial mobile networks," *Physical Communication*, vol. 4, no. 2, pp. 127 – 139, 2011. [Online]. Available: http://www.sciencedirect.com/science/article/pii/S187449071100019X

[14] T. D. Cola, D. Tarchi, and A. Vanelli-Coralli, "Future trends in broadband satellite communications: Information centric networks and enabling technologies," *International Journal of Satellite Communications and Networking*, vol. 33, no. 5, pp. 473–490, 2015, sat.1101.

[15] J. D. Oetting and T. Jen, "The mobile user objective system," *John Hopkins APL technical Digest*, vol. 30, no. 2, 2011. [Online]. Available: http://techdigest.jhuapl.edu/techdigest/TD/td3002/Oetting.pdf

[16] P. Dingley, A. Frizon, and G. Stanley. (2014) A review of the two primary types of Ka satellite systems. [Online]. Avail-

able: http://www.securecommunications-airbusds.com/wp-content/uploads/2014/04/a-review-of-the-two-primary-types-of-ka-satellite-systems.pdf

[17] G. J. Foschini and M. J. Gans, "On limits of wireless communications in a fading environment when using multiple antennas," *Wireless Personal Communications*, vol. 6, no. 3, pp. 311–335, Mar 1998. [Online]. Available: https://doi.org/10.1023/A:1008889222784

[18] P. D. Arapoglou, K. Liolis, M. Bertinelli, A. Panagopoulos, P. Cottis, and R. De Gaudenzi, "MIMO over satellite: A review," *IEEE Journal on Communications Surveys and Tutorials*, vol. 13, no. 1, pp. 27–51, 2011.

[19] R. T. Schwarz, A. Knopp, D. Ogermann, C. A. Hofmann, and B. Lankl, "Optimum-capacity MIMO satellite link for fixed and mobile services," in *2008 International ITG Workshop on Smart Antennas*, Feb 2008, pp. 209–216.

[20] A. Perez-Neira, C. Ibars, J. Serra, A. del Coso, J. Gomez, and M. Caus, "MIMO applicability to satellite networks," in *2008 10th International Workshop on Signal Processing for Space Communications*, Oct 2008, pp. 1–9.

[21] DVB-NGH, "TM-H NGH study mission report (final)," Tech. Rep., 2008.

[22] P. D. Arapoglou, P. Burzigotti, M. Bertinelli, A. Bolea Alamanac, and R. De Gaudenzi, "To MIMO or not to MIMO in mobile satellite broadcasting systems," *IEEE Trans. on Wireless Communications*, vol. 10, no. 9, pp. 2807–2811, 2011.

[23] P. R. King, "Modelling and measurement of the land mobile satellite MIMO radio propagation channel," Ph.D. dissertation, Apr 2007.

[24] P. R. King, T. W. C. Brown, A. Kyrgiazos, and B. G. Evans, "Empirical-stochastic LMS-MIMO channel model implementation and validation," *IEEE Transactions on Antennas and Propagation*, vol. 60, no. 2, pp. 606–614, Feb 2012.

[25] "MIMOSA: Characterisation of the MIMO channel for mobile satellite systems."

[26] F. Burkhardt, E. Eberlein, S. Jaeckel, G. Sommerkorn, and R. Prieto-Cerdeira, "MIMOSA-a dual approach to detailed land mobile satellite channel modeling,"

*International Journal of Satellite Communications and Networking*, vol. 32, no. 4, pp. 309–328, 2014. [Online]. Available: http://dx.doi.org/10.1002/sat.1045

[27] D. Tse and P. Vishwanath, *Fundamentals of wireless communications.* Cambridge University Press, 2005.

[28] A. Knopp, R. T. Schwarz, and B. Lankl, "On the capacity degradation in broadband MIMO satellite downlinks with atmospheric impairments," in *2010 IEEE International Conference on Communications (ICC)*, May 2010, pp. 1–6.

[29] A. Knopp, R. T. Schwarz, and B. Lankl, "MIMO system implementation with displaced ground antennas for broadband military SATCOM," in *2011 IEEE Military Communications Conference (MILCOM)*, Nov 2011, pp. 2069–2075.

[30] R. T. Schwarz, A. Knopp, and B. Lankl, "Performance of an SC-FDE SATCOM system in block-time-invariant orthogonal MIMO channels," in *2011 IEEE Global Telecommunications Conference (GLOBECOM)*, Dec 2011, pp. 1–6.

[31] C. A. Hofmann, K.-U. Storek, R. T. Schwarz, and A. Knopp, "Spatial MIMO over satellite: A proof of concept," in *2016 IEEE International Conference on Communications (ICC)*, May 2016, pp. 1–6.

[32] M. Hasan and C. Bianchi, "Ka band enabling technologies for high throughput satellite (HTS) communications," *International Journal of Satellite Communications and Networking*, vol. 34, no. 4, pp. 483–501, 2016.

[33] H. Fenech, A. Tomatis, S. Amos, V. Soumpholphakdy, and J. L. Serrano Merino, "Eutelsat HTS systems," *International Journal of Satellite Communications and Networking*, vol. 34, no. 4, pp. 503–521, 2016, sAT-15-0018.R3. [Online]. Available: http://dx.doi.org/10.1002/sat.1171

[34] M. Caus, A. I. Perez-Neira, M. Angelone, and A. Ginesi, "An innovative interference mitigation approach for high throughput satellite systems," in *2015 IEEE 16th International Workshop on Signal Processing Advances in Wireless Communications (SPAWC)*, June 2015, pp. 515–519.

[35] V. Boussemart, L. Marini, and M. Berioli, "Multi-beam satellite MIMO systems: BER analysis of interference cancellation and scheduling," in *2012 6th Advanced Satellite Multimedia Systems Conference (ASMS) and 12th Signal Processing for Space Communications Workshop (SPSC)*, Sept 2012, pp. 197–204.

[36] G. Colavolpe, A. Modenini, A. Piemontese, and A. Ugolini, "Multiuser detection in multibeam satellite systems: Theoretical analysis and practical schemes," *IEEE Transactions on Communications*, vol. 65, no. 2, pp. 945–955, Feb 2017.

[37] V. Joroughi, M. A. Vazquez, and A. I. Perez-Neira, "Generalized multicast multibeam precoding for satellite communications," *IEEE Transactions on Wireless Communications*, vol. 16, no. 2, pp. 952–966, Feb 2017.

[38] M. M. Rahman, "Distributed beamforming and nullforming: Frequency synchronization techniques, phase control algorithms and proof-of-concept," Ph.D. dissertation, Aug 2013.

[39] S. Jayasimha and P. Jyothendar, "Reducing VSAT aperture via satellite MIMO," in *2008 IEEE Military Communications Conference (MILCOM)*, 2008, pp. 1–6.

[40] F. Yamashita, K. Kobayashi, M. Ueba, and M. Umehira, "Broadband multiple satellite MIMO system," in *IEEE* $62^{nd}$ *Vehicular Technology Conference, VTC-2005-Fall.*, vol. 4, pp. 2632–2636.

[41] R. B. Dybdal, "UHF satcom antenna architectures," in *MILCOM 2000 Proc. 21st Century Military Communications Architectures and Technologies for Information Superiority (Cat. No.00CH37155)*, vol. 2, 2000, pp. 801–804 vol.2.

[42] D. A. Fritz, B. T. Doshi, A. C. Oak, S. D. Jones, J. L. Burbank, H. L. Miller, J. D. Oetting, R. M. Collins, L. A. Gonzalez, and R. A. Nichols, "Military satellite communications: Space-based communications for the global information grid," in *John Hopkins APL technical Digest*, vol. 27, no. 1, 2006. [Online]. Available: http://techdigest.jhuapl.edu/TD/td2701/Fritz.pdf

[43] E. Gunduzhan and K. Dewayne Brown, "Narrowband satellite communications: Challenges and emerging solutions," in *John Hopkins APL technical Digest*,

vol. 33, no. 1, 2015. [Online]. Available: http://www.jhuapl.edu/techdigest/TD/td3301/33_01-Gunduzhan.pdf

[44] J. Sadowski, "Measurement of coherence bandwidth in UHF radio channels for narrowband networks," *International Journal of Antennas and Propagation, Hindawi Publishing*, Apr 2015.

[45] X. Tang and Y. Hua, "Optimal design of non-regenerative mimo wireless relays," *in IEEE Transactions on Wireless Communications*, vol. 6, no. 4, pp. 1398–1407, 2007.

[46] G. Maral and M. Bousquet, *Satellite communications systems.* John Wiley, 4th ed., 2002.

[47] ETSI-EN-302-307-1, "Digital Video Broadcasting (DVB): Second generation framing structure, channel coding and modulation systems for broadcasting, interactive services, news gathering and other broadband satellite applications."

[48] P. D. Arapoglou, M. Zamkotsian, and P. Cottis, "Dual polarization MIMO in LMS broadcasting systems: Possible benefits and challenges," *International Journal of Satellite Communications and Networking*, vol. 29, no. 4, pp. 349–366, 2011. [Online]. Available: http://dx.doi.org/10.1002/sat.986

[49] M. Sellathurai, P. Guinand, and J. Lodge, "Space-time coding in mobile satellite communications using dual-polarized channels," *IEEE Transactions on Vehicular Technology*, vol. 55, no. 1, pp. 188–199, 2006.

[50] R. U. Nabar, H. Bolcskei, V. Erceg, D. Gesbert, and A. J. Paulraj, "Performance of multiantenna signaling techniques in the presence of polarization diversity," *IEEE Transactions on Signal Processing*, vol. 50, no. 10, pp. 2553–2562, 2002.

[51] J. S. Seybold, *Introduction to RF propagation.* Wiley, 2005.

[52] L. Gonzalez, C. McLain, and W. Hall, "A plausible CONOPS for frequency reuse at Ka-band on WGS system," in *2011 IEEE Military Communications Conference (MILCOM)*, Nov 2011, pp. 1676–1683.

[53] P. Wade, "Septum polarizers and feeds," in *Proc. of Microwave update, W1GHZ*, 2003. [Online]. Available: http://www.w1ghz.org/antbook/conf/SEPTUM.pdf

[54] P. S. Kildal, *Foundations of Antennas: A Unified Approach.* Studentlitteratur, Lund, 2000.

[55] P. S. Kildal, *Foundations of Antenna Engineering: A Unified Approach for Line-of-Sight and Multipath.* Chalmers University of Technology, 2015.

[56] M. Coldrey, "Modeling and capacity of polarized MIMO channels," in *2008 IEEE Vehicular Technology Conference (VTC Spring)*, May 2008, pp. 440–444.

[57] I. Gupta and A. Ksienski, "Effect of mutual coupling on the performance of adaptive arrays," *Antennas and Propagation, IEEE Transactions on*, vol. 31, no. 5, pp. 785–791, Sep 1983.

[58] K. Zarifi, S. Affes, and A. Ghrayeb, "Collaborative null-steering beamforming for uniformly distributed wireless sensor networks," *IEEE Transactions on Signal Processing*, vol. 58, no. 3, pp. 1889–1903, March 2010.

[59] "Satellite tracking TLE files." [Online]. Available: http://www.satflare.com/home.asp

[60] P. Almers, F. Tufvesson, and A. F. Molisch, "Keyhole effect in MIMO wireless channels: Measurements and theory," *IEEE Transactions on Wireless Communications*, vol. 5, no. 12, pp. 3596–3604, Dec 2006.

[61] V. Dantona, T. Delamotte, G. Bauch, and B. Lankl, "Impact of nonlinear power amplifiers on the performance of precoded MIMO satellite systems," in *2012 IEEE First AESS European Conference on Satellite Telecommunications (ESTEL)*, 2012, pp. 1–7.

[62] A. B. Carlson, *Communications systems: An introduction to signals and noise in electrical communications.*

[63] A. G. Piersol, "Time delay estimation using phase data," *IEEE Trans. on Acoustics, Speech and Signal Processing*, vol. 29, no. 3, pp. 471–477, 1981.

[64] R. Rafael and H. Mathias, "Application note: How to utilize the I/Q software interface of the RS RTO oscilloscope with Matlab," 2014. [Online]. Available: https://cdn.rohde-schwarz.com

[65] "Satellite and flare tracking." [Online]. Available: https://www.prismnet.com/~mmccants/tles/index.html

[66] R. T. Schwarz, F. Volk, A. Knopp, C. A. Hofmann, and K. U. Storek, "The multiple-satellite MIMO channel of narrow band vehicular communications at UHF," in *2017 IEEE Military Communications Conference (MILCOM)*, Oct 2017, pp. 447–452.

[67] C. A. Hofmann, R. T. Schwarz, and A. Knopp, "Multisatellite UHF MIMO channel measurements," *IEEE Antennas and Wireless Propagation Letters*, vol. 16, pp. 2481–2484, 2017.

[68] G. Huckell and F. Tirpak, "What the mobile user objective system will bring to UHF SATCOM," in *2007 IEEE Military Communications Conference (MILCOM)*, Oct 2007, pp. 1–4.